Characterization and Modeling of Solar Flare Effects in the Ionosphere Observed by HF Instruments

Shibaji Chakraborty

Dissertation submitted to the Faculty of the
Virginia Polytechnic Institute and State University
in partial fulfillment of the requirements for the degree of

Doctor of Philosophy
in
Electrical Engineering

J. Michael Ruohoniemi, Co-chair
Joseph B. H. Baker, Co-chair
Gregory D. Earle
Scott M. Bailey
Bhuvana Srinivasan
Scott England
Lamine M. Mili

May 07, 2021
Blacksburg, Virginia

Keywords: Space Weather, Solar Flare, Shortwave Fadeout, HF Absorption, Collision Frequency, Ionospheric Sluggishness, Doppler Flash

Characterization and Modeling of Solar Flare Effects in the Ionosphere Observed by HF Instruments

Shibaji Chakraborty

(ABSTRACT)

The ionosphere is the conducting part of the upper atmosphere that plays a significant role in trans-ionospheric high frequency (HF, 3-30 MHz) radiowave propagation. Solar activities, such as solar flares, radiation storms, coronal mass ejections (CMEs), alter the state of the ionosphere, a phenomenon known as Sudden Ionospheric Disturbance (SID), that can severely disrupt HF radio communication links by enhancing radiowave absorption and altering signal frequency and phase. The Super Dual Auroral Radar Network (SuperDARN) is an international network of low-power HF coherent scatter radars distributed across the globe to probe the ionosphere and its relation to solar activities. In this study, we used SuperDARN HF radar measurements with coordinated spacecraft and riometer observations to investigate statistical characteristics and the driving mechanisms of various manifestations of solar flare-driven SIDs in HF observations. We begin in Chapter 2 with a statistical characterization of various effects of solar flares on SuperDARN observations. Simultaneous observations from GOES spacecraft and SuperDARN radars confirmed flare-driven HF absorption depends on solar zenith angle, operating frequency, and intensity of the solar flare. The study found flare-driven SID also affects the SuperDARN backscatter signal frequency, which produces a sudden rise in Doppler velocity observation, referred to as the "Doppler flash", which occurs before the HF absorption effect. In Chapter 3, we further investigate the HF absorption effect during successive solar flares and those co-occurring with other geomagnetic disturbances during the 2017 solar storm. We found successive solar flares can

extend the ionospheric relaxation time and the variation of HF absorption with latitude is different depending on the type of disturbance. In Chapter 4, we looked into an inertial property of the ionosphere, sluggishness, its variations with solar flare intensity, and made some inferences about D-region ion-chemistry using a simulation study. Specifically, we found solar flares alter the D-region chemistry by enhancing the electron detachment rate due to a sudden rise in molecular vibrational and rotational energy under the influence of enhanced solar radiation. In Chapter 5, we describe a model framework that reproduces HF absorption observed by riometers. This chapter compares different model formulations for estimating HF absorption and discusses different driving influences of HF absorption. In Chapter 6, we have investigated different driving mechanisms of the Doppler flash observed by SuperDARN radars. We note two particular findings: (i) the Doppler flash is predominantly driven by a change in the F-region refractive index and (ii) a combination of solar flare-driven enhancement in photoionization, and changes in the zonal electric field and(or) ionospheric conductivity reduces upward ion-drift, which produces a lowering effect in the F-region HF radiowave reflection height. Collectively, these research findings provide a statistical characterization of various solar flare effects on the ionosphere seen in the HF observations, and insights into their driving mechanisms and impacts on ionospheric dynamics.

Characterization and Modeling of Solar Flare Effects in the Ionosphere Observed by HF Instruments

Shibaji Chakraborty

(GENERAL AUDIENCE ABSTRACT)

The Earth's ionosphere, extending from about 60 km to 1000 km in altitude, is an electrically charged region of the upper atmosphere that exists primarily due to ionization by solar X-ray and extreme ultraviolet radiation. The ionosphere is an effective barrier to energetic electromagnetic (EM) radiation and charged particles originating from the Sun or any other extraterrestrial sources and protect us against harmful space radiation. High frequency (HF, 3-30 MHz) radio communication, broadly used for real-time medium and long-range communication, is strongly dependent on the state of the ionosphere, which is susceptible to solar activities, such as solar flares, solar energetic particles (SEPs), and coronal mass ejections (CMEs). Specifically, we are interested in the impacts of solar flares. In this study, we use Super Dual Auroral Radar Network (SuperDARN) HF radars, ground-based riometers, and coordinated spacecraft observations to investigate the driving mechanisms of various space weather impacts on the ionosphere and radiowave propagation following solar flares. We begin in Chapter 2 with a characterization of various kinds of ionospheric disturbances manifested in SuperDARN backscattered signal following solar flares. Specifically, we characterized HF absorption effects and frequency anomalies experienced by traveling radiowaves, also known as Shortwave Fadeout (SWF) and Sudden Frequency Deviations (SFDs), respectively. In SuperDARN HF radar observations, SFDs are recorded as a sudden enhancement in Doppler velocity, which is referred to as the "Doppler flash". In Chapter 3, we investigate a special event study that elucidates the nonlinear physics behind HF absorption caused

by multiple simultaneous solar flares and flares co-occurring with SEPs and CMEs. In Chapter 4, we explore an inertial property of the ionosphere, known as sluggishness, and its dependence on solar flares can provide important information about the chemical proprieties of the ionosphere. We found that the enhanced solar radiation during a solar flare increases the molecular vibrational and rotational energy that in turn enhances the electron detachment rate and reduces ionospheric sluggishness. In Chapter 5, we describe a framework to estimate HF absorption observed by riometers following solar flares. We analyze the influence of different physical parameters, such as collision frequency and electron temperature, on HF absorption. In Chapter 6, we delved into the physical processes that drive the Doppler flash in SuperDARN observations following solar flares. We find, (i) the Doppler flash is predominately driven by change in the F-region refractive index and (ii) a combination of solar flare-driven enhancement in photoionization, and change in zonal electric field and(or) ionospheric conductivity reduces upward ion-drift, which produces a lowering effect in the F-region HF radiowave reflection height. Taken together, these research findings provide new insights into solar flare impacts on the ionosphere and could be used to improve forecasting of ionospheric space weather disturbances following solar flares.

Dedication

To my parents Uma Prasanna Chakraborty & Mandira Chakraborty and my loving wife Sarasi Banerjee.

Acknowledgments

I want to start by expressing my deepest gratitude to my advisors, Dr. J. Michael Ruohoniemi and Dr. Joseph B. H. Baker, for their continuous support and guidance throughout my graduate career. I forever feel fortunate to have looked into the Space@VT SuperDARN lab website and expressed my propensity towards space physics to Dr. Ruohoniemi over an email, which led me to admission to the Virginia Tech SuperDARN space science group. Coming in with no space science background, I have learned a lot on the topics along with a wide range of new skills such as data analytics and machine learning, all thanks to their support and encouragement. I would especially like to thank them for giving me the freedom to pursue my passion for Data Science and complete a graduate certification in Data Analytics from the Discovery Analytics Center and a dual Master of Arts degree in Data Analysis & Applied Statistics from the Department of Statistics. I feel so blessed to have been a student of two wonderful professors who see the value in such pursuits. I thank them for all their efforts in making the VT SuparDARN group such a wonderful place for me and others.

I am very grateful to Dr. Gregory D. Earle, Dr. Scott M. Bailey, Dr. Bhuvana Srinivasan, Dr. Scott England, and Dr. Lamine M. Mili for serving as my committee members and for their time and efforts in reviewing this dissertation. Special thanks to Dr. Scott M. Bailey for collaborating on one of my studies and providing his insight, which led to one first-authored paper published in JGR Space Physics.

I want to thank and acknowledge my collaborators. First, I thank Dr. Nozumu Nishi-

tani for his prior work that provided the initial motivation for my research on solar flare impacts using SuperDARN HF radars. I thank Dr. Robyn Fiori for allowing me to collaborate with her on riometer based HF absorption studies, sharing the data, and her invaluable research insight on HF absorption. I thank Dr. Liying Qian at the High Altitude Observatory (HAO) laboratory at NCAR, Boulder, Colorado, for being my host and mentor during NCAR's Graduate Visitor Program (ASP-GVP). I also thank Dr. Steven Karl Morley at the Los Alamos National Laboratory for mentoring me during the 2018 LANL Space Weather Summer School. I would also like to thank Dr. Bharat Kunduri, Dr. Raymond A. Greenwald and Dr. Kjellmar Oksavik for providing invaluable research insights.

I also extend my gratitude to all of my past and present lab-mates for their friendly support and invaluable suggestions. Special thanks to Mr. Kevin Sterne for his tireless effort in keeping the radars and data servers functioning, Dr. Maimaitirebike Maimaiti (Muhammad), and Dr. Xueling Shi for teaching me technical skills and for countless valuable discussions on many different things. I would also like to thank the Space@VT center administrators, ECE staff members, and computer systems administrators for their support and assistance. Special thanks to Debbie Collins for helping with administrative processes, always treating me with kindness, and saying encouraging words when things became tough on me.

Finally, I am deeply grateful to my childhood teachers, Mr. Arun Kumar Bhattacharya, Mr. Manabendra Sadhu, and Mr. Aparesh Roy, who made me fall in love with general sciences. To my parents, uncles Mr. Asish Achariya and Girija Prasanna Chakraborty, my wife Sarasi, my mother-in-law Supriya Banerjee, and my extended family, I do not have words to express my thanks and gratitude towards you. To my friends Uddipan, Mallik, Bhanja, Subhasish, Arindam, Jayanta, Papai, and others who make my life as stress-free as possible. I have arrived at this stage because of your unconditional love and support throughout my

life. I am incredibly blessed and honored to be born to such a wonderful family and friends.

This research was supported by the National Science Foundation under grants AGS-1935110, AGS-1341918, the NASA under 80NSSC20K1380, and partially by NCAR's Advanced Study Program's Graduate Student (GVP) Fellowship.

Contents

List of Figures

List of Tables

Chapter 1

Introduction

In this chapter, we present introductory material for this research including descriptions of the solar-terrestrial environment, various forms of solar activity and their impact on the ionosphere, the instruments used, research objectives, and the organization of the dissertation.

1.1 The Sun

Among the four fundamental states of matter in physics, namely solid, liquid, gas, and plasma, plasma is the most ubiquitous in our universe. Plasma is a quasi-neutral gas consisting of approximately equal numbers of positively charged ions and negatively charged electrons. The Sun at the heart of our solar system contains 99.86% of the total mass of the solar system and is a gigantic ball of plasma. The Sun emits EM radiation at all wavelengths, but approximately 44% falls within the visible portion of the EM spectrum and has its source in the photosphere region of the lower solar atmosphere. The Sun also releases a steady outward stream of plasma known as the solar wind. The source of the solar wind is the Sun's corona, the outermost layer of the Sun's atmosphere, which is so hot that gravity cannot overcome thermal expansion. The solar wind carries a remnant portion of the solar magnetic field called the interplanetary magnetic field (IMF). The IMF is "frozen-in" to the highly conductive solar wind, thus both travel at the same speed that ranges from 300 to

800 km/s. Solar EM radiation travels at the speed of light and takes ∼8 minutes to reach Earth while the solar wind generally takes 2 to 3 days to reach Earth.

1.2 Geospace: The Magnetosphere

To first order, the Earth's magnetic field (i.e. the Geomagnetic Field) can be described as a bar magnet. Figure 1.1 presents an illustration of a first order model of a dipole Earth magnetic field, which is directed horizontal near the equator and nearly vertical at both poles. The source of the geomagnetic field is circulating electric currents due to the motion of molten iron in Earth's outer core [101]. The geomagnetic field plays an important role in the coupling of the geospace regions and response to the solar wind.

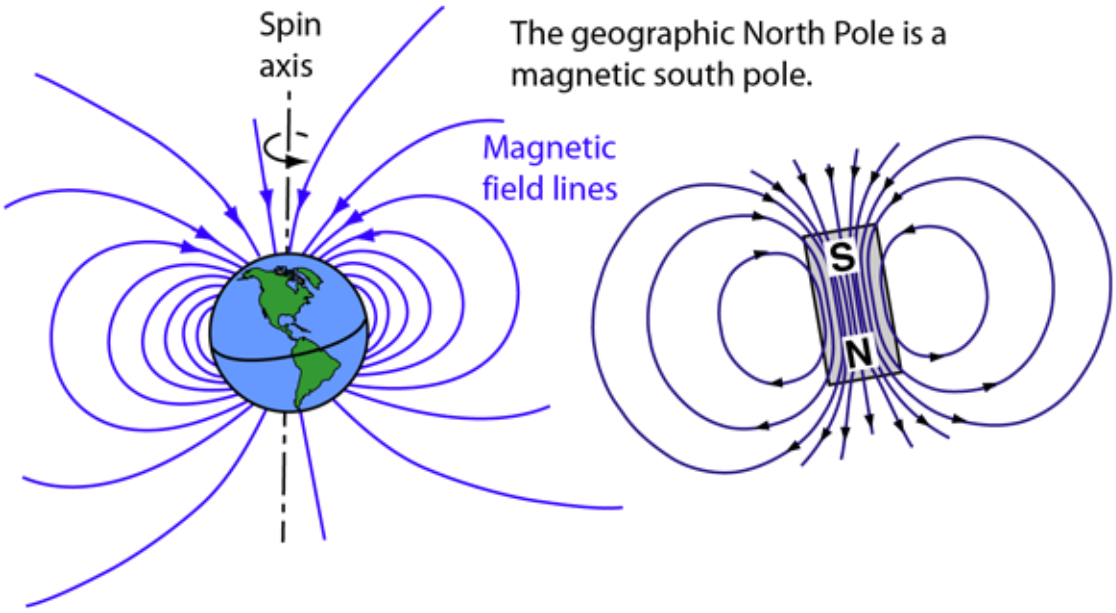

Figure 1.1: Schematic of the Earth's magnetic field assuming Earth is a bar magnet (left) and an equivalent bar magnet (right) (Image source)

The Earth's magnetosphere is the region of space surrounding Earth in which the physics of charged particle motion is dominated by the geomagnetic field. The shape and size of the

magnetosphere has a strong dependence on solar wind and IMF conditions.

1.3 The Atmosphere

The Earth's atmosphere is the collection of gases that are gravitationally bound to the planet. The atmosphere is mainly composed of nitrogen (∼78%), oxygen (∼21%), argon (∼0.93%), and carbon dioxide (∼0.038%). Water vapour and other trace gas constituents are present in small amounts. Similar to the magnetosphere, Earth's atmosphere partially protects us from energetic extraterrestrial radiations. The atmosphere can be subdivided into layers based on the vertical temperature profile. Figure 1.2 (left) shows the five layers of the atmosphere from bottom to top: troposphere, stratosphere, mesosphere, thermosphere, and exosphere. The transition regions between layers are referred to as "pauses". The innermost layer of the atmosphere is the troposphere that exists between 0-10 km altitudes. In the troposphere, there is a negative temperature gradient with height (solid curve in Figure 1.2 (left)). Around 80% of the total mass of the atmosphere is retained in this layer and its dynamics is what we colloquially refer to as "weather". The topside boundary of the troposphere is known as the "tropopause"; here, the temperature stops increasing with altitude, producing a temperature inversion.

The next atmospheric layer is the stratosphere, ranging from ∼10-50 km in altitude, with the tropopause as its lower boundary. The very important ozone layer that protects us from harsh solar ultraviolet radiation is confined in this layer. The temperature inversion that started in the tropopause continues with altitude until the upper "stratopause" boundary of the stratosphere is encountered at ∼50-55 km altitude. This positive temperature gradient with altitude is mainly caused by the absorption of solar ultraviolet (UV) radiation in the ozone layer. The mesosphere is located between ∼50-85 km altitude and is the coldest of

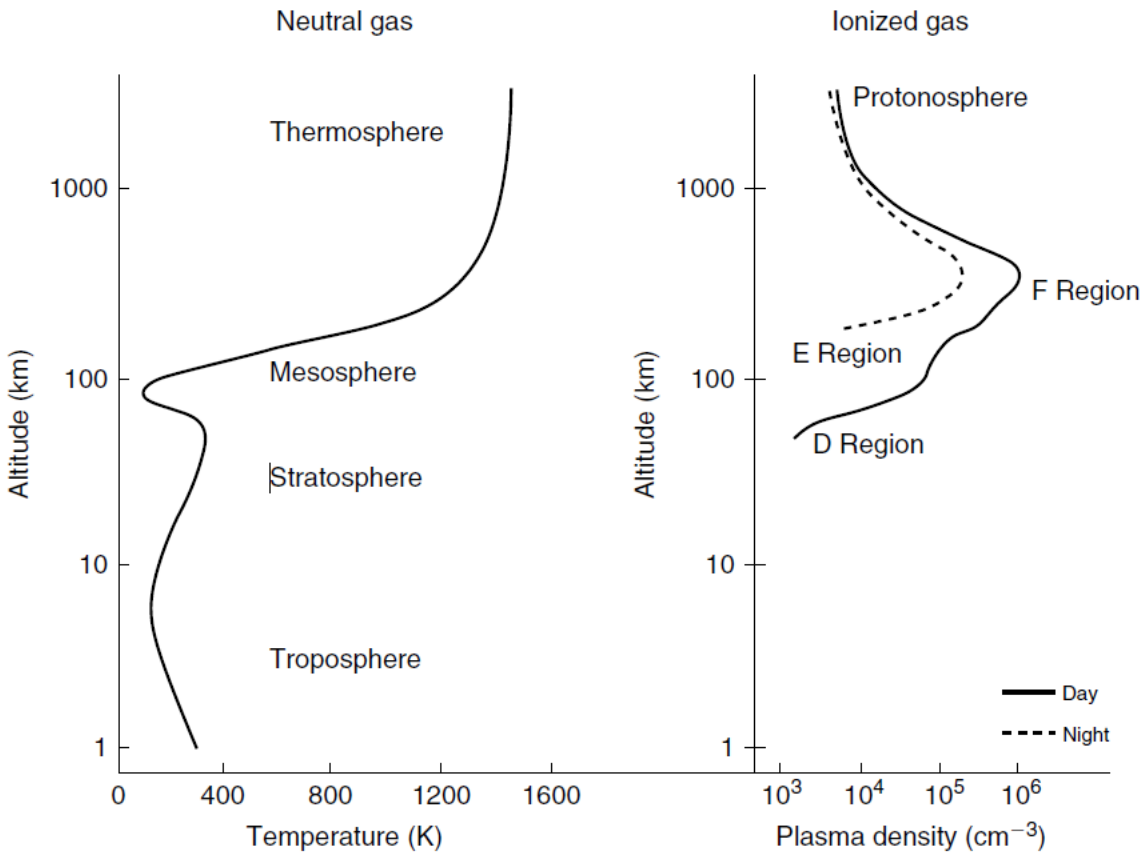

Figure 1.2: Typical profiles of neutral atmospheric temperature (left) and ionospheric plasma density (right) with the various layers designated (from Kelley [72]).

all the atmospheric layers. The negative temperature gradient with altitude is due to the decreased solar radiation heating and increased cooling by CO_2 radiative emission. The topside boundary of the mesosphere where the temperature reaches its minimum is called the "mesopause". The majority of meteors dissipate in the mesosphere. The layer above the mesosphere is the thermosphere, existing between ∼85-600 km altitudes. A second temperature inversion occurs at the "mesopause". Due to absorption of solar X-ray and extreme ultraviolet (EUV) radiation, we see a dramatic increase in temperature. The International Space Station and most low Earth orbit satellites are located in this layer. The exosphere is the outermost layer of Earth's atmosphere, existing from ∼600 to 10,000 km altitude. It

separates the atmosphere from outer space.

1.4 The Ionosphere

The Earth's atmosphere coexists with a region of ionized gas (i.e. plasma) commonly known as the "Ionosphere". The ionosphere extends from about 60 km to 1000 km above the Earth's surface. The ionosphere is generated on the dayside primarily through photoionization by solar x-rays and extreme ultraviolet radiation. There is also impact ionization produced by precipitation of magnetospheric particles around the high latitude auroral oval region. The ionosphere is structured into three semi-distinct regions or "layers" organized by plasma density: the D, E, and F-regions.

D-region: This layer is located between ∼60-90 km altitude. Lyman-α and X-rays are the major sources of ionization. Lyman-α is responsible for ionizing NO while X-rays are responsible for ionizing molecular oxygen (O_2) and molecular nitrogen (N_2). Due to high recombination rates, the half-life of the D-region is measured in minutes and it thus requires a continuous source of radiation to be sustained. The D-region thus disappears completely after sunset. Due to the high neutral density, the plasma-neutral collision frequency is high in the D-region and this causes significant attenuation of high frequency (HF: 3-30 MHz) radiowaves. This explains why distant AM broadcast band stations cannot be heard during the daytime. Due to its relatively low plasma density traveling radiowaves do not experience significant refraction and thus the D-region is also referred to as the non-deviative layer of the ionosphere.

E-region: This region exists between 90-150 km during daytime. The primary ionization source is solar soft X-ray and far ultraviolet (FUV) radiation, which primarily ionize molecular oxygen. Secondary ionization is created by electrons and ions precipitating from the

magnetosphere along magnetic field lines into the nightside high latitude auroral zones. The neutral density is much lower in the E-region compared to the D-region so the recombination rate is slower allowing the layer to be sustained at nighttime, though at much lower densities. There is also attenuation of radiowaves in the E-region, but at a lower level than in the D-region.

F-region: This region extends above 150 km (>150 km). The F-region is the outermost layer of the ionosphere and it is here that the overall electron density maximizes. During daytime we can subdivide the F-region into two sub-layers, the **F1-layer** (∼150-200 km) and the **F2-layer** (>200 km), which merge to form one single layer during night. The F2-layer has relatively higher electron density because vertical diffusion produces accumulation of plasma at upper F-region altitudes. Due to the very low neutral density we consider this region to be collisionless and it therefore does not produce significant attenuation of traveling HF radiowaves. Due to high plasma density traveling radiowaves experience significant refraction and thus the F-region is referred to as a deviative layer of the ionosphere.

1.5 Solar Activity and Space Weather

In this section, we describe the three main forms of solar activity and their space weather impacts, namely solar flares (SFs), coronal mass ejections (CMEs), and solar energetic proton events (SEPs). All of the solar activity features described here propagate outward from the Sun through interplanetary space and can produce severe impacts in the magnetosphere and ionosphere.

At visible wavelengths the Sun's radiant output is relatively constant but at other wavelengths (e.g. X-rays, EUV, UV, FUV, IR, radiowave) the Sun is a highly variable star. This is demonstrated in Figure 1.3, which shows solar spectral irradiance and relative variability

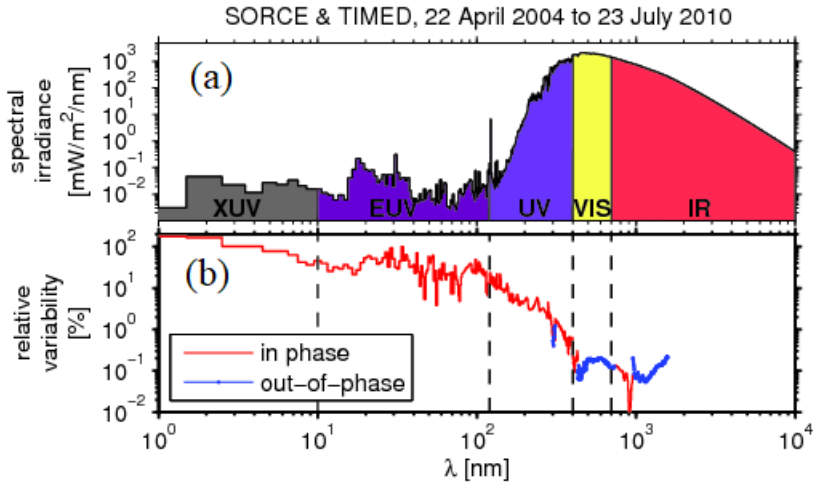

Figure 1.3: Solar spectral irradiance as inferred from SOURCE and TIMED satellite observations between 22nd April 2004 and 23rd July 2010: (a) average spectral irradiance and (b) relative variability of solar irradiance (peak/average) (Image source)

versus the wavelength of solar EM radiation. At short wavelengths (XUV, EUV) the irradiance is relatively low but the variability is high whereas at visible and IR wavelengths the irradiance is high and the variability is low. The variability of short wavelength solar EM radiation is governed by the ∼11 year magnetic activity cycle (or "sunspot cycle"). Sunspots are dark, cooler, regions in the Sun's photosphere characterized by strong magnetic fields that inhibit plasma convection. The sunspot cycle progresses from solar minimum, when there are fewer sunspots and less activity, to solar maximum when there are more sunspots and more activity. Figure 1.4(a) shows how the EUV irradiance (at X-ray wavelengths) of the solar chromosphere evolves over the 11 year solar cycle while Figure 1.4(b) shows a sunspot on the photosphere disk and a closeup view. Magnetic activity in the vicinity of sunspots creates short-lived disturbances, i.e., solar flares, solar energetic proton events, and coronal mass ejections.

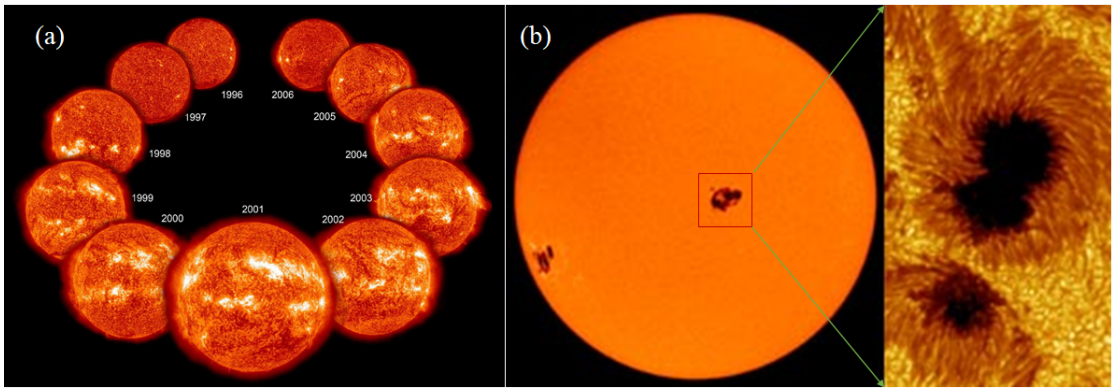

Figure 1.4: (a) Evolution of EUV emission from the solar chromosphere through the 11 year solar cycle (Image source) and (b) image of the solar photosphere and a closeup view of a sunspot (Image Source)

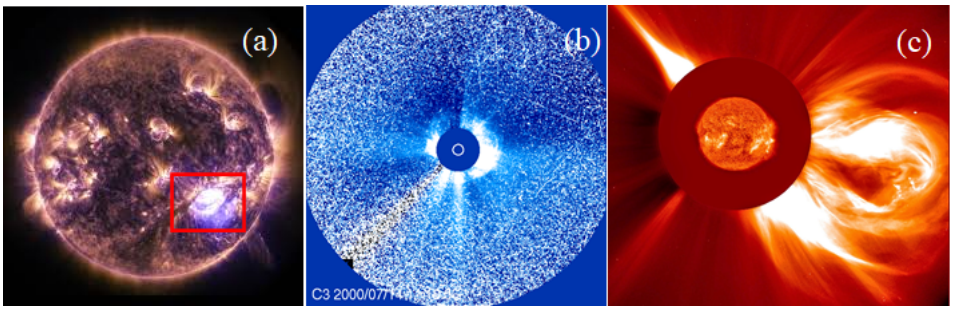

Figure 1.5: Solar activity captured by various spacecraft imagers: (a) X-ray image from the Atmospheric Imaging Assembly (AIA) on the Solar Dynamics Observatory (SDO) showing a solar flare on December 19, 2014 (Image source), (b) Solar and Heliospheric Observatory (SOHO) coronagraph image showing contamination by solar energetic protons (Image source), and (c) solar coronagraph image captured by SOHO on December 2, 2003 (Image source).

1.5.1 Solar Flares and Sudden Ionospheric Disturbances (SIDs)

A solar flare is a sudden localized intensification of EM radiation across a wide range of the EM spectrum, caused by rearrangement of magnetic field in the vicinity of sunspots. This intense EM radiation can degrade space borne electrical equipment, cameras, and expose humans to dangerous levels of X-ray radiation. Solar flares are often accompanied by solar energetic proton events (SEPs) and coronal mass ejections (CMEs). Flares are classified into three categories based on their intensity in the soft X-ray (0.1-0.8 nm, SXR) waveband of the

EM spectrum: C, M or X, with X being the strongest. There is a tenfold increase in intensity in the SRX waveband from one class to the next, such that an X-class flare is 100 times more powerful than a C-class flare. There is also gradation of solar flare intensity within each class from 1 to 9, e.g. a solar flare classified as X2.2 has a power rating 2.2×10^{-4} Wm^{-2}. Figure 1.5(a) shows an image of a solar flare that occurred on December 19, 2014.

Electromagnetic emissions from solar flares travel at the speed of light and hence reach the Earth in ∼8 minutes. Sudden intensification of solar EM radiation during solar flares enhances photoionization and increases ionospheric plasma density in all three ionospheric regions leading to sudden ionospheric disturbances (SIDs). Figure 1.6 presents a schematic illustration depicting the solar flare-induced enhancement of daytime ionospheric plasma density and resulting sudden ionospheric disturbances. As shown in the figure, the impact of flare-driven SIDs is more severe at the subsolar point and decreases with increasing solar zenith angle. The SID results in a sudden increase in ionospheric radiowave absorption that is most severe in the high frequency (HF) ranges, and, as a result, often interrupts or interferes with telecommunications systems. This disruption of HF signal is broadly categorized as shortwave fadeout (SWF) and sudden frequency deviation (SFD).

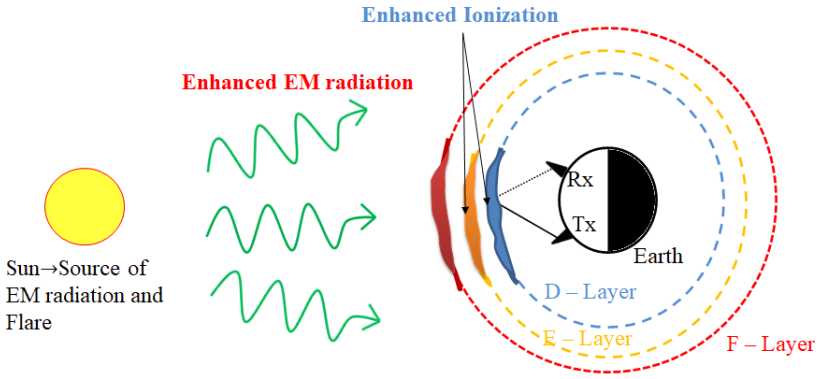

Figure 1.6: Schematic showing solar flare induced daytime enhancement of ionospheric electron density and sudden ionospheric disturbances.

Shortwave Fadeout (SWF)

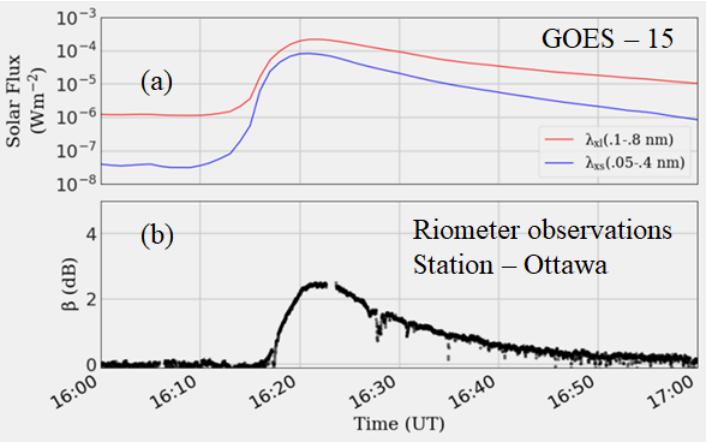

Figure 1.7: Example solar flare event on 11th March, 2015: (a) solar flux observed by GOES 15 geostationary satellite's X-ray sensors [refer to Section 1.7] and (b) ionospheric HF absorption observed by the Ottawa riometer [refer to Section 1.7] station.

Shortwave Fadeout (SWF) is a sudden increase in radiowave absorption in the high frequency (HF) ranges (3-30 MHz) [39]. Figure 1.7 presents an example solar flare event and enhanced ionospheric HF absorption recorded by the geostationary GOES 15 satellite's on-board X-ray sensors and ground based HF receiver, respectively. Figure 1.8 presents a schematic diagram depicting the solar flare induced absorption effect on a traveling radiowave passing through the stratified ionosphere with the D, E, and F-regions identified. The radiowave in green is transmitted from the ground and passes successively through the neutral atmosphere, D, E, and F-regions, respectively. The color of the radiowave changes as it passes through each region. As mentioned earlier, the D-region is highly collisional in nature and this causes the radiowave to lose EM energy in the form of heat via plasma-neutral collision. One way transmit-receive requires the signal to pass through the D-region twice. Sudden enhancement in solar irradiance following a solar flare increases the plasma density of the ionosphere, including in the D-region, which produces an intensification of radiowave absorption, referred to as Shortwave Fadeout or SWF.

Sudden Frequency Deviation (SFD)

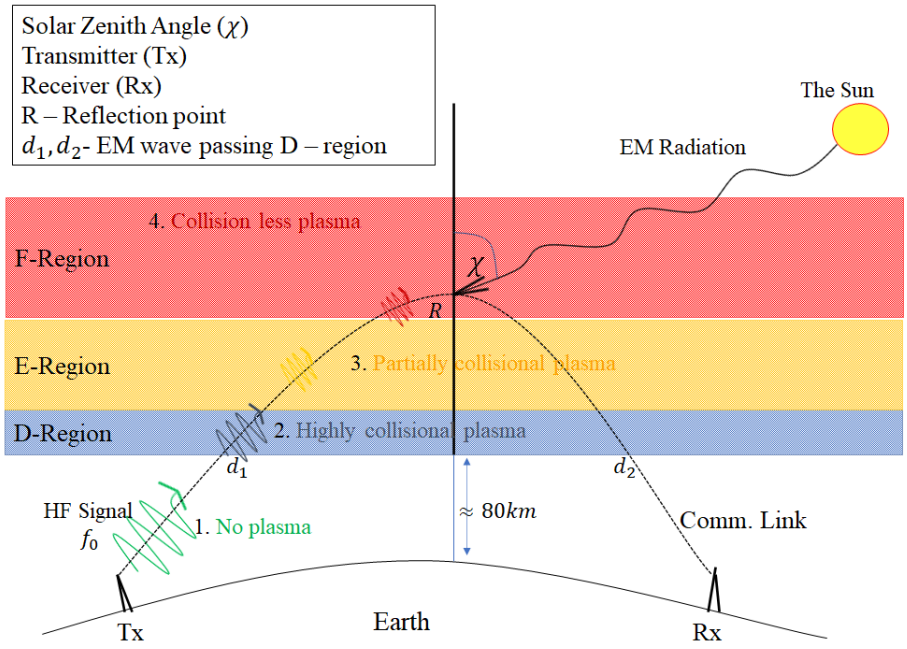

Figure 1.8: Illustration of sudden ionospheric disturbance induced SWF and SFD.

Sudden Frequency Deviation (SFD) following a solar flare is a sudden change in the frequency of the traveling radiowave [39]. Figure 1.9 presents an example of sudden frequency deviation observed by a ground-based vertical HF sounder following a solar flare on 22 October 2014. The sudden jump in the signal between 14 and 14.25 UT in the figure represents SFD of the transmitted signal. The schematic presented in Figure 1.8 depicts a change in the frequency of the traveling radiowave, in addition to a change in its amplitude or intensity. Previous studies have suggested that the frequency deviation is caused by a sudden change in the phase path length of the travelling radiowaves [e.g. 75, 156]. Kikuchi et al. [75] suggested two possible sources that might contribute to the change in phase path length: first, changes in the refractive index due to enhancement of plasma density in the non-deviative part of the ionosphere, i.e., D and lower E-regions; and second, changes in the F-region ray reflection height. Kikuchi et al. [75] postulated that changes in the F-region ray reflection height are more likely associated with geomagnetic storms and travelling ionospheric disturbances while

the change in refractive index of the non-deviative slab of the ionosphere is predominantly produced by enhanced photoionization following a solar flare.

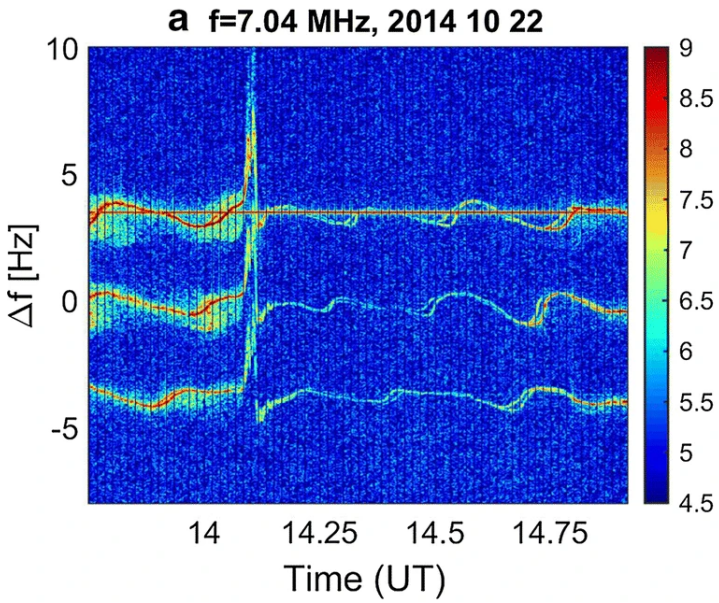

Figure 1.9: Spectrograms recorded by the Continuous Doppler Sounders in the Czech Republic on 22 October 2014 from 13:45 to 14:55 at 7.04 MHz (Image courtesy: [refer to Figure 3(a) of 35]).

1.5.2 Coronal Mass Ejections (CMEs) and Geomagnetic Storms

A coronal mass ejection (CME) is a sudden release of plasma and accompanying magnetic field from the solar corona. CMEs often occur in conjunction with solar flares. The plasma released during CMEs can be observed in coronagraph imagery, e.g. Figure 1.5(c) shows a CME that erupted from the Sun on December 2, 2003.

The plasma ejected by a CME travels through interplanetary space at speeds of ∼300 to 800 km/s and reaches Earth in 2-3 days. The interaction of a CME with the Earth's coupled magnetosphere-ionosphere-thermosphere produces a significant disturbance called a geomagnetic storm. Geomagnetic storms occur when there are many hours of sustained high-speed

solar wind and elevated IMF magnitude. Energy transferred into the magnetosphere drives electric currents and bulk plasma flows that couple to the ionosphere at high latitudes and the auroral region to produce sudden enhancements in ionospheric density via impact ionization. This intense magnetosphere-ionosphere coupling process also creates visible aurora, known as the "northern lights", as shown by the yellow bounded region in Figure 1.10. Sudden enhancements of ionization in the D and lower E-regions of the ionosphere creates an increase in radiowave absorption, commonly known as Auroral Absorption (AA).

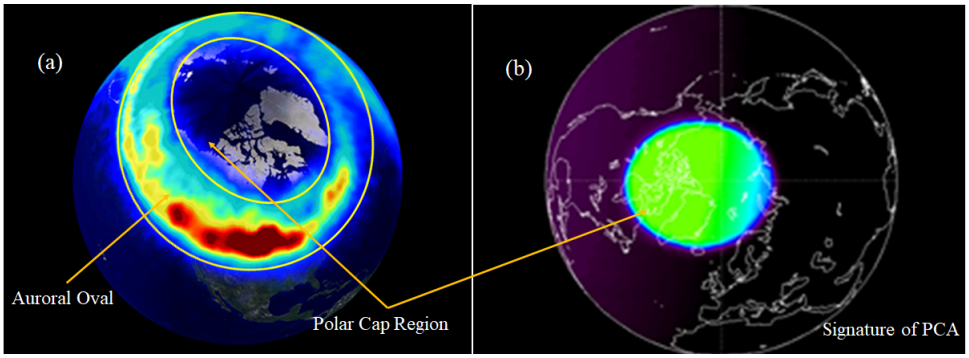

Figure 1.10: Polar view of the Earth showing (a) the extent of the auroral region/oval, visible aurora, and (b) polar cap region with PCA estimated using D-Region absorption prediction model (Image courtesy: University of Iowa and NASA.)

1.5.3 Solar Energetic Proton Events and Polar Cap Absorption

Solar energetic proton events (SEPs) are created when high-energy protons are accelerated during a solar flare or at the leading edge of interplanetary shocks ahead of coronal mass ejections. The protons erupted during SEP events typically carry energies in the ∼keV to GeV range. Figure 1.5(b) presents a coronagraph from the Solar and Heliospheric Observatory (SOHO). The speckles on the image are produced by impacts from SEPs.

Solar energetic protons (SEPs) travel at relativistic speed and take ∼10s of minutes to reach Earth. When the energetic protons enter the magnetosphere they are forced to gyrate around

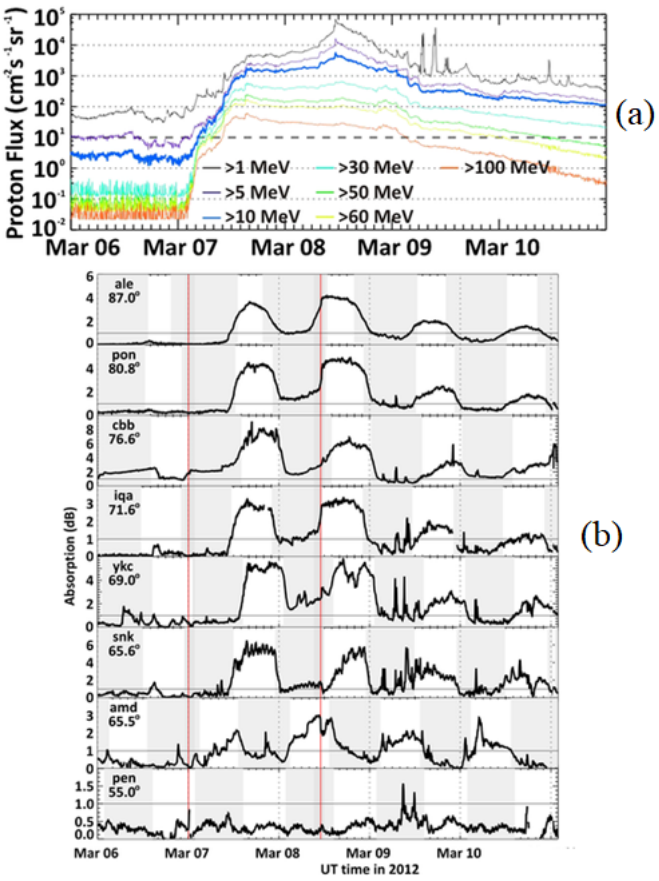

Figure 1.11: (a) >1 MeV, >5 MeV, >10 MeV, >30 MeV, >50 MeV, >60 MeV, and >100 MeV proton flux measured by the GOES 15 geostationary satellite 7-10 March 2012, (b) ionospheric HF absorption observation from the ALE, PON, CBB, IQA, YKC, SNK, AMD, and PEN riometer [refer to Section 1.7] stations (Image courtesy: [adopted from Figure 1 and 2 of 46]).

and travel along Earth's magnetic field lines which funnel them toward the polar regions where they enter the upper atmosphere and create sudden enhancements of ionization via impact ionization. Sudden enhancement of ionization in the D and lower E-regions of the polar ionosphere creates increased absorption of HF radiowave frequencies, commonly known as Polar Cap Absorption (PCA). The region of intense PCA is centered on the magnetic pole and typically bounded by the poleward boundary of the auroral oval (refer to Figure 1.10). Figure 1.11 presents an example SEP event observed near the Earth and the ionospheric

response observed by the passive HF ground instruments located at different latitudes.

1.6 Ionospheric Sluggishness and D-Region Ion Chemistry

The term "Sluggishness" of a system refers to a delay in the system response to any external stimulus. Appleton [9] was the first to describe ionospheric sluggishness as the time delay between the peak in irradiance at solar noon and the peak in ionospheric electron density. Later, the term was used more generically to describe a delay in ionospheric response to any solar driver, specifically to solar flares [44].

Sluggishness can be understood as an inertial property of the ionosphere that is microscopic in nature and thus depends on spatial coordinates, in particular, height. Measurements of sluggishness can provide important information about the ionospheric electron density and ionospheric chemistry. Figure 1.12 presents an example of ionospheric sluggishness observed by a Very Low Frequency (VLF: 3-30 kHz) receiver. Among the three ionospheric layers, the chemistry of the D-region is the most complex. Unlike the E and F-regions, the D-region includes negative ions, water cluster ions, and negative cluster ions. The lower part of the D-region is dominated by these complex ions that participate in various photochemical reactions, which control ionospheric sluggishness. Developing an improved understanding of sluggishness can thus provide new insights into D-region and mesospheric photochemistry and its evolution during solar flares.

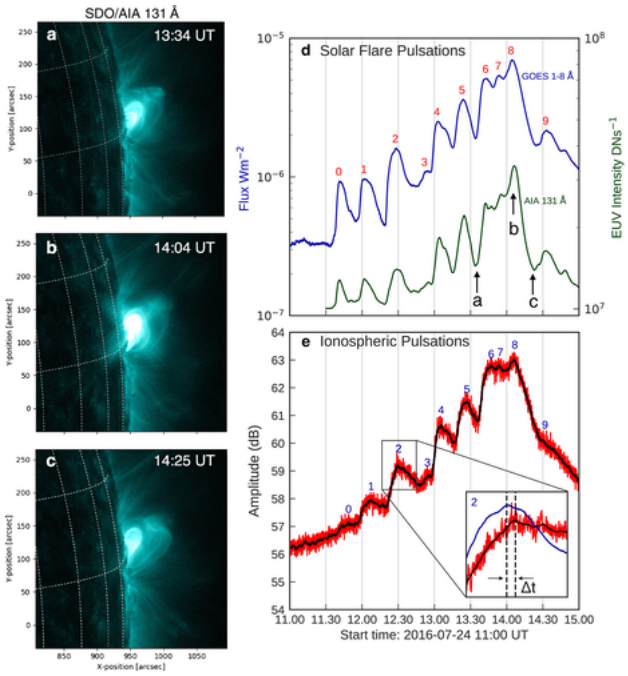

Figure 1.12: Example of ionospheric sluggishness observed by a VLF receiver. Panels (a-c) EUV images from the 13.1 nm channel of SDO/AIA is shown during the (d) three intervals marked by arrows. Quasi-periodic pulsations are evident in both the X-ray and EUV emission in panel (d), while the corresponding D-region response observed using VLF at 24 kHz is shown in panel (e). Panel (e) shows subplot of a zoom in of the pulsation numbered (2) to highlight the time delay (ionospheric "sluggishness") ($\Delta t \sim 90$s) between the X-ray peak and the VLF response. (Image courtesy: [adopted from Figure 1 of 63])

1.7 Instrumentation

In this section, we introduce the instruments and datasets used in this dissertation. The primary datasets are solar flare information from GOES X-ray sensors and observations of ionospheric perturbations following solar flares from SuperDARN HF radars and riometers. The GOES X-ray data provides information about the intensity and temporal evolution of solar flares while the HF radar and riometer data provide information about the ionospheric response to the flares via HF absorption, sluggishness, and frequency deviation across various latitudes and longitudes.

1.7.1 GOES X-ray Sensors

Solar X-ray flux information was obtained from the National Oceanic and Atmospheric Administration (NOAA) GOES 15 satellite [93]. The solar x-ray sensors on the GOES 15 satellite have two channels, namely, hard X-ray (0.05-0.4 nm, HXR) and soft X-ray (0.1-0.8 nm, SXR). The NOAA archive supports high resolution (2s) and low resolution (1-minute) X-ray data. We used 1-minute resolution solar flux information from both X-ray channels for our data analysis.

1.7.2 Super Dual Auroral Radar Network (SuperDARN)

The Super Dual Auroral Radar Network (SuperDARN) is an international network of low-power HF coherent scatter radars designed to probe Earth's ionosphere at middle to polar latitudes and its outward connection to space [33, 57, 112]. The radars measure the Doppler shift in signal backscattered from decameter-scale magnetic field-aligned irregularities at F-region altitudes in the ionosphere, which $\mathrm{E} \times \mathrm{B}$ drift in response to electric fields mapped into the ionosphere from the magnetosphere. Although the network was originally constructed to monitor global-scale plasma convection, other research themes have benefited from the analysis of the data (e.g. mesospheric winds and ultra-low frequency pulsations and waves). Figure 1.13 shows the locations and fields-of-view (FOVs) of currently operational SuperDARN radars in the northern (left) and southern (right) hemispheres. For this dissertation, only data from SuperDARN radars in the northern hemisphere was used.

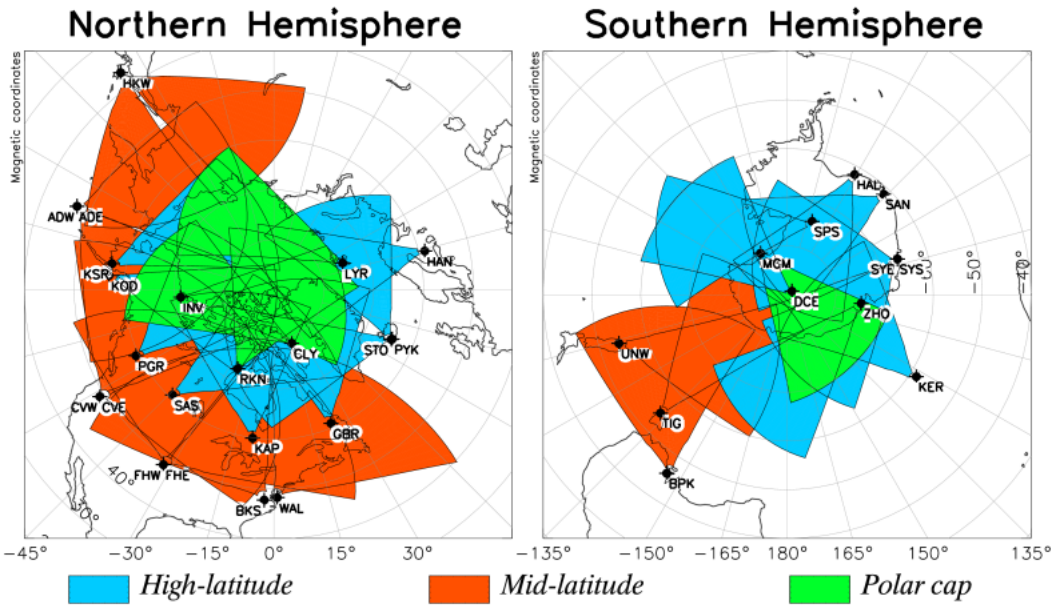

Figure 1.13: Fields of view (FOV) of currently operational SuperDARN radars from the northern (left) and southern (right) hemispheres in magnetic coordinates. Polar cap, high latitude, and mid-latitude radar FOV are shaded in green, cyan, and red, respectively.

1.7.3 Riometers

A riometer is a ground-based passive radio receiver that provides information about HF absorption in the ionosphere by measuring variations in cosmic radio noise at 30 MHz [22, 46, 85]. The cosmic noise absorption (CNA) values used in this study were taken from a network of riometers jointly operated by Natural Resources Canada (NRCan) and the University of Calgary (Geospace Observatory riometer, or GO-RIO) [e.g. 80, 133]. Riometer data from the NRCan and UofC sites were provided at 1s and 5s resolution, respectively. For this study we down-sampled both datasets to 1-minute averages for the purpose of analysis and inference. Figure 1.14 presents the locations of the riometers used. The coverage extends nearly across the full expanse of the Canadian land mass. Note that the three and four letter station codes are associated with riometers operated by NRCan and UoC, respectively.

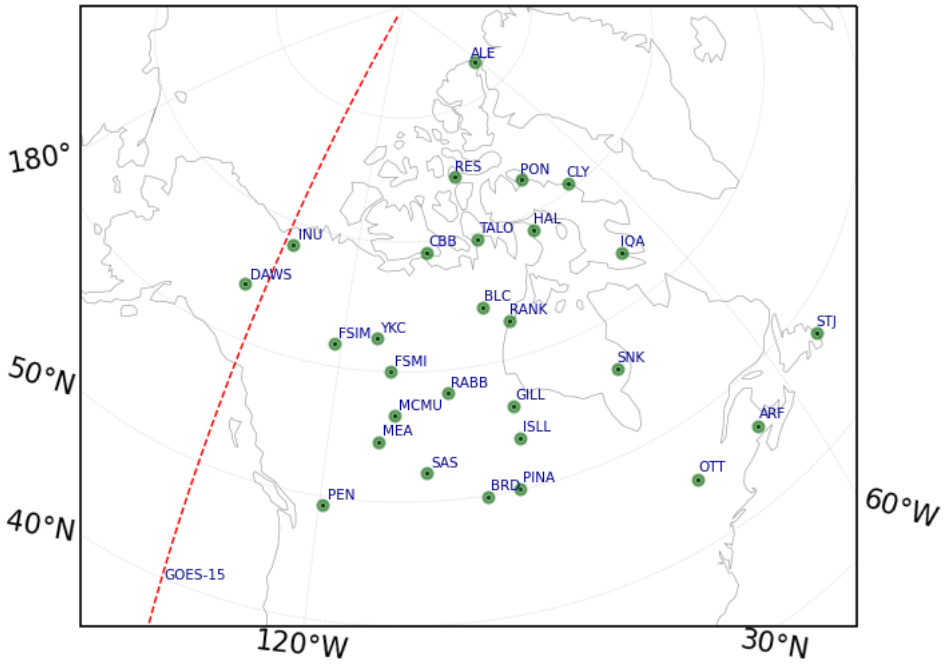

Figure 1.14: Locations of the various riometers used in the study. The black dots identify riometer locations while the green circles represent the 100-km fields-of-view. The red line at -135.3^o longitude indicates the longitudinal location of the GOES 15 satellite.

1.8 Outstanding Research Issues

In this section, we discuss some of the outstanding research issues regarding the ionospheric response to various space weather events, specifically those driven by solar flares, which provided the primary motivation for research described in this dissertation.

1.8.1 HF Absorption During Solar Flares

In section 1.5.1 we explained how solar flare driven sudden enhancement in ionospheric electron density produces SWF. There have been many modeling studies since the late 1960s that aimed to predict the solar flare impact on the ionosphere using data-driven or physics-based models, specifically the HF absorption part of the SID [42, 134, 135, 147]. However,

despite recent advances in our abilities to model and forecast HF absorption, we still do not have a clear understanding of flare time D-region dynamics. The data-driven models only consider solar EUV and X-ray irradiances, solar zenith angle, and operating frequency as input parameters [5, 134, 135]. This is despite the well-known fact that ionospheric HF absorption is strongly dependent on plasma-neutral collisions and the photochemistry at D-region heights (∼60-105 km), factors which are neglected in most of the existing prediction models [162]. Levine et al. [83] showed that during extreme events, one data-driven model underestimates HF absorption by more than 20 dB. Another largely overlooked influence is electron temperature. The study by Zawdie et al. [162] suggested ionospheric electron temperature may be an important parameter through its impact on collision frequency. Accurate estimation of HF absorption may have to include electron temperature as well as a collision frequency model and dispersion relation formulation [162]. We have performed a statistical study that characterizes the signature of solar flare-driven SWF in SuperDARN data using coordinated spacecraft and SuperDARN observations. Finally, we built a physics-based model framework to accurately account for the characteristics of SWF and predict HF absorption experienced by traveling radiowaves.

1.8.2 HF Absorption During Co-Occurring Space Weather Events

In section 1.5.2 we described some other sources of HF absorption, namely geomagnetic storm-driven AA and SEP-driven PCA. Several studies have described and characterized the impact of these geophysical phenomena [46, 73, 77], independently. However, only a handful of studies have addressed the impact of co-occurring events on ionospheric properties, such as HF absorption, temperature, recombination rates, etc. We therefore still do not have a clear understanding how co-occurring space weather events, namely, solar flares, SEPs, and CMEs combine to produce severe impacts on ionospheric properties. We examine the ionospheric

HF absorption experienced by traveling radiowaves following solar flares occurring in quick succession and co-occurring with other space weather events, such as CMEs and SEPs. We use coordinated observations from the geostationary GOES 15 spacecraft and ground-based SuperDARN HF radars and riometers to investigate the ionospheric response to these co-occurring space weather effects. We found that ionospheric response to successive solar flares is non-linear that extends the ionospheric relaxation time and one possible explanation for this phenomenon might be the enhancement in D-region electron temperature.

1.8.3 Frequency Anomalies during Solar Flares

In section 1.5.1, we explained how solar flare driven sudden enhancement in electron density produces SFD. A handful of studies have explored the driving mechanism of this phenomenon [75, 156]. Observations and modeling efforts regarding the manifestation and evolution of the frequency anomaly following a solar flare are very limited. Kikuchi et al. [75] suggested the frequency anomaly could be driven by changes in refractive index in the lower ionosphere or due to lowering of the F-region height. In a later study, Watanabe and Nishitani [156] found that changes in the refractive index is the major driver of the frequency anomaly, while they did not discuss the location of the source in the ionosphere. One objective for this research is to investigate whether first-principles based modeling of HF signal propagation through the flare-modified ionosphere can reproduce radar observations. Such modeling efforts can be used to investigate the primary causes of the frequency anomaly, their relative contributions, and location in the ionosphere. First, we characterize the SFD signature in SuperDARN observations and then use a first principal model framework to investigate the drivers of this SFD. Specifically, we are interested in validating the theory behind the SFD described in Kikuchi et al. [75] and confirming the findings of Watanabe and Nishitani [156]. We found, that changes in the E and F-region refractive indices are

the major driver of the SFD observed by SuperDARN radars and the apparent downward movement of the ray reflection height in the F-region is related to increase in ionospheric refractive index and weakening of the vertical ion-drift.

1.8.4 Solar Flare Effects on D-Region Chemistry

Ionospheric sluggishness measurements are useful because they provide information about the ionospheric electron density and the effective recombination coefficient (α_{eff}). In turn, α_{eff} can be used to understand the ionospheric photochemistry. Appleton [9] determined that sluggishness is inversely proportional to the recombination coefficient. Owing to the variety of recombination processes, it is more appropriate to refer to an effective recombination coefficient, α_{eff}, which is controlled by the atmospheric negative ions (e.g. O^-, O_2^-, NO_3^-, CO_3^-, HNO_3^- etc and their hydrates) and positive cluster ions (e.g. $H^+(H_2O)_n$) [113, 124, 155]. Specifically, α_{eff} defines the effective loss rate of electrons due to cascading photochemical reactions following electron production due to photoionization [117]. Sluggishness measurements, however obtained, can provide insight into D-region and mesospheric photochemistry and can also be used to validate models. Previous studies of ionospheric sluggishness have used very low frequency (VLF: 3-30 kHz) receivers to study the D-region phtotochemistry. We also know that the ionospheric photochemistry influences sluggishness. To our knowledge no studies have determined which chemical reaction is most responsible for producing ionospheric sluggishness. We characterize ionospheric sluggishness observed by ground-based HF receivers and infer useful information related to D-region ion chemistry from a simulation study. Specifically, we compare solar flare observations from a GOES satellite with the ionospheric response from ground-based HF instruments to characterize ionospheric sluggishness and found sluggishness is anti-correlated with zenith angle and solar X-ray radiation intensity. The simulation results suggest that solar flare-driven enhancements in the electron

detachment rate are due to the sudden rise of molecular vibrational and rotational energy under the influence of energetic EM radiation.

1.9 Objectives & Dissertation Organization

This dissertation seeks to characterize solar flare impacts on the ionosphere and to understand the fundamental processes that drive them. The broad objective is to utilize the SuperDARN and riometer observations to study solar flare-driven SIDs and their driving mechanisms. We seek answers to the following science questions:

1. What are the basic *characteristics* of SWF and SFD observed by SuperDARN HF radars?

2. Are flare-driven ionospheric responses *linear* in nature?

3. How does a solar flare alter the *D-region chemistry* and what are the *resulting manifestations* of ionospheric sluggishness?

4. Can we accurately account for the characteristics of SWF in terms of *ionospheric processes* using a physics–based model framework?

5. Which *physical mechanisms* are the dominant factors in generating of the Doppler flash?

This dissertation is organized into seven chapters. Chapter 1 has introduced the background knowledge for this dissertation, such as the solar-terrestrial environment, solar activity features and their impacts on the ionosphere, the instrumentation that will be used, and the research objectives. In Chapter 2, we present a characterization of solar flare-driven SID

signatures in SuperDARN HF radar observations. In Chapter 3, we present an event study during the September 2017 solar storm, which produced multiple co-occurring solar flares, SEPs, and CME driven geomagnetic storms. We analyze SuperDARN and riometer data in conjunction with spacecraft data and report on how the co-occurring space weather activities combine to influence HF absorption. In Chapter 4, we analyze ionospheric sluggishness and show how it is linked to ionospheric chemistry. In Chapter 5, we use a new physics-based modeling framework to estimate solar-flare driven HF absorption and analyze its drivers. In Chapter 6, we use a ray-tracing model framework to estimate the Doppler flash observed by SuperDARN following an X-class solar flare and investigate its generating mechanisms. Finally, Chapter 7 summarizes the conclusions and ideas for future work.

Chapter 2

Characterization of Short-Wave Fadeout seen in Daytime SuperDARN Ground Scatter Observations

S. Chakraborty[1], J. M. Ruohoniemi[1], J. B. H. Baker[1], and N. Nishitani[2]

[1]Bradley Department of Electrical & Computer Engineering, Virginia Tech, United States

[2]Solar Terrestrial Environment Laboratory, Nagoya University, Nagoya 464-8601, Japan

Chakraborty, S., Ruohoniemi, J. M., Baker, J. B. H., & Nishitani, N. (2018). Characterization of short-wave fadeout seen in daytime SuperDARN ground scatter observations. Radio Science, 53, 472– 484. doi:10.1002/2017RS006488

Abstract

Shortwave fadeout (SWF) is a well-known radiowave anomaly which follows Earth-directed solar flares and leads to severe disruption of trans-ionospheric HF systems. The disruption is produced by flare-enhanced soft and hard X-rays which penetrate to the D-layer where they dramatically enhance ionization leading to heavy HF absorption over much of the day-side for an hour or more. In this paper, we describe how Super Dual Auroral Radar Network (SuperDARN) observations can be exploited to analyze SWF events. Superposed epoch analysis of multiple signatures reveals the typical characteristics of SWF. The number of SuperDARN ground-scatter echoes drops suddenly (≈ 100 *seconds*) and sharply after a solar flare, reaching a maximum depth of suppression within a few tens of minutes, and then recovering to pre-SWF conditions over half an hour or so. The depth of echo suppression depends on the solar zenith angle, radiowave frequency, and intensity of the flare. Furthermore, ground-scatter echoes typically exhibit a sudden phase change leading to a dramatic increase in apparent Doppler velocity (the so-called "Doppler flash") which statistically precedes the dropout in ground-scatter echoes. We report here on the characterization of SWF effects in SuperDARN ground-scatter observations produced by several X-class solar flares. We also describe the functional dependence of peak Doppler flash on solar zenith angle, frequency, and peak intensity of solar flux.

Plain Language Summary

This study is about how energetic electromagnetic eruptions (solar flares) coming from the Sun alter the physical properties of the ionosphere which affects the over the horizon high-frequency (HF) radio communication channels, commonly known as short-wave fadeout (SWF). The study characterizes different facts and features of SWF seen in daytime observations of the SuperDARN HF radar (a monostatic HF transceiver system, which simulates a two-way HF communication link) during different solar flare events. The article also demon-

strates how the physical location of HF transmitter/receiver, HF transmitter frequency, and intensity of solar flare impacts SWF.

2.1 Introduction

A solar flare event is a sudden increase in brightness observed near the Sun's surface across a broad spectrum of frequencies [103, 110], lasting for a few minutes to several hours. Enhanced fluxes of solar X-rays penetrate deep into in the Earth's atmosphere (reaching down to the D-Region) where they dramatically increase ionization on the day side. This sudden increase of plasma density causes an increase in radiowave absorption [16, 98], which is most severe in the $3 - 30$ MHZ high frequency (HF) ranges, commonly known as Short-Wave Fadeout (SWF). The enhancement of D-region plasma also increases the bending of radiowaves due to changes in refractive index of the ionosphere. Solar EUV and X-rays propagate at the speed of light and take only ≈ 8 minutes to reach Earth's atmosphere, so SWF is one of the earliest space weather effects following a flare. This geophysical phenomenon was first described by J.H. Dellinger in 1935 [40] and a later statistical study DeMastus and Wood [41] showed that there is a one-to-one relation between solar flares and SWF. A recent study by Zawdie et al. [162] showed that plasma density enhancement is the main driver of HF radiowave absorption in D and E layers. Developing an improved understanding of SWF is important because these events have serious effects on trans-ionospheric radiowave systems including ground-to-ground radio communications [39, 45], amateur radio links, satellite communication systems and GNSS [153].

Many instruments have been used to study SWF. In the early 1950's the riometer [105] was the main instrument to study the cause of ionospheric absorption, but recently ISR data [100] have been used to study the increase in D-region ionization more directly. Digisonde

(digital Ionosonde) and GNSS TEC data [3] have also been used to study fluctuations of the ionospheric plasma frequency profile during flare events. Handzo et al. [59] used a Digisonde and ISR-based system to characterize the enhancement of plasma frequency and D-region absorption, whereas Xiong et al. [159] used ionospheric solar flare activity indicator (ISFAI, GNSS TEC data) to characterize flare related anomalies in TEC data. Modeling has been used in an effort to better understand the physics of ionospheric absorption and its variability during SWF events [142]. Eccles et al. [42] used ionospheric radio sounding data to study the characteristics of SWF and as input to a data-driven photochemical model of D-region absorption. Finally, Watanabe and Nishitani [156] used SuperDARN radar data to study SWF and establish the fact that Doppler characteristics of SWF observed on HF radar are highly correlated with D-region plasma enhancement. Despite these efforts the physics behind SWF is not yet fully understood and tools for widespread monitoring of SWF effects on HF propagation are lacking.

In this paper, we present a comprehensive statistical characterization of SWF using the SuperDARN HF OTH radar system. Specifically, we characterize SWF events in terms of solar zenith angle, transmitted frequency, and flare intensity, and examine the timings of SWF across the dense sub-network of SuperDARN radars in North America. We discuss one illustrative event study in detail and present some statistical characteristics of SWF events seen in SuperDARN radar observations.

2.2 Instrumentation: SuperDARN

The Super Dual Auroral Radar Network (SuperDARN) is a network of high-frequency (HF, $8-20\ MHz$) radar designed to probe the Earth's ionosphere and its relationship to space [33, 57]. SuperDARN radars measure the line-of-sight (LOS) velocity component of the F-

region drift of ionospheric plasma when decameter-scale electron density irregularities are present and oriented favorably to produce backscatter. Although the network was originally constructed to image the high-latitude auroral zone, it has recently been expanded to middle latitudes. Figure-2.1 shows the dense sub-network of middle and high latitude SuperDARN radars in the North American sector used for this study. Also, the large spatial extent and continuous operation of SuperDARN radar chain makes it a perfect network for detecting and monitoring the flare effects in real time.

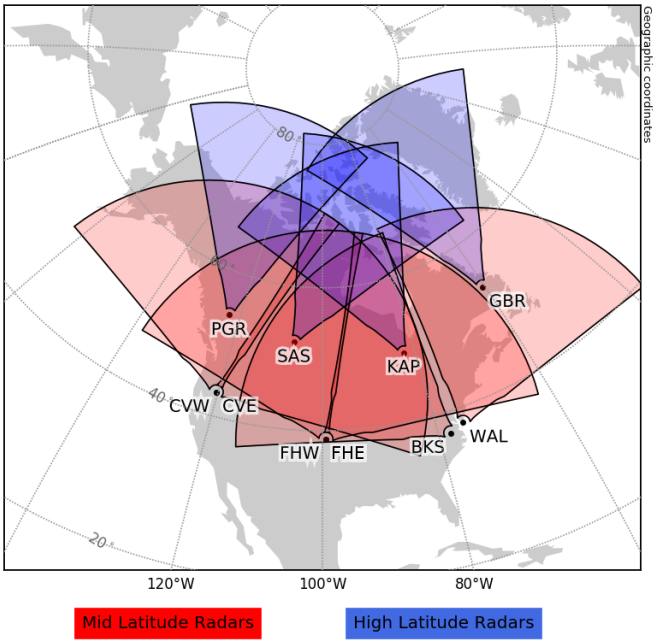

Figure 2.1: Fields-of-view (FoV) of SuperDARN radars located at middle (red) & high (blue) latitudes used in this study. The radars are Prince George(PGR), Saskatoon (SAS), Kapuskasing (KAP), Goose Bay(GBR), Christmas Valley East and West (CVE, CVW), Fort Hays East and West (FHE, FHW), Blackstone (BKS), Wallops Island (WAL).

SuperDARN radars observations primarily consists of two types of backscatter signals, namely, ground scatter and ionospheric scatter as shown in Figure-2.2a and b. Figure-2.2(a) shows how ground scatter and ionospheric scatter are generated in the HF radar observations. In the case of ground scatter (corresponds to ray (1) of Figure-2.2a), due to vertical gradient in refractive index the ray bends towards the ground and is reflected from

the surface roughness and returns back to the radar following the same path. This simulates a complete 1-hop ground-to-ground HF communication link, which passes through the D-region 4 times. Ionospheric scatter (corresponds to ray (2) of Figure-2.2a) is due to the reflection of signal from ionospheric plasma irregularities and are associated with relatively higher Doppler velocities and wider spectral width. Figure-2.2b presents a SuperDARN field-of-view (fov) Doppler velocity scan plot from the Blackstone radar showing ground scatter (in gray) and ionospheric scatter (in color) color-coded by Doppler velocity. During daytime SuperDARN observations typically feature a band of ground scatter that extends over several hundred kilometer range. The effects of SWF can be easily identified in this ground scatter band. To select the ground scatter we identified SuperDARN observations having relatively low Doppler velocity (within $\pm 10\ ms^{-1}$ range) and, narrow spectral width. Typical daytime ground scatter band lies within the slant range $> 900\ km$ and $< 2000\ km$ from slightly after the sunrise to sunset.

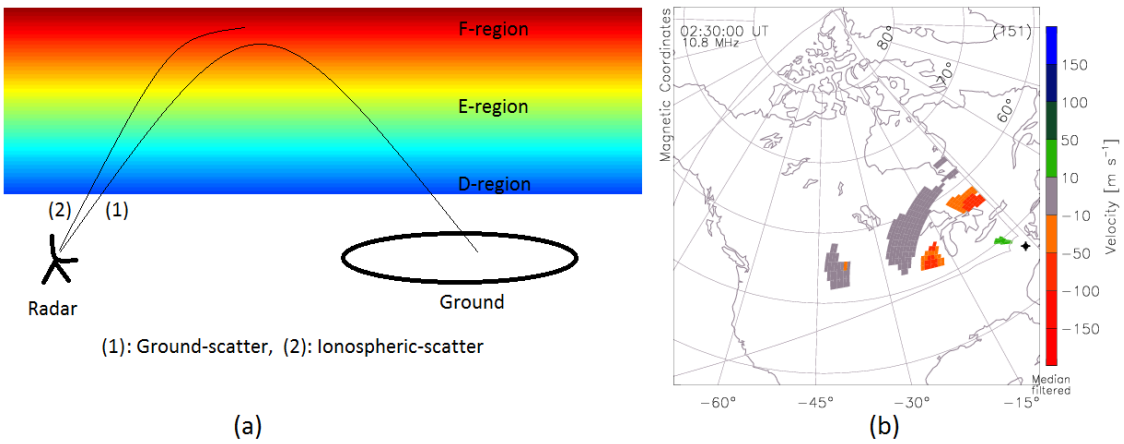

Figure 2.2: (a) Schematic plot of SuperDARN radar show ray-paths of ground-scatter and ionospheric-scatter, (b) SuperDARN FoV scan plot, showing line-of-sight (LoS) Doppler velocity measured by the Blackstone radar on May 31^{st}, 2017 at 2:30 UT. Velocity is color coded according to the scale on the right and ground scatter is marked gray.

2.3 Results

This section is split into two subsections: (1) a case study of an SWF event which occurred in response to an X class solar flare ($X2.7$) on May 5^{th}, 2015 at 22:10 UT and (2) a statistical study of multiple SWF signatures observed by SuperDARN radars across North America.

2.3.1 Event Study: An Example of Short-Wave Fadeout on May 5^{th}, 2015

In this part we present an event study of an X-class solar flare signature in SuperDARN data. Figure-2.3 presents a typical example of an SWF event seen by the Blackstone radar in response to a solar flare measured by GOES spacecraft at 22:10 UT on May 5^{th}, 2015. The upper 9 panels (Figure-2.3a) present a series of FoV scan plots of LoS Doppler velocity at 4-minutes cadence, while the lower two panels (Figure-2.3b) show range time plots of received power and Doppler velocity on beam 7. Figure-2.3a shows a complete wipeout of backscatter signal at 22:12 UT, consistent with SWF, while Figure-2.3b shows the SWF phenomenon lasts about an order of 10s of minutes and gradually restores back to normal (pre-SWF) condition with some negative shifts in Doppler velocity. Also noteworthy is the fact that, the radio blackout event was preceded by a sudden enhancement of apparent backscatter Doppler velocity at 22:08 UT, which is evident in both Figure-2.3a and Figure-2.3b. Because this "Doppler Flash" signature is embedded within a robust band of pre-existing ground scatters, it must be associated with a sudden change in the environmental condition along the ray path due to change in phase path length (due to ionospheric properties, such as refractive index) and not to a displacement of the ray path itself.

Figure-2.4 compares the Blackstone (BKS) measurements to GOES X-ray fluxes. The event

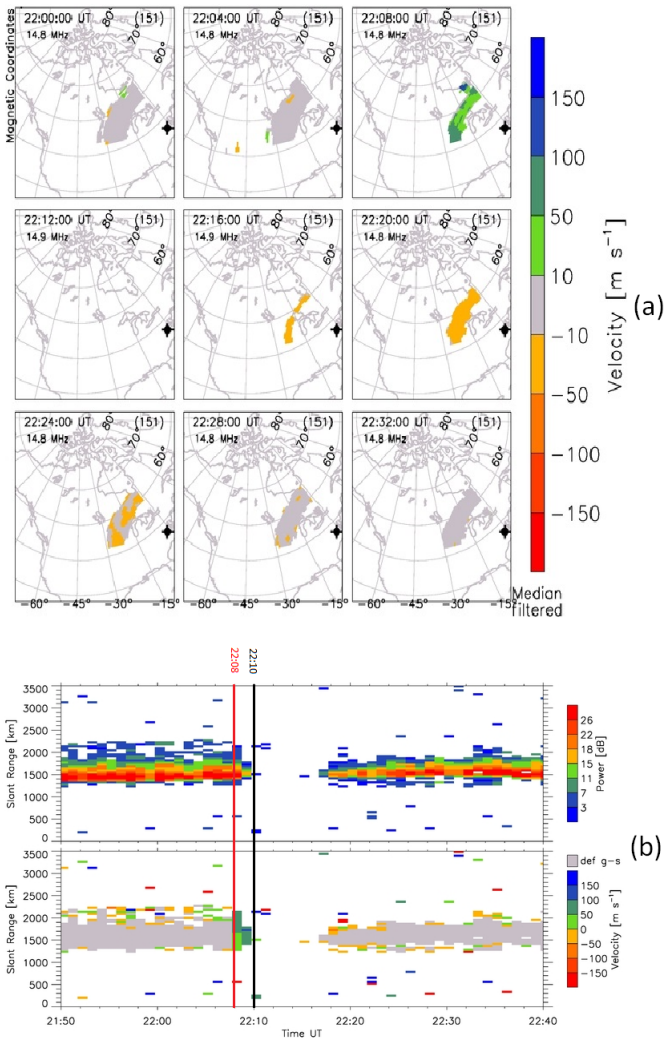

Figure 2.3: Response of the Blackstone radar to a solar flare on May 5^{th}, 2015: (a) Series of FoV scan plots of LoS Doppler velocity color coded according to the scale on the right and (b) Range-Time (RTI) plot showing backscattered power (top panel) and Doppler velocity (bottom panel) on beam 7, color coded according to the scales on the right. The vertical line denotes the start of the Doppler flash in red and start of the radio blackout phase in black respectively.

can be seen to initiate at 22:06 UT when the GOES X-ray sensor observes a sudden increase in solar X-ray flux (panel (a)), and BKS starts to observe a decrease in average received power (panel (b)) and number of ground scatter echoes (panel (c)) leading to a total wipeout of radio link about 10 minutes and a gradual recovery over $30 - 60$ minutes. Finally, panel

(d) shows the "Doppler Flash" signature peaks at a value of $80 - 100\ ms^{-1}$ on a similar timescale as the SWF. We discuss the physics behind this Doppler phenomenon in the Discussion section. The vertical red line passing through all panels represents SWF "onset time" when a significant depletion in the number of ground scatter echoes first detected. Other vertical lines in panel (c) represent "radio blackout start time" (black), "onset of recovery time" (blue) and "recovery time" (green) of the SWF phenomenon. The radio blackout start time corresponds to nearly complete suppression ($\geq$ 80% reduction) in the number of ground scatter echoes; the onset of recovery time corresponds to the beginning of the recovery phase ($\geq 25 - 30\%$ increase); and the recovery time corresponds to the time when ground scatter reaches almost back to pre-existing conditions ($\geq$ 95% of pre-SWF count). More importantly, the event onset timing matches the time of solar flare onset. In this particular case, the duration of the onset, blackout ,and recovery phase are 1.4, 13.9 and 26.3 minutes respectively.

SWF is a day side phenomenon and most impactful at the sub-solar point, so, here we are going to examine the solar zenith angle effect on SWF signature. Figure-2.5 shows the impact of solar zenith angle (SZA, χ) on the intensity and duration of SWF [Note that, radars are operating at different frequencies]. Applying simple analogy of ground scatter propagation, radio signal crosses D region 4 times at 2 different location (assuming the outbound EM wave ray path is same as inbound ray path), one is near to radar another is near to target (ground scatter). Our goal is to characterize the features of SWF in terms of single SZA, which can incorporate the effects of 2 D-region passes. We took the average SZA of these two points to represent a single SZA. Also note that, the variability of SZA two points is much smaller ($\approx 10\% \approx 2^o - 3^o$) than the variation in SZA of different radar sites for individual events. Vertical lines passing through each panel show phase timings of SWF observed by individual radar. Red, black, blue and green lines represent onset, blackout, start of recovery

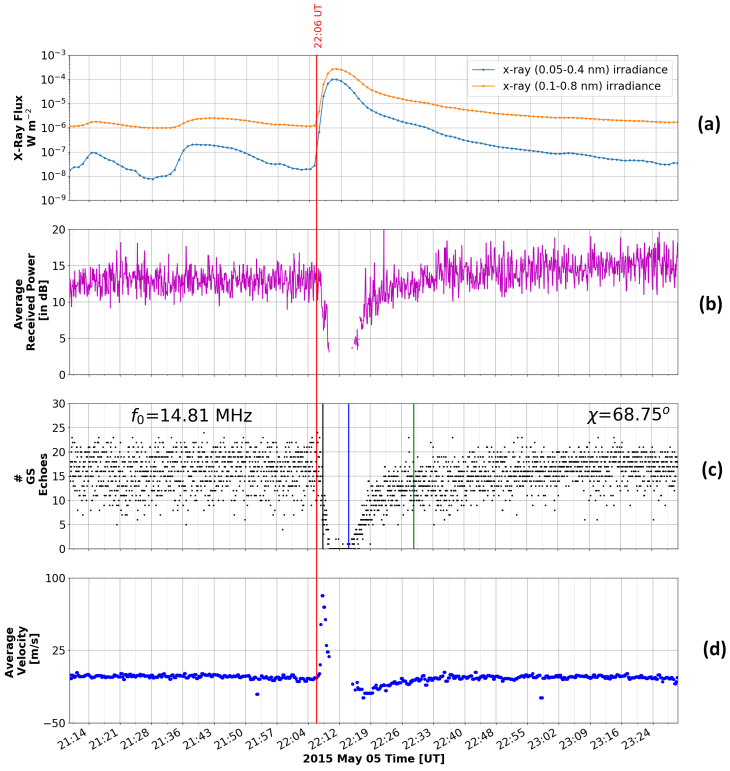

Figure 2.4: GOES and Blackstone(BKS) radar measurements during a solar flare & associated SWF event on May 5^{th}, 2015 : (a) GOES X-ray flux 0.1-0.8 nm (orange) and 0.05-0.4 nm (blue) wavelength bands, (b) average backscatter BKS power, (c) average number of BKS ground scatter echoes and (d) average BKS LoS Doppler velocity. Vertical lines in panel (c) represents onset time (red), blackout start time (black), blackout end time (blue) and recovery time (green). The radar operating frequency (f_0) and solar zenith angle(χ) are provided. The red line passing through all the panels represents the event commencement timing (22:08 UT). See section 3.1 for details.

and end of recovery respectively. Radars located closest to the sub-solar point (e.g. PGR & CVW) are impacted more severely than the radars located further away from the subsolar point (e.g. GBR & BKS), indicating that SZA controls the intensity of SWF signatures. Effects can be seen in the duration of the event, as well as in the durations of blackout and recovery phases and the depth of the blackout phase (% change in the number of ground scatter during the blackout phase). Also, note that the recovery of the radars having smaller SZA (e.g. PGR & CVW) is more gradual than that of radars with higher SZA (e.g. BKS &

GBR).

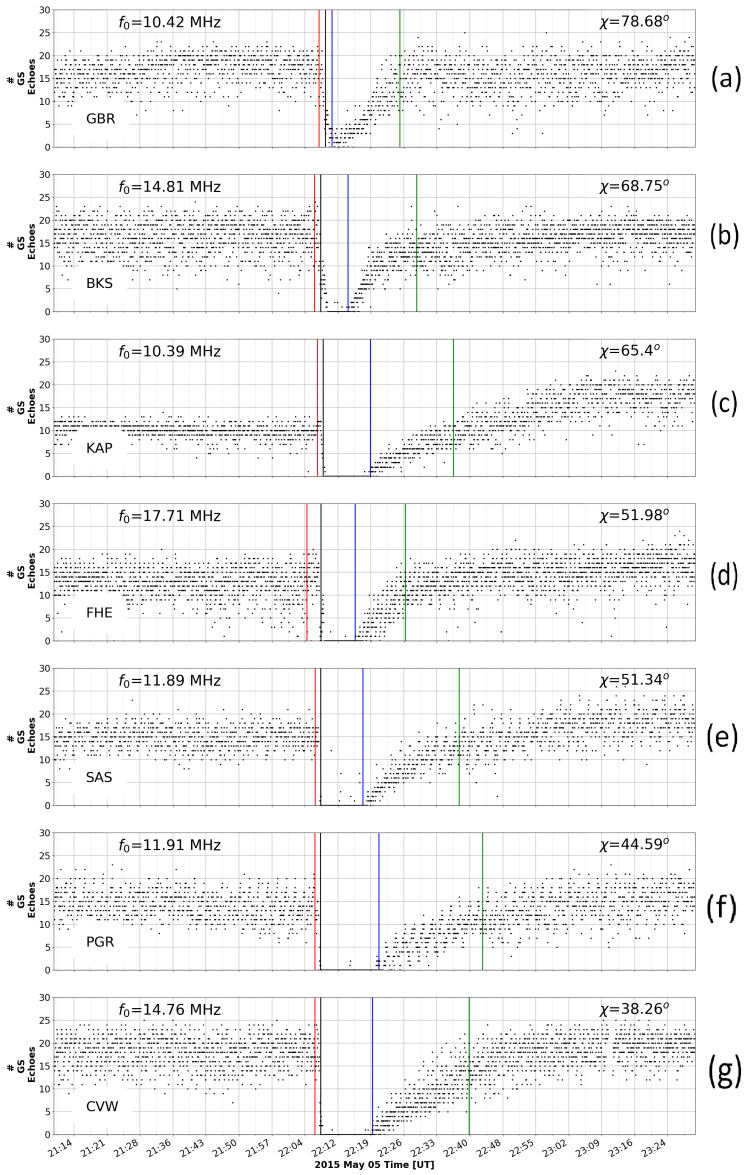

Figure 2.5: Multi-radar time series of the ground scatter echoes during a SWF event on May 5^{th}, 2015 observed by the (a) GBR, (b) BKS, (c) KAP, (d) FHE, (e) SAS, (f) PGR, and (g) CVW radars. Similar format to Figure-2.4(c).

Just like SZA, frequency of the propagating radiowave also alters the signatures of SWF. The non-deviative absorption of a radiowave in the ionosphere has an inverse 2^{nd} power dependency on the frequency of the radiowave, so the lower the frequency of radiowave,

more it is attenuated. Figure-2.6 compares the response of SWF between two radars with similar SZA but different operating frequencies. A stronger SWF response was observed by the radar operating at a lower frequency (KAP) and the recovery phase was more gradual. Taken together, both figures show neither SZA nor operating frequency plays a major role in influencing the timing and duration of onset phase.

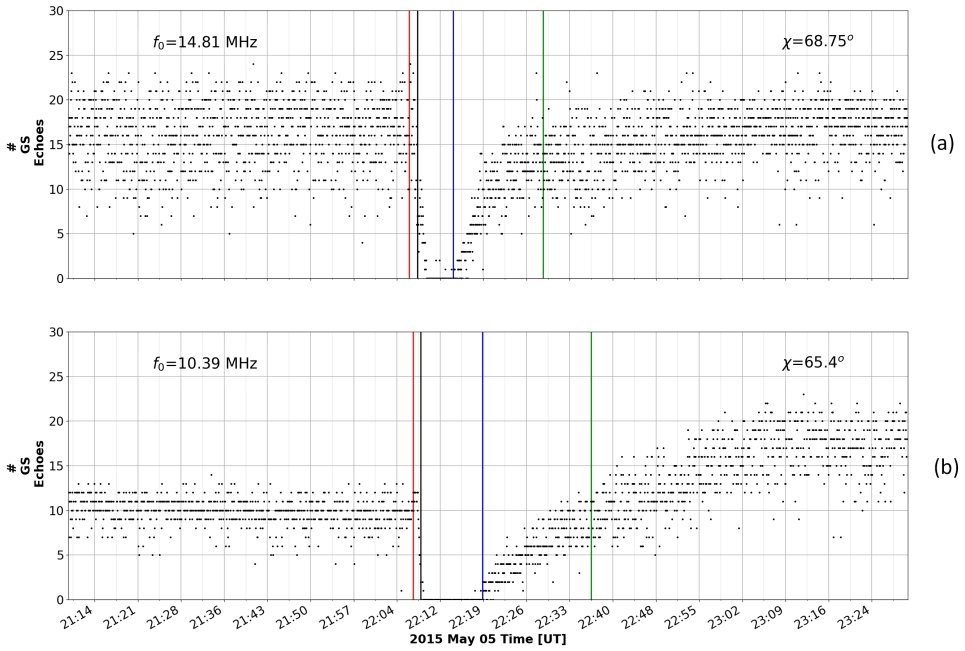

Figure 2.6: Comparison of ground scatter echoes during a SWF event on May 5^{th}, 2015 observed by the (a) BKS and (b) KAP radars. Similar format to Figure-2.4(c). These measurements correspond to similar solar zenith angle(χ) but different radar operating frequencies(f_0).

2.3.2 Statistical Results

In order to characterize statistical behavior of SWF signatures in SuperDARN data, we choose 9 different X-class events from $2013 - 2015$. We consider GOES X-ray sensor instruments as our reference to identify these events. Table-2.1 provides a list of event times, event duration and solar flare class associated with all the events used in this statistical study.

Each event generally lasts for ≈ 50 minutes to an hour and half and affects 5 radars on average, so a total of 52 SWF signatures were analyzed from SuperDARN radars across the northern hemisphere. Figure-2.7 shows an analysis correlating the durations of SWF phases with SZA, radiowave frequency, and solar flare intensity. It can be seen that onset phase (upper row) has a very weak dependence on all these parameters, blackout and recovery phase duration is mainly depends on SZA (left column). Also, SZA has a negative correlation with all phase durations, i.e. with SWF impact gets mitigated with increasing SZA. Again, frequency (middle column) and solar flare intensity (right column) show relatively less influence on the phase durations.

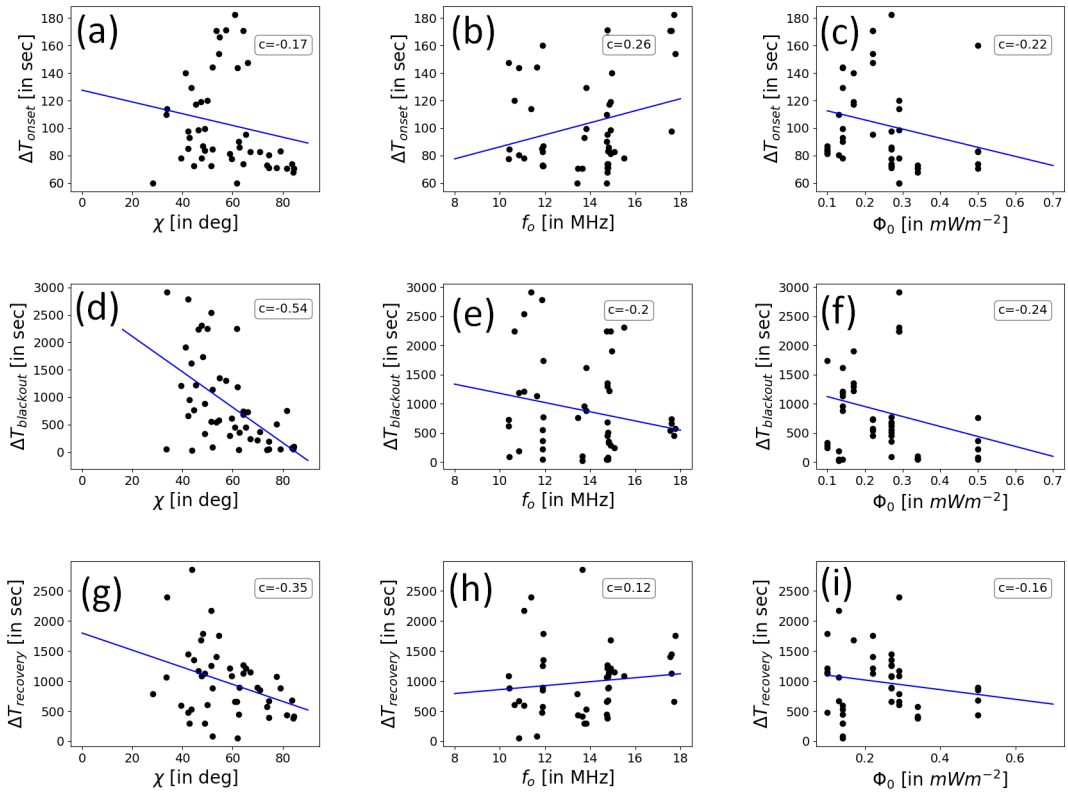

Figure 2.7: Scatter plots of duration of onset phase ΔT_{onset} (upper row), duration of blackout phase $\Delta T_{blackout}$ (middle row) & duration of recovery phase $\Delta T_{recovery}$ (lower row) versus SZA(χ) (left column), operating frequency(f_0)(center column) and solar X-ray flux (Φ_0) (right column). Blue lines show the best fitted value and the associated correlation coefficients are also provided inside each panel.

In order to describe different phases of SWF as a linear of SZA, frequency and peak solar flux we do a multiple linear regression analysis. Figure-2.8 shows multiple linear regression models of the phase durations as a function of the physical parameters discussed above. The models do a reasonably good job reproducing the durations of blackout and recovery phase (i.e. the correlation coefficient is high) but not so well for the onset phase [Note that, based on the analysis of Figure-7 it is expected that none of the parameters χ, f_0 and Φ_0 can describe onset phase].

Table 2.1: Events list for statistical study

Event (UTC)	Duration (minutes)	Flare Class
2015-05-05 22:10:00	90	X2.7
2015-03-11 16:22:00	90	X2.2
2014-09-10 17:45:00	60	X1.7
2013-05-13 16:05:00	75	X2.9
2014-03-29 17:48:00	50	X1.0
2014-02-25 00:49:00	70	X5.0
2014-04-25 00:27:00	70	X1.4
2013-05-15 01:48:00	80	X1.3
2013-11-05 22:12:00	130	X3.4

[a]Events are associated with X class flares.
[b]On an average 5 radars are affected by these each of these events.
that gives total = 52 radar events.

In order to find the typical durations of the SWF phases and characterize average radar observations we do an superposed epoch analysis on 52 radar signatures. Figure-2.9 shows a superposed epoch analysis of all SWF events, taking maximum absorption time (radio blackout start time) as the key time (0.0 hr). The first three panels are color-coded by SZA, frequency, and solar flare intensity, while the last panel shows the average duration of the three SWF phases. The black thick line passing through all panels is the mean value of all events, while the standard deviation error bars given in red and thin color lines are for the individual events. In panels $(a) - (c)$ all event signatures lying below the black line (average signature) have a more severe impact. Brighter colors correspond to higher values

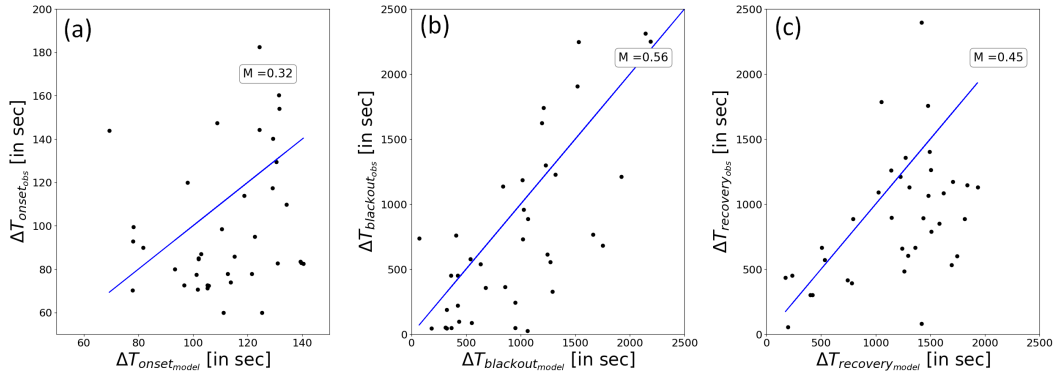

Figure 2.8: Multiple regression scatter plots of predicted (a) ΔT_{onset}, (b) $\Delta T_{blackout}$ and (c) $\Delta T_{recovery}$ versus corresponding measured values from a multiple linear regression model. Blue lines show the best fitted values and the correlation coefficients are provided inside each panel.

of SZA, frequency and flare intensity. Based on the correlation coefficients obtained by the statistical study we can conclude that SZA is the dominant parameter, which is consistent with Figure-2.7. Panel (d) shows the mean duration of different phases for any typical SWF event (average values), are 100 seconds, 10 minutes 33 seconds and 41 minutes 45 seconds for onset, radio blackout, and recovery phase respectively.

Next, we examine the statistical behaviors of the Doppler flash feature of SWF. Figure-2.10 shows a statistical analysis of the Doppler flash phenomenon. Figures-2.10(a)-(c) are scatter plots of peak Doppler velocity versus SZA, radiowave frequency, and solar flare intensity. It can be seen that the peak value of the Doppler velocity has a relatively weak dependence on SZA (panel (a)) and solar flare intensity (panel (c)), but stronger dependence on frequency (panel (b)). Also, SZA and frequency have a negative correlation, i.e. with increasing SZA, peak Doppler velocity value decreases, while it increases with peak flare intensity.

Figures-2.10(a) -(c) show scatter plots of Doppler velocity versus SZA, frequency and peak solar flux respectively. In order to obtain the individual functional forms of peak Doppler Velocity with respect to SZA, frequency and peak solar flux, we can simply integrate the

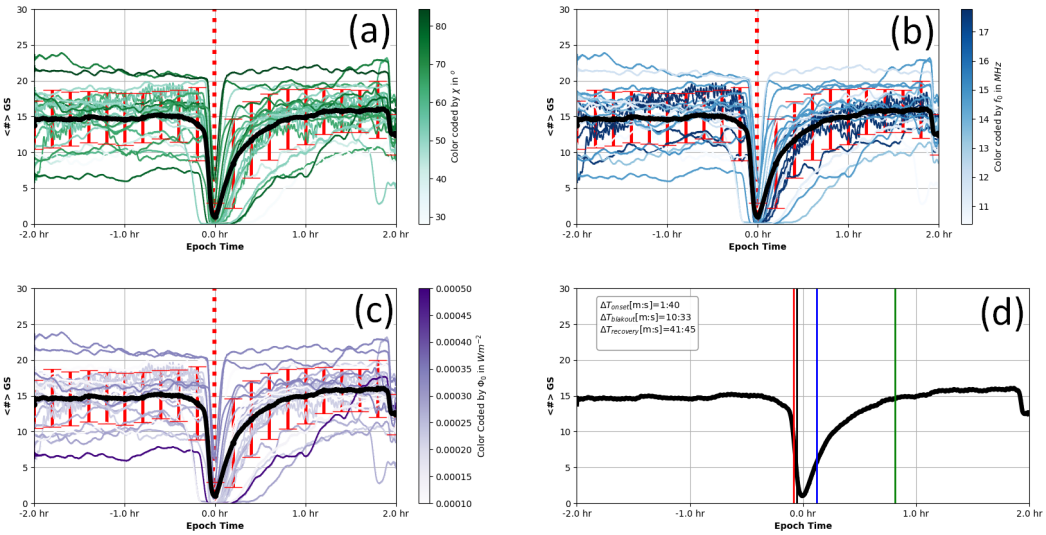

Figure 2.9: Superposed epoch analysis of ($\approx$ 52) SWF signatures seen by SuperDARN radars during the 9 X-class solar flares listed in Table-2.1. Panels (a)-(c) respectively show the ground scatter echoes color coded by SZA(χ), frequency(f_0) and solar X-ray flux Φ_0. Panel (d) shows average timings of onset (red), blackout start (black), blackout end(blue) and recovery (green). Duration of each phase is also provided inside the panel.

Doppler velocity with respect to any two parameters among χ,f_0 and Φ_0 considering other parameter constant. Figures-2.10(d)-(f) shows the functional dependencies of velocity with SZA, radiowave frequency, and solar flare intensity respectively. Doppler velocity provides the proxy measure of decrease in phase path length which is the effect of decrease in refractive index or increase in plasma density (plasma frequency). Assuming the ionospheric density conforms to a Chapman function and making use of binomial approximation (on the nondeviative absorbing D-layer)[39], the refractive index can be expressed as:

$$\eta \approx 1 - \frac{k}{2}\frac{g\,(\Phi_0)}{f_0^2} e^{1-z-\sec\chi e^{-z}} \tag{2.1}$$

where, k is constant, z is the scale hight and (Φ_0) is the functional dependence of incoming solar flux and ionization, which is typically linear for fixed wavelength. To extract the functional dependence of η only on each of the physical parameters we can simply average

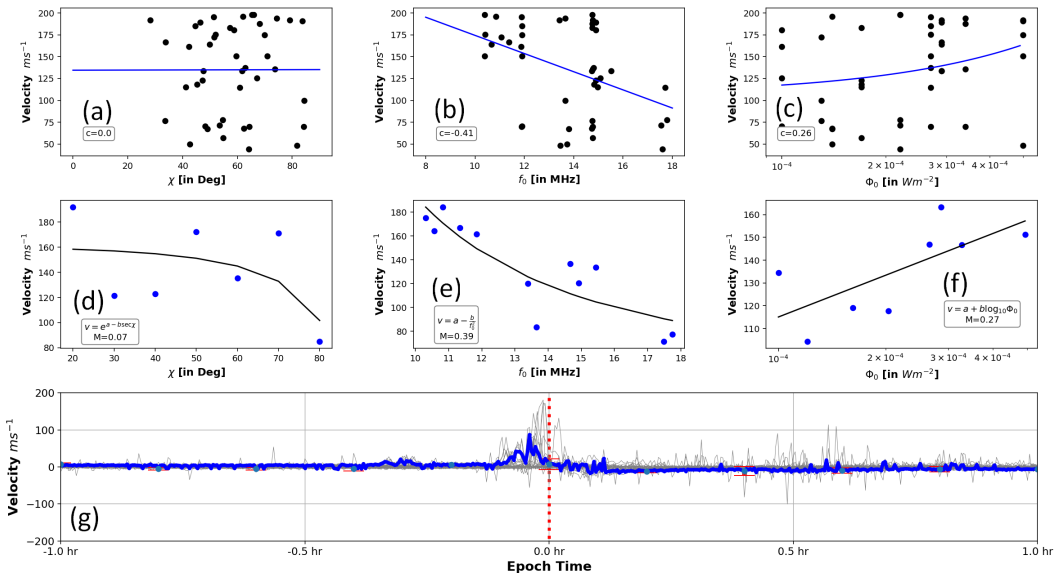

Figure 2.10: Statistical analysis of peak Doppler flash data from multiple events. Panels (a)-(c) respectively show scatter plots of peak Doppler flash versus SZA (χ), frequency(f_0) and solar X-ray flux Φ_0. Blue lines show the best fitted values and the correlation coefficients are provided inside each panel. Panels (d)-(f) show the functional dependence of peak velocity with only SZA (χ), only frequency(f_0) and only solar X-ray flux Φ_0 respectively (see text for details). Black lines show the best fit curves, while the box inside the panels shows the functional forms and the multiple linear regression correlation coefficients. Panel (g) shows a superposed epoch analysis of SuperDARN Doppler velocity using radio blackout as the key time (vertical dashed red line, 0.0 hr).

out the effects of other parameters from the equation-2.1 by taking the arithmetic mean. Figure-10(a)-(c) show variability of the peak velocity with χ,f_0 and Φ_0 along the x-axis accordingly, and the variability in the dataset along the y-axis is due to other parameters (f_0,Φ_0),(χ,Φ_0)and (χ,f_0). So, to obtain the functional form of the peak Doppler velocity we binned the data into small groups with respect to χ,f_0 and Φ_0 respectively, and then used the average values (Doppler velocity) of the data to represent the velocity for that bin. Note that, if a bin does not have data then we replace that dataset by NaN (Not-a-Number) values. The functional dependence of η with SZA, frequency and solar flux are $e^{a-b\sec\chi}$, $a-\frac{b}{f_0^2}$ and $a+b\log_{10}\Phi_0$ respectively. Applying this approach yields Figures-2.10(d)-(f), where black lines show the fitted functional forms which are reasonably close to the measured velocities.

In order to examine the timing of the Doppler flash relative to the SWF we did a superposed epoch analysis of multiple events. Figure-2.10g shows superposed epoch analysis of all Doppler flash events, taking maximum absorption time (radio blackout start time) as the key time (0.0 hr). The blue thick line is the median value of all events, while the standard deviation error bars are provided in red. Panel (d) shows the Doppler flash consistently occurs before the radio blackout phase (red dashed line) and reaches a typical value of $90-100$ ms^{-1}.

2.4 Discussion

In this paper, we have provided a characterization of SWF signatures detected by SuperDARN radars in response to 9 X-class solar flares occurring in $2013-2015$. In this section, we summarize the main findings and compare the results to other pertinent studies.

SWF is the most significant effect seen by any HF communication system following a solar flare event. Figures-2.2−2.6 show evidence of decreased backscatter signal most likely due to increased D-region absorption [98]. The signature of SWF in SuperDARN daytime observation has three distinct phases, namely, onset, radio blackout, and recovery, with typical durations of 100 seconds, 10 minutes and 42 minutes respectively. The duration of the SWF phases is influenced strongly by SZA (χ), radar frequency (f_0) and flare intensity (Φ_0). Among these, SZA and radar frequency effect the evolution of the SWF signature across the radars as shown in Figures-2.5−2.6, while flare intensity has a relatively smaller contribution. The reason behind the relatively small correlation between the X-ray flare intensity and the features of SWF (durations of onset, blackout and recovery) is due to the fact that study only focuses on the peak value of the X-ray flux not the integrated flux (area under the flux curve which is equivalent to the total energy deposited to the upper

atmosphere due to the flare enhanced X-ray flux) and also we do not consider energy deposition due to enhancement of flux in EUV spectrum. Hence, statistical results also showed strong dependencies on SZA and frequency but weak dependency on X-ray peak intensity in Figures-2.7−2.9. The previous study by Xiong et al. [159] showed that ionospheric solar flare activity indicator (ISFAI, TEC data) has a high statistical correlation with the solar zenith angle. Our results also reveal the fact that onset phase is nonlinear in nature and does not depend on any of the physical parameters. Flares are traveling at the speed of light and the first impact flare takes almost no time to spread its effects from sub-solar point to the edge of the sunlit part of the ionosphere, which is the reason of the dramatic initial effects of SWF. Hence SZA, frequency and solar peak flux intensity have no effect on onset phase. The intensity of the event is also modified by the radiowave frequency as shown in Figure-2.6. Radars operating with low frequency are more vulnerable to SWF events which are also consistent with the HDIVE experiment and ABBY Normal model study done by Eccles et al. [42]. Previous statistical study Le et al. [81] related to flare peak and effects of ionosphere shows that X-ray peak intensity has a very low direct correlation with the effects on the ionosphere, which is also consistent with our results. Moreover they also showed that X-ray flux is not a good proxy of EUV flux which is a direct measure of flare-driven ionospheric anomalies and a central meridional distance adjustment leads to a better correlation between flare time X-ray and EUV fluxes. The reason behind the relatively small correlation coefficient between the X-ray flux and the radar peak Doppler velocity is due to the fact that we only considered peak value of the X-ray flux not the integrated flux and also we do not consider energy deposition due to enhancement of flux in EUV spectrum. Also noteworthy that Xiong et al. [159] showed that ionospheric solar flare activity indicator has a higher correlation with EUV flux. Unlike onset and radio blackout phase, recovery is quasi-linear and more gradual in nature. These results can be used to test empirical and physics-based models. Also, a detailed modeling of the SWF may reveal different parameters

such as ionization rate, response time and recombination rate of the ionosphere and their variability with physical constraints like χ, f_0, and Φ_0.

One of the most interesting features of the SWF signature is the Doppler flash prior to the blackout. Figure-2.4d shows a clear example, while Figure-2.10 presents some statistics and functional forms of Doppler flash with physical parameters. Specifically, we found the peak value of the Doppler velocity has a weak dependence on SZA and solar flare intensity but a relatively strong correlation with frequency. Superposed epoch analysis in Figure-2.10g shows the Doppler flash peaks before the radio blackout and reaches a typical value of $90-100\ ms^{-1}$. A sudden increase in Doppler velocity generally occurs due to positive phase shift, which implies a reduction in the phase path length of the propagating radiowave due to a sudden change in plasma density (in other words refractive index or plasma frequency and radar frequency) of the ionosphere. We found that the Doppler velocity peak has a relatively higher dependency with radar frequency and the functional forms also shows the same. Kikuchi et al. [75] described this phenomenon using the HF Doppler system data in which Doppler shifts in HF radiowaves during solar flare events are caused by two factors, one is the apparent decrease in the phase path length as a result of the change in the refractive index caused by increasing electron densities in the D-region (non-deviating slab) ionosphere and the other is the phase path length decrease because of the descending reflection point associated with increasing electron density in the F-region ionosphere. A more recent study by Watanabe and Nishitani [156] using SuperDARN Hokkaido radar data found that the decrease in the phase path length was more consistent with increasing electron densities in the D-region. Detailed analysis and modeling of the velocity rise time and peak velocity value may provide further insights about how the ionosphere responds to a solar flare.

2.5 Conclusion & Future Work

The main purpose of this paper has been to statistically characterize the signature of SWF in SuperDARN ground scatter observations in terms of dispersion of phase timings, duration of the phases and depth of blackout and dependencies on physical parameters such as solar zenith angle, operating frequency, and intensity of the solar flare. Another objective was to identify and characterize the Doppler flash feature and provide functional dependence of peak Doppler velocity with zenith angle, frequency, and solar flux. The results show SWF intensity is mostly controlled by solar zenith angle and less by radar frequency and flare intensity, whereas peak Doppler velocity is mostly dependent on radar operating frequency. None of the physical parameters investigated in this study are able to influence strongly the onset phase timing and duration across different radars, while blackout and recovery depend on initial conditions. Several python-based tools have been developed to analyze statistical data, future study will describe how these results can be used for real-time detection of SWF in SuperDARN observations across North America and thus serve as an effective space weather capability for prompt detection and monitoring of impending disruption to HF communications. Future work will also examine how SWF characteristics may depend on season, solar cycle, $F_{10.7}$, and geomagnetic activity indices, also how EM wave propagation through D-region alters under SWF conditions.

Acknowledgments

We thank the National Science Foundation for support under grant AGS-1341918. We wish to acknowledge the use of the NOAA/GOES X-ray Data (from https://satdat.ngdc.noaa.gov/sem/goes/data/) for flare confirmation and analysis. We also thank all participants in the worldwide SuperDARN collaboration for the distribution of SuperDARN data via http://vt.superdarn.org/tiki-index.php?page=Data+Access. The majority

of analysis and visualization was completed with the help of free, open-source software tools such as matplotlib [68], IPython [118], pandas [97], Skifield python API, and others (e.g.,Millman and Aivazis [102]).

Chapter 3

A Study of SuperDARN Response to Co–occurring Space Weather Phenomena

S. Chakraborty[1], J. B. H. Baker[1], J. M. Ruohoniemi[1], B. Kunduri[1], N. Nishitani[2], and S. G. Shepherd[3]

[1]Bradley Department of Electrical & Computer Engineering, Virginia Tech, United States

[2]Institute for Space-Earth Environmental Research, Nagoya University, Nagoya 464–8601, Japan

[3]Thayer School of Engineering, Dartmouth College, Hanover, New Hampshire, United States

Chakraborty, S., Baker, J. B. H., Ruohoniemi, J. M., Kunduri, B. S. R., Nishitani, N., & Shepherd, S. G. (2019). A study of SuperDARN response to co-occurring space weather phenomena. Space Weather, 17, 1351– 1363. doi:10.1029/2019SW002179

Abstract

The Sun was remarkably active during the first week of September 2017 producing numerous solar flares, solar radiation storms and coronal mass ejections (CME). This activity caused disruption to terrestrial high frequency (HF, 3–30 MHz) radio communication channels including observations with the SuperDARN HF radars. In this paper, we analyze the response of SuperDARN ground–scatter observations and decreases in background sky noise level in response to multiple solar flares occurring in quick succession and co–occurring with solar energetic protons and auroral activity. We estimate the attenuation in HF signal strength using an approach similar to riometry and find that the radars exhibit a nonlinear response to compound solar flare events. Additionally, we find the three different space weather drivers have varying degrees of influence on the HF signal properties at different latitudes. Our study demonstrates that in addition to monitoring high latitude convection, SuperDARN observations can be used to study the spatiotemporal evolution of disruption to HF communication during extreme space weather conditions.

Plain Language Summary

High-frequency (HF, 3-30 MHz) communication system plays an essential role in emergency communications such as amateur radio, missile defense, and air traffic control. Most of these systems solely depend on HF communication that can travel beyond the horizon (over the horizon) without any relay or repeater network. This bending of the HF signal is feasible because of the presence of an electrically charged upper atmosphere, also known as ionosphere which can bend the HF signal back to the Earth. This electrically conducting upper atmosphere (ionosphere) can be influenced by the Sun and the outer space, commonly known as space weather. Extreme space weather events such as solar flares, radiation storms, and geomagnetic storms produced by the Sun can alter the state of the ionosphere and disrupt HF communication. During the first week of September 2017, the Sun produced numerous

solar flares, radiation storms, and geomagnetic storms. This paper compares the impacts of isolated versus co-occurring space weather disturbances on HF communications as observed by the Super Dual Auroral Radar Network HF radar network distributed across the North American sector.

3.1 Introduction

Solar activity drives a myriad of space weather anomalies that can disrupt high frequency (HF, 1–30 MHz) communication systems [10, 50, 123]. For example, solar flare–driven Short Wave Fadeout (SWF) [156], Solar Energetic Proton (SEP) event-driven Polar–Cap Absorption (PCA) [46] and geomagnetic storm–driven auroral absorption [56, 94] are well–known absorption effects experienced by radiowaves. While these three phenomena have different physics, driving influences, duration, intensity of absorption, and latitudinal extents, all of them increase ionization in the lower ionosphere either by photoionization or impact–ionization. Enhancement in electron density increases the number of collisions between neutral and charged particles in the D and lower E–regions resulting in increased HF absorption (70–120 km) [16, 162]. SWF exhibits short and intense HF absorption characteristics [18, 27], whereas PCA is relatively longer lasting (typically a few hours to days). Auroral absorption is also a relatively long lived phenomenon and generally intensifies during enhanced geomagnetic activity. It is necessary to understand these phenomena as they impact various facets of modern technology such as air traffic control, maritime and emergency management and amateur radio [10, 50], as well as over–the–horizon radars used in ionospheric research, coastal hazard management, and defense surveillance.

It is rare to find co–occurring solar flare, SEP and CME events and very few studies have reported such events in the past [77, 152]. While early studies analyzed the sources and

characteristics of SWF, PCA, and auroral absorption separately, our understanding of the impacts of such co–occurring events is limited. Additionally, most of the absorption forecasting models such as The ABsorption BY the D and E Region of HF Signals with Normal Incidence (ABBY Normal) and the D–Region Absorption Prediction (DRAP2) are either limited to predicting the impacts of isolated events [42] or apply linear superposition to quantify the radiowave absorption from overlapped space weather events [135]. A handful of studies have analyzed the ionospheric response to co–occurring space weather events [2, 63] but none have analyzed the ionospheric response during the periods when all three events (solar flare, SEP, geomagnetic storm) occur simultaneously.

Since the early 1960s, riometers have provided valuable insights into HF absorption [46, 47, 58, 130]. In recent times the availability of new datastes such as SuperDARN and GPS TEC have provided excellent opportunities to further analyze the effects and impacts of space weather on HF absorption. TEC datasets were utilized by Linty et al. [84], Berngardt et al. [18], and Gonzalez-Esparza et al. [55] to analyze the impacts of solar flare and CME–driven space weather phenomena on communication systems. Specifically, the studies used phase scintillation index, differential TEC, and rate of TEC index (ROTI) to characterize the impact of different space weather impacts on ionospheric propagation conditions. Some studies have proposed applying newer models, methodologies, datasets and instrumentation (both ground–based and space–borne) to forecast the effects and impacts of various space weather events [38, 55]. Despite all these efforts, our ability to forecast the consequences of severe space weather events is still very limited [123]. Finally, *Bland et al.* [2018] and Berngardt et al. [18] have demonstrated the utility of the Super Dual Auroral Radar Network (SuperDARN) for understanding HF absorption during SEPs and solar flares.

A solar storm that occurred during 4–10 September 2017 produced severe space weather anomalies including numerous flares, energetic protons, and CMEs directed towards the

Earth. The impacts included R_3 category radio blackouts, PCAs, and a G_4 category geomagnetic storm [123]. In addition, this solar storm produced multiple flare events in which M and X–class flares occurred in quick succession. The ionospheric responses were distinctly different from that expected from isolated flares. We have therefore classified these as a separate category, referred to as "compound flares". This is in contrast with the well–defined ionospheric response due to a typical solar flare occurring in isolation, known as an "isolated flare". Our previous study [27] examined the characteristics of several isolated X–class flare–driven SWFs. This follow–up work presents a comparative analysis of the ionospheric response to an isolated flare and a compound flare. In addition, we examine the latitudinal impact of the three space weather drivers, namely solar flares, SEPs, and auroral activity.

3.2 Datasets & Methodology

The Super Dual Auroral Radar Network (SuperDARN) is an international network of HF radars, operating between 8–18 MHz [33, 57, 112] and located at middle, high and polar latitudes. Traditional SuperDARN data products include line–of–sight (LoS) velocity, spectral width and power of the backscattered signal from the electron density irregularities (ionospheric scatter), from the Earth's surface (ground/sea scatter), and from meteor plasma trails at $\approx$ 90 km altitude. However, a few recent studies have demonstrated the utility of SuperDARN sky noise level to characterize ionospheric disturbances during various space weather phenomena [18, 20]. The primary datasets used in this study are the sky noise measurements and the occurrence of daytime ground–scatter echoes from SuperDARN radars across the North American sector as shown in Figure 3.1. The SuperDARN sky noise measurements are used to derive the HF absorption using the concept of riometry [85] and characterization of a quiet day curve (QDC) is a crucial step in the process.

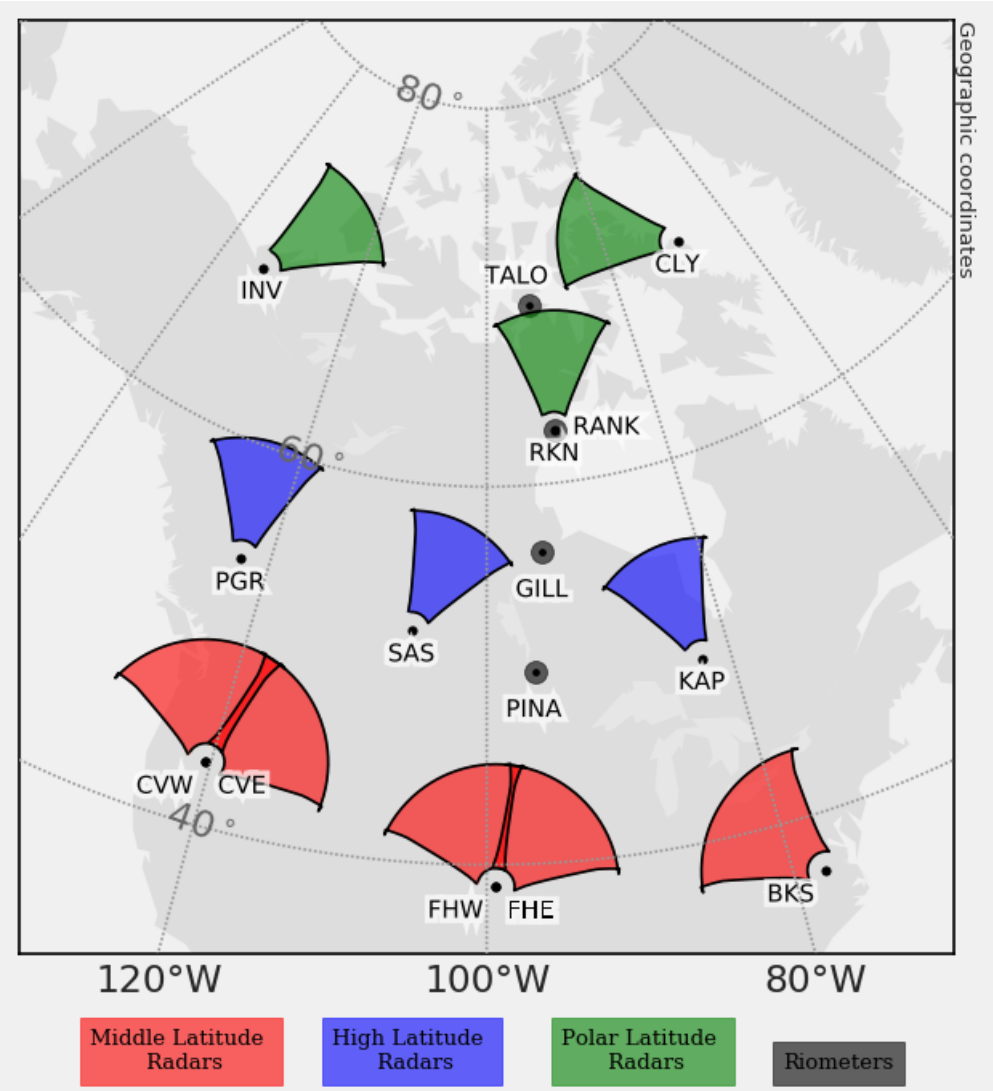

Figure 3.1: Fields–of–view (FoV) of SuperDARN radars and riometers used in this study.

We derived a QDC of sky noise for each radar using data for quiet days from the previous month (August, 2017). Specifically, we used data from intervals having no solar flares, no SEPs and AE less than 100 nT. SuperDARN sky noise measurements have strong dependences on range separation and operating frequency [20]. Hence, we adopted the methodology described in Bland et al. [20] to segregate these influences on the variations of sky noise level. We binned the measurements based on these parameters and separate QDCs were derived for individual radars and each frequency band. Finally, we estimated the HF absorption by

taking the ratio of the instantaneous sky noise measurement to the QDC level, which is a standard procedure in riometry [21, 132]. This method provides a physically reliable estimation of HF absorption with very few (less than 4%) data points having negative values. In addition, we also used riometer cosmic noise absorption (CNA) data from the Pinwa, Gillam, Rankin Inlet and Taloyoak stations as shown in Figure 3.1. The HF absorption due to three overlapped space weather drivers might not be a linear superposition of their individual impacts. We therefore used a non–parametric Kendall's rank correlation (Kendall, 1938) analysis to segregate the three driving influences.

We used the GOES X–ray and proton flux data along with geomagnetic indices, namely, AE [71], K_p [13] and D_{st} [23] to describe the solar and geomagnetic conditions. Furthermore, crowd–sourced amateur radio data (only 80 m band) from an electronic amateur radio monitoring network (WSPRNet) was used to describe the impacts of different space weather phenomena on HF communication links. WSPRNet reports the time stamp, frequency of operation, signal–to–noise ratio (SNR), and call signs of the transmitting (TX) and receiving (RX) stations in a record known as a "spot". The count of these link records, known as number of spot (#–Spot), can be used to describe the ionospheric HF propagation conditions.

The solar flares are classified as isolated or compound based on the shape of the solar X–ray spectrum and their signatures in the SuperDARN radar observation. While isolated flares were characterized by a single sharp peak in the X–ray spectrum, compound flares consisted of numerous sharp peaks with small time separations. Specifically, the time separations of successive solar flares was much less than the expected duration of the effect of an individual solar flare in the ionosphere. We used the method described in Chakraborty et al. [27] to estimate the duration of SWF from ground–scatter echoes and aggregated all the flares occurring within that time as one compound flare.

A typical SuperDARN radar response to a solar flare has three distinct phases, namely,

onset, radio blackout and recovery. We defined the onset and the start of radio blackout of an event as the instants when the depletion in ground–scatter echo count reaches to at least 10% and 80% of the background values, respectively. The start and end of the recovery phase correspond to ground–scatter echo counts of at least 15% and 95% of the background values, respectively. Chakraborty et al. [27] also proposed a linear model to describe the duration of SWF as a function of solar zenith angle (SZA), X–ray peak flux, and operating frequency. In this study, we compare the observed and predicted durations of SWF obtained using the methodology and the model described in our previous paper for the cases of isolated and compound flares.

3.3 Observations

In this section, we examine the difference in SuperDARN response to isolated versus compound flares and to co–occurring space weather events between 4 and 10 September 2017. Specifically, we analyze the impact of this severe solar storm using the number of ground–scatter echoes and the drop in sky noise level observed by SuperDARN.

During the first week of September 2017, the Sun produced multiple flares, energetic protons, and CMEs projected towards the Earth, which drove several space weather phenomena. Figure 3.2 presents the solar and geomagnetic conditions during this extended period of extreme solar activity. The top three panels provide information about three major driving influences for HF absorption, namely, solar X–ray flux, solar energetic proton flux, and the auroral electrojet index AE. The colored shadings indicate dominant drivers based on the upper three panels: yellow for solar proton events ($\geq$ 10 MeV proton excited 10 particle flux unit), green for auroral activity (AE $\geq$ 500 nT), and red and blue regions for compound and isolated solar flares ($\geq$ M1–class) respectively. Next, panels (d) & (e) present information

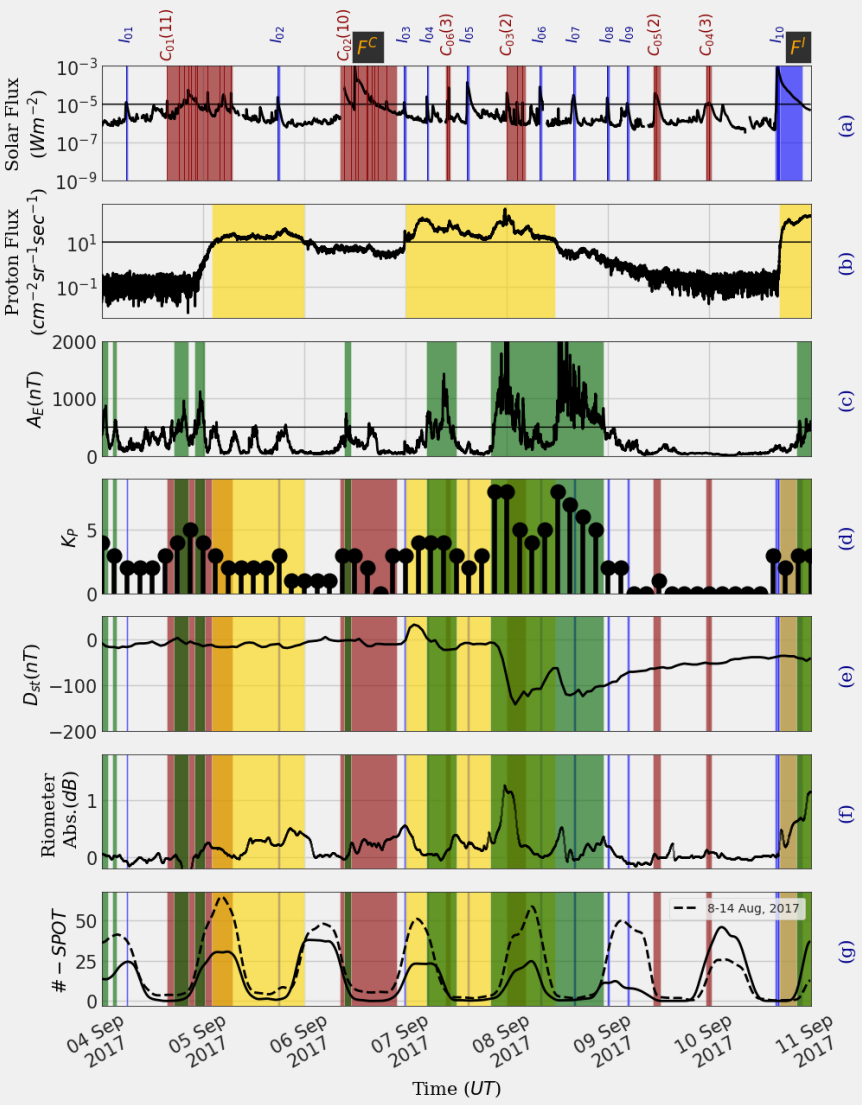

Figure 3.2: Geomagnetic conditions during 4–10 September, 2017: (a) GOES–15 solar X–ray flux at 0.1–0.8 nm wavelength band, (b) GOES–15 proton flux ($\geq$ 10 MeV), (c) AE , (d) K_P, (e) D_{st} indices, (f) averaged CNA data from the riometers mentioned in Figure 3.1 and (g) average number of spots (records from WSPRNet 80 m band) for the current event (solid line) as well as for the period between 8–14 August 2017 (dashed line). Blue and red vertical lines in panel (a) show isolated (I_*) and compound ($C_*(\#)$) flare events respectively. Horizontal black lines passing through panels (a), (b) and (c) represent M–class flare, SEP event ($\geq$ 10 MeV proton data reaches 10 pfu) and AE = 500 nT thresholds respectively. Shaded regions indicate different geomagnetic phenomena. Yellow: Solar proton event, Green: Auroral activity (precipitation) due to geomagnetic storm, Red: Compound solar flare, and Blue: Isolated solar flare.

about geomagnetic storm intensity indicated by K_p and D_{st} respectively. Finally, panels (f) and (g) present the average riometer CNA data from Pinawa, Gillam, Rankin Inlet and Taloyoak stations and the WSPRNet spot counts in solid black lines. For reference, the spot count for 8–14 August 2017 is also overlaid in panel (g), showing spot counts during the previous Carrington cycle. Isolated and compound flares are labeled as I_* and $C_*(\#)$, where * and # indicate flare number and the number of individual flares during one compound flare, respectively. It is evident that multiple overlapped space weather events were occurring throughout this period. For example, three strong SEP events were observed during 5–8 September and on 10 September. Additionally, a severe (G_5) geomagnetic storm was observed during 8–9 September, and the whole period was dominated by five major X–class and many M–class solar flares ($\approx$ 40 in total). Finally, the spot count comparison between the two curves indicate that HF propagation was significantly impacted during this period (during 4–10 September 2017) due to the numerous space weather phenomena.

3.3.1 Mid and High Latitude Ionospheric Response to Solar Flares

We now investigate the mid and high latitude SuperDARN radar response to solar flares. Specifically, we analyze the differences in SuperDARN responses due to isolated and compound flares, labeled as (F^I) and (F^C) in Figure 3.2, respectively. The isolated flare (F^I) struck North America during early afternoon and so most of the SuperDARN radars under consideration were impacted by it. However, during the compound flare (F^C) event most of the mid and high latitude SuperDARN radars were in the dawn and night sectors except the Blackstone and Kapuskasing radars and so only these two radars captured all the signatures of the compound flares.

Figure 3.3 compares observations from SuperDARN radars and the Pinawa riometer during

the isolated and compound solar flare period labeled as (F^I) and (F^C), respectively in Figure 3.2. Panels (a), (b) and (c) present flare signatures from the GOES X–ray sensor, the number of ground–scatter echoes from the Blackstone radar, and Blackstone HF absorption data. Panels (d) and (e) show corresponding observations from the Kapuskasing radar. The gray shaded regions in panels (b) and (d) indicate the expected duration of flare impact calculated using the linear model described in Section 3.2. Finally, panel (f) presents Pinawa riometer cosmic noise absorption (CNA) data. The panels on the left and right of panel (f) present the impact of the isolated flare (F^I) and compound flare (F^C), respectively.

As shown by Figure 3.3, the isolated flare (F^I) completely suppresses the ground–scatter echoes and sky noise measurement for almost 2 and 4 hours for the Blackstone and Kapuskasing radars, respectively. In contrast, the impact of the compound event (F^C) is more gradual. Successive small flares suppress the ground–scatter echoes for longer than predicted by the Chakraborty et al. [27] method for isolated flares and lengthen the overall blackout and recovery phases. For example, multiple small depressions in average number of ground–scatter echoes shown in panels (b.2), (d.2) and enhancements in CNA in panel (f.2) represent the impact of individual flares following the initial X9.3 flare. By comparing panels (b.1) and (d.1) with (b.2) and (d.2) we can conclude that the expected duration of the isolated flare matches the observations whereas the duration of the response for flares during the compound event are underestimated. Two important features can be observed in panels (b.2) and (d.2). First, the impacts of individual flares (gray shading) inside a compound flare are not continuous (see overlapping and gaps in gray shading) and, secondly, linear superposition of individual SWF durations does not add up to the total observed duration. This disagreement suggests that the ionospheric response to multiple flares in quick succession is not merely the linear superposition of individual isolated flare effects.

Solar flare–driven SWF is a dayside phenomenon and most impactful near the subsolar point.

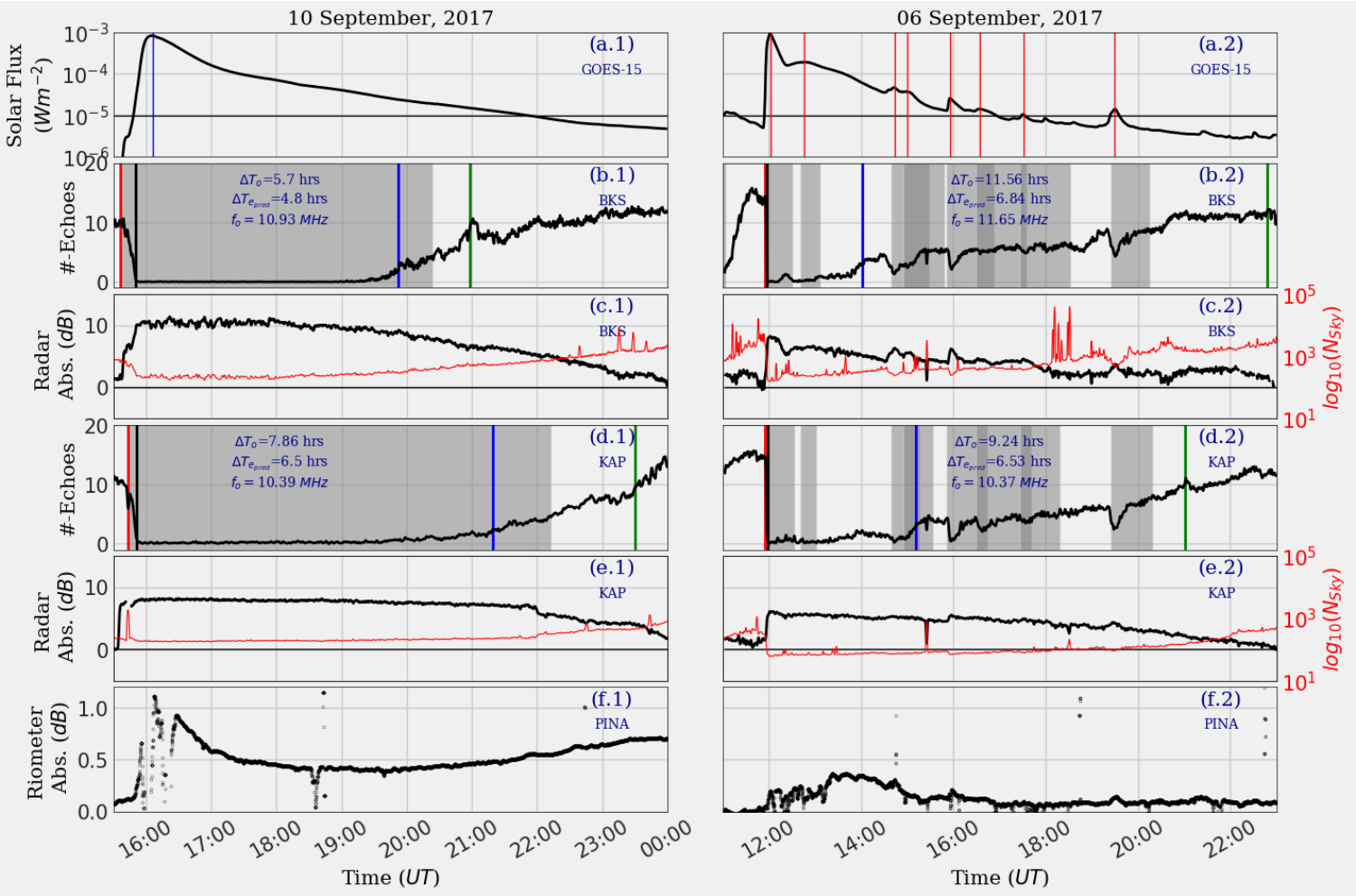

Figure 3.3: Blackstone, Kapuskasing radar and Pinawa riometer observations in response to an isolated flare (I_{10}) on 10 September and a compound ($C_{02}(10)$) flare on 6 September (right). From top to bottom: (a) GOES–15 solar X–ray flux data (0.1–0.8 nm wavelength band), (b) number of ground–scatter echoes, (c) attenuation in sky noise from Blackstone radar, (d) number of ground–scatter echoes, (e) attenuation in sky noise from Kapuskasing radar and (f) riometer absorption from Pinawa station. Blue and red vertical lines in panel (a) indicate individual flares. Vertical lines in panels (b) and (d) represent onset (red), blackout start (black), recovery start (blue) and recovery end (green) time of SWF. Shaded regions in panel (b) and (d) show the expected duration of the SWF based on the methodology of Chakraborty et al. [27] (see text for details). Red curves passing through the panels (c) and (e) represents sky noise measurement in log scale.

During the compound flare F^C most of the SuperDARN radars across the North American sector were in the dawn and night sectors. We therefore analyzed the SuperDARN radar and

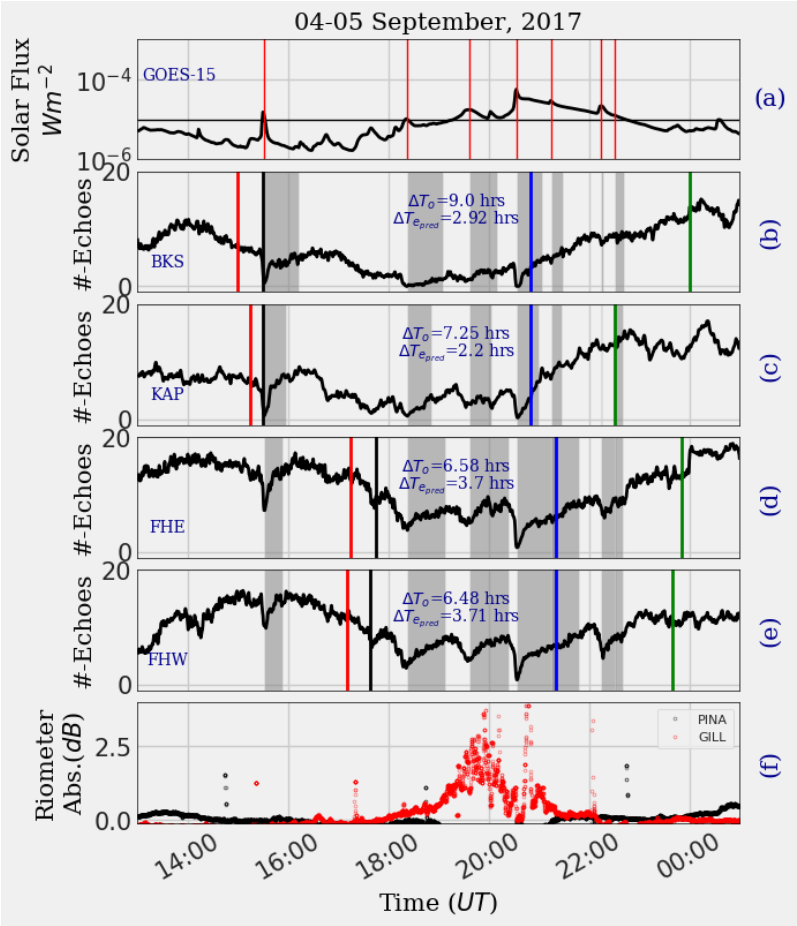

Figure 3.4: Stack plot showing SuperDARN HF radar and riometer observations in response to a compound ($C_{01}(11)$) flare during 4–5 September. From top to bottom: (a) GOES–15 solar X–ray flux data (0.1–0.8 nm wavelength band), number of ground–scatter echoes from (b) Blackstone, (c) Kapuskasing, (d) Fort Hays East, (e) Fort Hays West, and (e) riometer absorption from Pinawa and Gillam stations. Red vertical lines in panel (a) indicate individual flares. Vertical lines in panels (b)-(e) represent onset (red), blackout start (black), recovery start (blue) and recovery end (green) time of SWF. Shaded regions in panel (b)-(e) show the expected duration of the SWF based on the methodology of Chakraborty et al. [27] (see text for details).

riometer responses during a second compound flare event labeled $C_{01}(11)$ in Figure 3.4, to confirm the observational features demonstrated in Figure 3.3. Panels (a), (b), (c), (d) and (e) of Figure 3.4 present the flare signature from the GOES X–ray sensor, and the number of ground–scatter echoes from the Blackstone, Kapuskasing, Fort Hays East and West radars,

respectively. Finally, panel (f) shows CNA data from the Pinawa and Gillam riometers. Note that the compound flare event $C_{01}(11)$ does not include an X–class flare and therefore SuperDARN ground–scatter echoes were not completely suppressed. However, the successive small flare impacts delay the overall recovery of the event and this leads to a mismatch in observed and predicted response times, which is consistent with the compound flare features presented in Figure 3.3. Panel (f) shows only one sudden enhancement (corresponding to the largest flare) in the Gillam riometer data in response to flare $C_{01}(11)$. Riometers operate at the high end of the HF spectrum (30 MHz) and so are less sensitive to M–class flare signatures than the HF radars operating on 10–18 MHz. The mismatch between the observed and predicted response times in SuperDARN observations, as shown in panels (b)-(d) of Figure 3.4, confirms that the observational features of a compound flare are reproducible and consistent with the evidence presented in Figure 3.3.

3.3.2 Correlation Analysis of Co–occurring Space Weather Events and Radio Absorption

In this subsection, we investigate the latitudinal impact of the three co–occurring space weather phenomena on ionospheric HF absorption using Kendall–tau correlation analysis. We also quantify the local time (longitudinal) influence on three features of SWF, namely, the durations of the onset, radio blackout and recovery phases. Note that the September 2017 solar storm produced two geomagnetic storms and three SEP events but 40 solar flare events; hence we restrict our investigation to the local time influence on SWF only.

Figure 3.5 presents an example of Kendall-tau correlation analysis for 4 September, 2017. We used a 24–hour correlation window to quantify the dependencies between the three space weather driving sources and ionospheric HF absorption observed by the three latitudinal

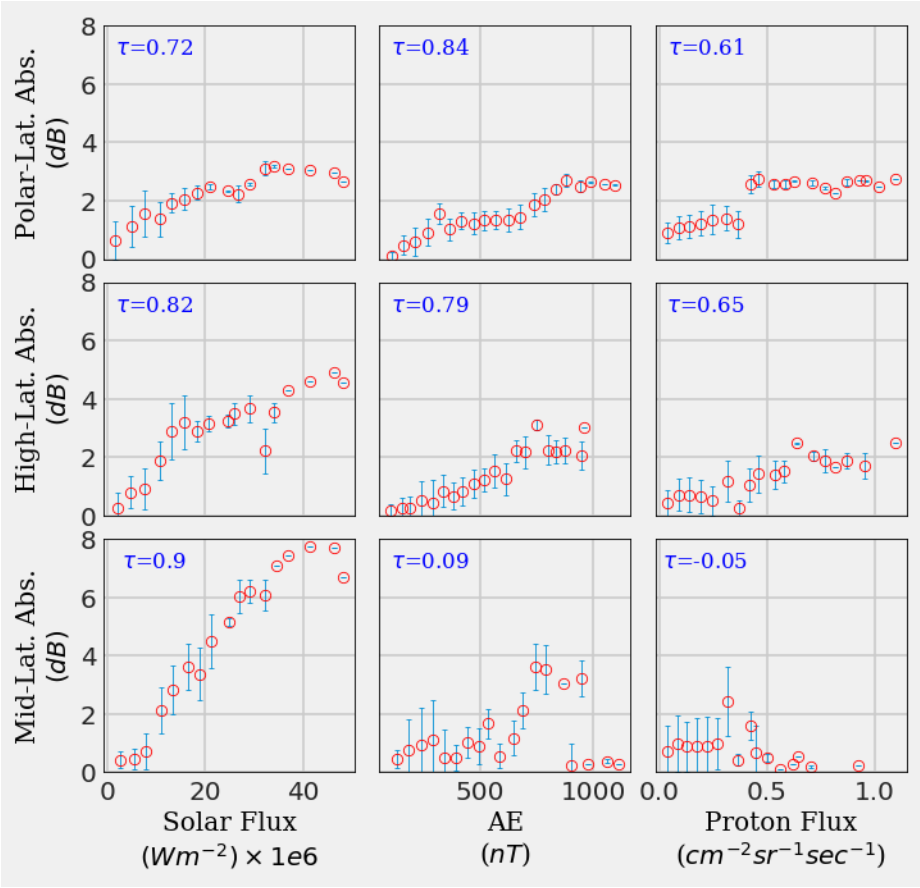

Figure 3.5: Scatter plots of polar (top row), high (middle row) and mid (bottom row) latitude ionospheric HF absorption versus solar flux (left column), AE (middle column) and proton flux (right column) for 4 September, 2017. Associated correlation coefficients are provided inside each panel.

radar chains. Kendall-tau correlation coefficients between median HF absorption for the three latitudinal radar chains and the three types of space weather driving, namely, GOES solar flux, AE, and GOES proton flux, are provided inside the panels of Figure 3.5. While solar flare impact typically lasts about 100 minutes [27], the impacts from SEPs and geomagnetic storms last a few hours to several days. We therefore used three minute median–filtered data for this statistical analysis, which should be able to capture any variations in derived HF absorption due to relatively short–lived solar flare or longer lasting SEP and geomagnetic storm events. To verify the robustness of the result we also analyzed the data with a

12–hour window and found the correlation coefficients obtained using the two different windows are different, but the overall conclusions regarding the dominant driving mechanism for each latitude chain are unchanged. From the figure, it is evident that solar flux–driven HF absorption has a severe impact at mid latitudes but not at higher latitudes. In contrast, AE and proton flux are the major drivers of HF absorption at high and polar latitudes and have negligible contribution to mid latitude absorption.

To further investigate the latitudinal impact of the three co–occurring space weather drivers on ionospheric HF absorption we adapted the methodology described in the previous paragraph to all 7 days of data from 4 September to 10 September 2017. Figure 3.6 presents Kendall–tau correlation analysis between radar derived HF absorption from three different latitudinal ranges and the three driving influences, namely, SWF, PCA and auroral absorption. The top three panels show the driving while the bottom three panels show the radar derived HF absorption from mid, high and polar latitude SuperDARN radars, respectively. Horizontal black lines passing through the panels represent M–class flares, SEP events (proton count $\geq$ 10 pfu) and auroral activity (AE = 500 nT), respectively. The Kendall–tau correlation coefficients between median absorption (orange line) and GOES X–ray flux, GOES proton flux and the auroral electrojet (AE) index are calculated for a window of 24 hours and are denoted by τ_{Φ}, τ_{P} and τ_{ae} respectively. It should be noted that the radars are distributed across longitudes so this analysis will not necessarily capture the diurnal variations. Each day of the bottom three panels is color–coded by the rank correlation coefficients, indicated by the color chart on the right. These color shadings identify the dominant driver(s) of HF absorption. For example, purple color in panel (d) indicates that both solar flux and auroral activity were dominant drivers of mid latitude HF absorption on 7 September.

It can be clearly observed from Figure 3.6 that HF absorption at mid latitudes is predominantly driven by solar flux while at polar latitudes it is more closely associated with proton

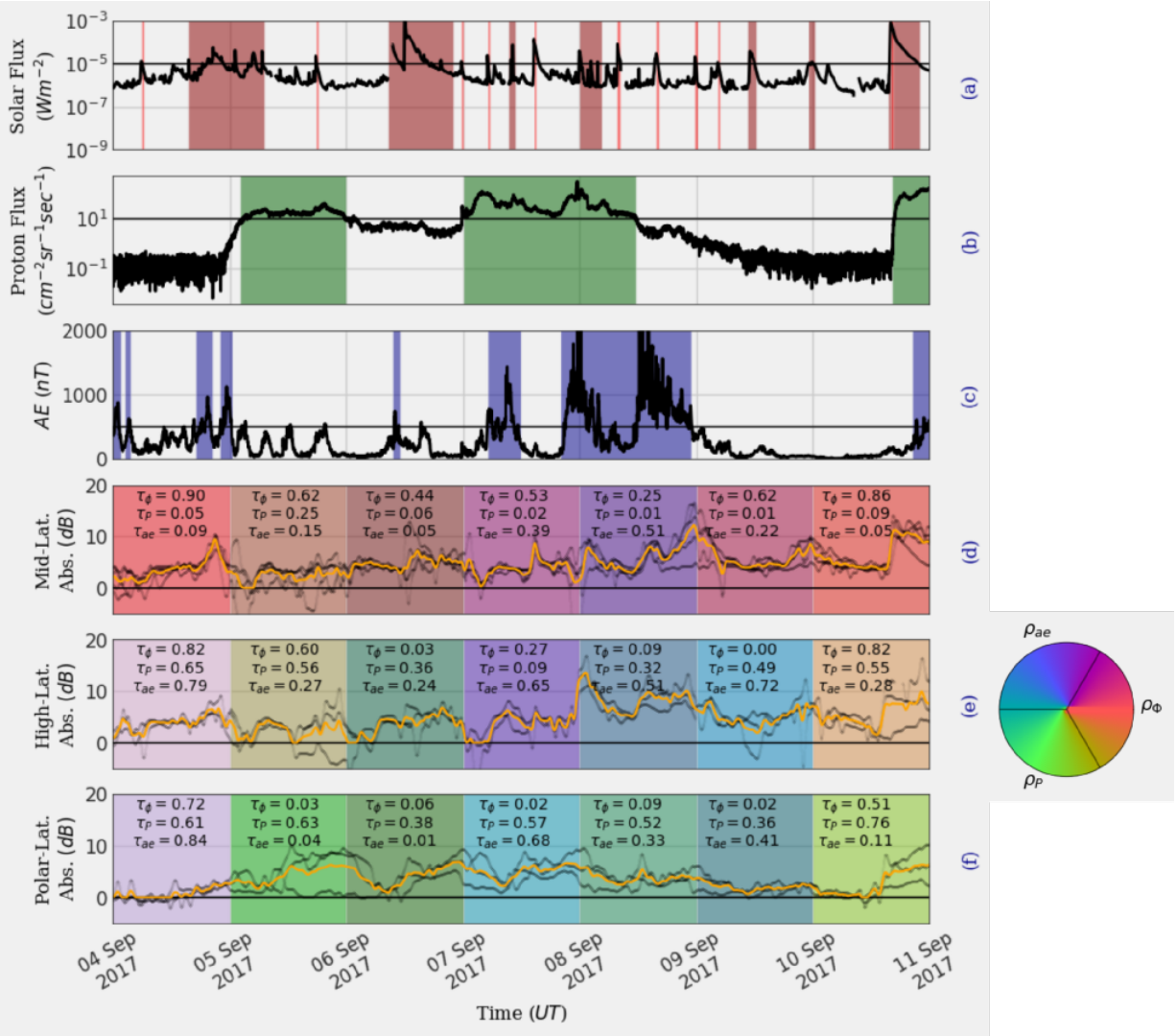

Figure 3.6: Correlation study showing latitudinal extents of different types of ionospheric absorption in SuperDARN radars during the event: (a) GOES–15 solar X–ray flux at 0.1–0.8 nm wavelength band (in red), (b) GOES–15 proton flux ($\geq$ 10 MeV) data (in green), (c) AE indices (in blue), (d), (e) and (f) absorption data from middle, high and polar latitude radars respectively. Horizontal black lines passing through panels (a), (b) and (c) represent M–class flare, SEP event and AE = 500 nT respectively. Color shades in panels (a), (b), (c) represent period where the threshold was exceeded. Orange lines passing through panels (d), (e) and (f) are maximum value of absorption (smoothed over a window). Daily correlation coefficients derived using the method described before and each day is color shaded according to the color chart mentioned right.

flux. However, high latitude (i.e. auroral) radar absorption is influenced by both solar flux and proton flux. Fields–of–View (FoV) of the high latitude radars cover a large latitudinal range ($\approx 45^{o}$–65^{o} geographic latitudes) and are therefore susceptible to both flare–driven SWF and SEP–driven PCA. Additionally, during the start and end of the week, solar flares and SEPs were the major drivers of HF absorption, whereas, during the middle of the week auroral activity (i.e. AE) was the primary driver of HF absorption observed by SuperDARN across all three latitudes. In summary, the statistical rank-correlation study displayed in Figure 3.6 demonstrates that solar X–ray and proton flux are the major drivers of mid and polar latitude HF absorption, respectively, but high latitude HF absorption is influenced by both of these drivers. However, during the geomagnetic storm auroral activity becomes the dominant driver across all three latitudes.

Last, we examine the influence of local time (LT) on solar flare–driven HF absorption observed by SuperDARN radars. The signature of SWF seen in SuperDARN ground–scatter echoes can be categorized into three phases, namely, onset, blackout and recovery [27]. In this study, we statistically quantify the LT influence on these three phases of SWF using the 10 isolated M–class solar flare events identified as I_* in Figure 3.2. Figure 3.7 presents the local time dependence of duration of onset, blackout and recovery phases from top to bottom, respectively. The black curve passing through each panel shows a cosine fit to the data. The goodness–of–fit reduced–χ^2 coefficients are also provided inside each panel. The reduced–χ^2 coefficient for the onset duration fitting suggests that the brief onset duration has a weak local time dependence. In contrast, the blackout and recovery phases are highly influenced by local time and both maximize at local solar noon. Note that the average duration of onset, blackout and recovery phases of these isolated M–class flare events are 10 seconds, 12 minutes and 10 minutes, respectively.

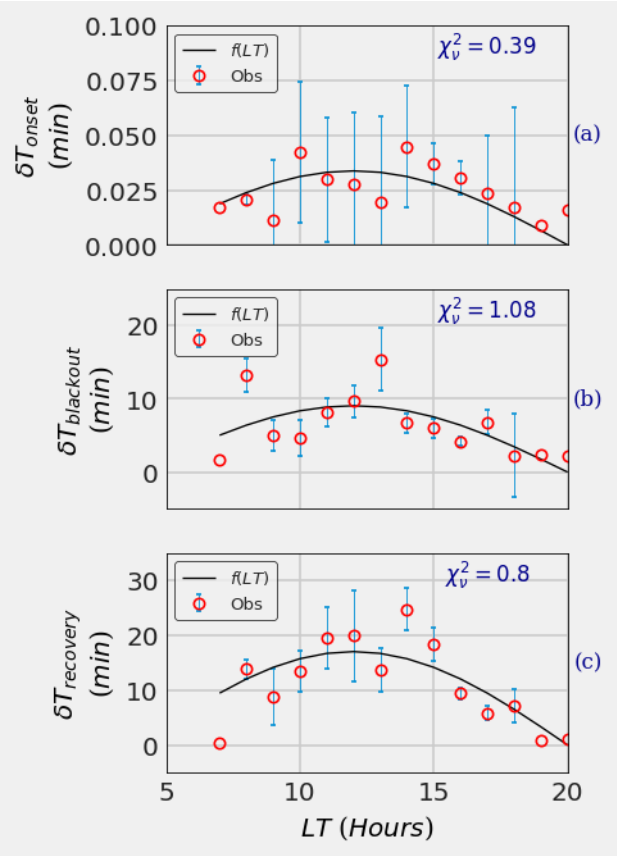

Figure 3.7: Local time dependence of: (a) duration of onset time, (b) duration of radio blackout time and (c) duration of recovery time. The black line passing through each panel shows a cosine fit to the data and associated goodness–of–fit reduced–χ^2 coefficients are provided inside each panel.

3.4 Discussion

In the previous section, we showed that the solar storm between 4 and 10 September 2017 had a significant impact on SuperDARN observations at all latitudes. Specifically, we compared the SuperDARN response during isolated versus compound flares, and examined the influence of the co-occurring space weather events on HF absorption at different latitudes. In addition, we quantified the LT influence on different features of flare–driven SWF. In this section, we further analyze the significance of the observations and compare them with previous studies.

We begin with a comparison of mid and high latitude ionospheric radiowave absorption in SuperDARN radar responses during an isolated flare and flares happening in quick succession. Figures 3 and 4 showed disruption in the number of ground–scatter echoes and enhancement of radar–derived HF absorption during isolated and compound solar flare events. Several prior studies focused on analyzing the impacts of isolated events [27, 78] but to our knowledge none have explicitly examined the effects of multiple flares happening in quick succession. Previously, we found that isolated X–class flares induce SWF lasting about 100 minutes [27]. However, the analysis here shows that the typical duration of a compound X–class flare–driven SWF event can be much longer ($\geq$4–5 hours). One explanation for this extended ionospheric relaxation time is that it is an artifact of the slow recovery of D–region electron temperature after a large perturbation as suggested by Bajčetić et al. [12]. Specifically, large increases in temperature can change D–region recombination rates, which induce a relatively longer relaxation time. Rodger et al. [129] showed that the functional form of lower ionospheric relaxation time in response to transient ionization following a solar flare is semi–logarithmic if there are no external excitations within the system during the period of relaxation. While this assumption is valid for an isolated flare, the scenario would be different for a compound flare. During the compound flare the ionosphere is being excited by solar flares in quick succession before completely recovering from the previous flare effects. Hence, these findings suggest that the impact of a compound flare cannot merely be reproduced with a linear superposition of individual flare influences.

The statistical analysis presented in Figures 5 and 6 reveals that the SuperDARN radar response during overlapped space weather events has a strong dependence on latitude. Abdu et al. [2] showed that a rapid recovery in the storm–time auroral activity in conjunction with an X–class flare could cause a delay in the response of the equatorial electrojet (EEJ) to that flare, suggesting storm–driven ionospheric effects are more severe than flare–driven

transients. Specifically, the study found the solar flare–induced enhanced E–region ionization alters the effective westward and overshielding electric fields and thus producing a delay in the EEJ response. These findings are consistent with the SuperDARN observations presented in this study. During the middle of the week, the storm–driven expanded auroral oval likely enhanced the D–region impact ionization at high and middle latitudes to such an extent that it dominated over the ionospheric HF absorption effects due to other sources, such as solar flares. These findings suggest that the latitudinal variability in the ionospheric background conditions influence the impacts of overlapped space weather events.

Another focal point of our study is the analysis of the LT effects on three features of SWF, namely, the onset, radio blackout and recovery phases. Tsurutani et al. [154] showed that photoionization decreases at regions away from the subsolar point due to the increase in the thickness of the atmosphere and the grazing angle of incidence. Specifically, they showed SWF is a dayside phenomenon, PCA affects the entire polar ionosphere, and auroral absorption affects the dayside or night side depending upon the upstream solar wind parameters and penetration electric field. In this study, we showed the relatively longer phases of SWF (i.e. blackout and recovery) exhibit severe impacts near local noon with a cosine LT– dependence while the relatively short–lived onset phase has a weaker dependence on LT. This is consistent with our previous study [27], in which we found a weak dependence of the relatively short–lived onset phase on SZA. Together, the results suggest the dispersion in arrival time of solar flux across different local time sectors is negligible. Finally, the study by Tsurutani et al. [154] emphasized the necessity of using multiple sources of data to decouple the effects of these individual phenomena. Further progress will likely require global observations and numerical modeling to fully decouple the overlapped effects of the individual space weather drivers.

3.5 Conclusions

An extreme solar storm on 4–10 September 2017 produced numerous solar flares, radiation storms, and a coronal mass ejection, which produced a drop in the number of ground–scatter echoes observed by SuperDARN radars. In this paper we have examined the nonlinear response of the ionosphere during successive solar flare events occurring in quick succession and segregated the influences of three different kinds of radiowave absorption, namely, shortwave fadeout, polar–cap absorption, and auroral absorption in SuperDARN observations. We found that successive solar flares extend the ionospheric relaxation time and one possible explanation for this is the enhancement in D–region electron temperature. Statistical analysis showed a combination of different drivers (i.e. solar flares, solar energetic particles and auroral precipitation) can influence HF absorption at any given latitudinal range and it is difficult to segregate their effects just based on SuperDARN observations. Further analysis combining global observations with numerical simulations is required to develop an improved understanding of the impacts of co–occurring space weather drivers on HF radiowave absorption. We believe the accuracy of such models could be validated and improved by carrying out such a study.

Acknowledgments

We thank the National Science Foundation for support under grant AGS–1341918. We wish to acknowledge the use of the NOAA/GOES X–ray and energetic proton data (from https://satdat.ngdc.noaa.gov/sem/goes/data/) for flare and SEP event confirmation and analysis. The D_{st} and AE indexes was obtained from the Kyoto World Data Center for Geomagnetism (http://wdc.kugi.kyoto-u.ac.jp/). The K_p index was accessed through the GFZ–Potsdam website. We thank all participants in the worldwide SuperDARN collaboration for the distribution of SuperDARN data via http://vt.superdarn.org/tiki-index.php?

page=Data+Access. The riometer CNA data was obtained from University of Calgary website (http://data.phys.ucalgary.ca/). We also thankful to the amateur radio community and provided the HF radio spot data used in this paper. Spot data was provided by the Weak Signal Propagation Reporting Network (WSPRNet, http://wsprnet.org/drupal/). The majority of analysis and visualization was completed with the help of free, open–source software tools such as matplotlib [68], IPython [118], pandas [97], Skifield python API, and others (e.g.,Millman and Aivazis [102]).

Chapter 4

Ionospheric Sluggishness: A Characteristic Time-Lag of the Ionospheric Response to Solar Flares

S. Chakraborty[1], J. M. Ruohoniemi[1], J. B. H. Baker[1], R. A. D. Fiori[2], S. M. Bailey[1], and K. A. Zawdie[3]

[1]Bradley Department of Electrical and Computer Engineering, Virginia Tech, Blacksburg, Virginia, USA

[2]Geomagnetic Laboratory, Natural Resources Canada, Ottawa, Ontario, Canada

[3]Space Science Division, US Naval Research Laboratory, Washington DC, USA

Chakraborty, Ruohoniemi, J. M., Baker, J. B. H., Fiori, R. A. D., Bailey, S. M., & Zawdie, K. A. (2021). Ionospheric Sluggishness: A Characteristic Time-Lag of the Ionospheric Response to Solar Flares. JGR Space Physics, Under Review.

Abstract

The term "sluggishness" was coined by E. V. Appleton in the 1950s to describe the time delay between peak irradiance at solar noon and the resulting peak in ionospheric electron density. Sluggishness can be understood as an inertial property of the ionosphere that manifests as a lag of the ionospheric response to a solar driver. As shown by Appleton, estimates of sluggishness can be used to study the chemistry of the lower ionosphere, of the D-region in particular. In this study, for the first time, we have examined ionospheric sluggishness in terms of the time delay between the peak irradiance during a solar flare and the resulting peak in ionospheric electron density using HF instruments. Estimates of the delay are obtained using HF observations from riometers and SuperDARN radars that are primarily sensitive to absorption in the D-region. Two new methods for measuring delay are introduced. Sluggishness is shown to be anti-correlated with peak solar X-ray flux and positively correlated with zenith angle and latitude. The choices of instrument, method, and reference solar waveband affect the sluggishness estimation. A simulation study was performed to estimate the effective recombination coefficient in the D-region. The coefficient was found to vary by orders of magnitude with peak flare intensity. We argue that the variation in effective recombination coefficient with peak flare intensity is highly sensitive to changes in the negative and positive ion chemistry of the D-region, which is sensitive to the incoming solar X-ray and EUV radiation.

Plain Language Summary

A systematic time delay between peak incoming solar radiation during a solar flare and peak electron density in the ionosphere is known as ionospheric sluggishness. Ionospheric sluggishness is known to be maximized around D-region heights (∼60-90 km altitude). This article is our first attempt to estimate ionospheric sluggishness using high frequency (3 - 30 MHz) instruments. In addition, we statistically characterize the observed sluggishness and provide

an insight into D-region photochemical processes. In this article, we also demonstrate how to extract the D-region's recombination coefficient using a theoretical model and measured sluggishness.

4.1 Introduction

Solar EUV and X-ray radiation are primary sources for producing the ionosphere. The ionospheric response to a sudden intense solar X-ray burst, or solar flare, has been studied since the early 1900s [40]. Flare-driven high frequency (HF: 3 - 30 MHz) absorption, also known as shortwave-fadeout (SWF), is a well-understood phenomenon [e.g. 47, 103]. However, the initial time delay of the ionospheric response following a solar flare, also known as "sluggishness", is not yet fully understood [113]. E. V. Appleton first defined the term sluggishness as the time delay between the peak in electron-ion production at local solar noon and the peak in ionospheric electron density [9]. We now understand sluggishness as an inertial property of the ionosphere that is dependent on latitude, longitude, and height of the ionosphere, as described in equation 4.1 [9].

$$\delta = \delta(\theta, \phi, h) = T_{n_e^{\max}} - T_{q^{\max}} \tag{4.1}$$

where: θ, ϕ, h, $T_{n_e^{\max}}$, and $T_{q^{\max}}$ are the latitude, longitude, altitude, time of peak electron density, and time of peak electron-ion production rate, respectively. Appleton found that δ is inversely proportional to the electron density. Appleton and his contemporaries tried to measure and characterize sluggishness in terms of the time delay between peak solar irradiance ($I_\infty^{\max}$) and peak radiowave absorption (β) in the ionosphere [9, 44], as described

in equation 4.2:

$$\bar{\delta} = \bar{\delta}(\theta, \phi) = T_{\beta^{\max}} - T_{I_\infty^{\max}} \tag{4.2}$$

where: $T_{\beta^{\max}}$ and $T_{I_\infty^{\max}}$ are the times of peak HF absorption and peak solar irradiance, respectively. Sluggishness has thus been discussed in terms of the time delay between the peaks in an ionospheric driver and a related ionospheric parameter. The underlying inertial property of the ionosphere can be gauged in other ways, for example, in terms of the time delay between the peaks in the rates of change of driver and parameter. This is particularly helpful for measurement techniques that experience a saturation effect with respect to the parameter measured. Recent studies have shown that some HF instruments indeed undergo a saturation effect (a flat peak in the observation, see section 3.1 for details) due to the suppression of signals caused by the absorption that follows an X-class solar flare on the dayside of the Earth [27, 28]. Hence, the standard definition by equation (2) is not applicable. We propose two alternative definitions of sluggishness. First, we define it as the time difference between the peak in the time derivative of β and the peak in the time derivative of I_∞ as described in equation 4.3:

$$\bar{\delta}_{\mathrm{s}} = \bar{\delta}_{\mathrm{s}}(\theta, \phi) = T_{\dot{\beta}} - T_{\dot{I}_\infty} \tag{4.3}$$

where: $T_{\dot{\beta}}$ and $T_{\dot{I}_\infty}$ are the times of peak time derivative in absorption and peak time derivative in solar irradiance, respectively. Second, we define the time shift (τ) in I_∞ that maximizes the correlation (ρ) between β and I_∞, as described in equation 4.4:

$$\bar{\delta}_{\mathrm{c}} = \bar{\delta}_{\mathrm{c}}(\theta, \phi) = \max_{\tau} \rho[\beta(t), I_\infty(t + \tau)] \tag{4.4}$$

We point out that ionospheric sluggishness has a microscopic nature and depends on spatial

coordinates, in particular, on height. However, it is impractical to extract and characterize the ionospheric sluggishness at each point using remote sounders. Note that $\bar{\delta}$, $\bar{\delta}_s$, and $\bar{\delta}_c$ represent time delays between a change in solar irradiance and an ionospheric response, whereas δ represents the time delay between peak photoionization rate and peak ionospheric electron density. Specifically, $\bar{\delta}$ represents the time delay between the peak in the HF absorption and peak solar irradiance of the event, whereas $\bar{\delta}_s$ represents the time delay when both solar irradiance and ionospheric response are changing most rapidly (during the peak of time derivative) and $\bar{\delta}_c$ represents the time delay that maximizes the similarities between variations in solar irradiance and ionospheric response. All three sluggishness estimates, ($\bar{\delta}$, $\bar{\delta}_s$, and $\bar{\delta}_c$) from riometer and SuperDARN measurements represent cumulative sluggishness along the ray path. For example, $\bar{\delta}$, $\bar{\delta}_s$, and $\bar{\delta}_c$ from riometers represent height integrated sluggishness, considering riometers have narrow vertical fields-of-view. In contrast, the same estimations from SuperDARN radars represent cumulative sluggishness along the ray path, considering that the radars have oblique fields-of-view (refer to Section 2 for SuperDARN fields-of-view). Although the three different time delays defined in equations (2)-(4) have different reference times, measurement, and estimation techniques, all of them are indicative of the inertial property of the ionosphere and thus inherit the properties of δ described by Appleton (see equation (1)).Our definitions in terms of peak time derivatives and correlation have some advantages for characterizing the response of the ionosphere to impulsive events such as flares measured using instruments such as riometers and SuperDARN HF radars.

Figure 1(a-c) present examples of the estimation of ionospheric sluggishness $\bar{\delta}$, $\bar{\delta}_s$, and $\bar{\delta}_c$ using the conventional, peak time derivative, and correlation methods, respectively. The data were obtained with the Ottawa riometer data during a solar flare event on 11 March 2015. The red curve and black dots in all three panels indicate solar soft X-ray (0.1-0.8 nm) irradiance from a GOES satellite and cosmic noise absorption (CNA) from the Ottawa riometer, respectively.

The solid and dashed vertical lines in panel (a) and (b) indicate peaks and maximum time derivative in X-ray irradiance (red) and CNA data (black), respectively. The difference in the solid [dashed] vertical lines in panel (a) [(b)] represents the estimated conventional [time derivative] sluggishness. The red dashed curve in panel (c) shows the time-shifted solar soft X-ray (0.1-0.8 nm) irradiance. The correlation coefficient and estimated sluggishness are shown in the panel. The estimated sluggishness values from the three different methods are $\bar{\delta}$= 46s, $\bar{\delta}_s$= 139s, and $\bar{\delta}_c$= 80s, for this event, respectively.

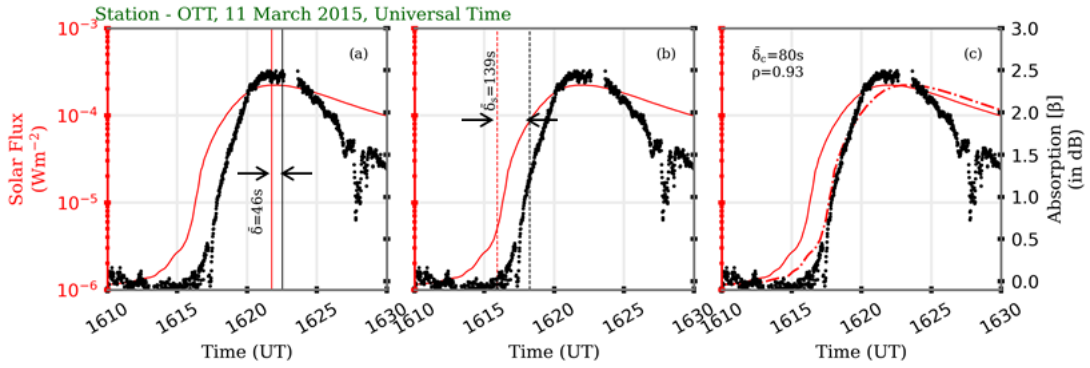

Figure 4.1: Ionospheric sluggishness in Ottawa (OTT) riometer measurement during a solar flare event on 11 March 2015, estimated using (a) conventional, (b) peak time derivative, and (c) correlation methods. Red and black colors represent SXR irradiance from GOES and CNA observations from the riometer, respectively. The solid and dashed vertical lines in panels (a) and (b) represent peaks and peak time derivative in both datasets, respectively. The dashed red curve in panel (c) represents time delayed GOES SXR irradiance data. Sluggishness values estimated using the three different methods are provided inside each panel

Since Appleton first described sluggishness, experimental studies have used very low frequency (VLF, 3-30 kHz) receivers to understand its variations with solar zenith angle (χ), and peak solar irradiance $I_\infty^{\max}$ [44, 113]. The sluggishness recorded using VLF instruments is defined as the time difference between the peak in VLF amplitude ($A^{\max}$) and $I_\infty^{\max}$, as described in equation 4.5:

$$\delta^{VLF} = T_{A^{\max}} - T_{I_\infty^{\max}} \tag{4.5}$$

It will be apparent this measurement also represents a cumulative effect due to the propagation of VLF signal along an extended path. VLF Studies have reported a typical value of sluggishness (δ^{VLF}) of 3 - 10 minutes [14, 113]. These studies reported wide variability in sluggishness values during M and C class flares but did not try to explain the chemical processes that manifest the sluggishness.

Sluggishness measurements are useful because they provide information about the ionospheric electron density and the effective recombination coefficient (α_{eff}). Appleton [9] determined that δ is inversely proportional microscopic recombination coefficient $\alpha(\theta, \phi, h)$. Owing to the variety of recombination processes, it is more appropriate to refer to an effective recombination coefficient, α_{eff}. The α_{eff} is controlled by the atmospheric negative ions (e.g. O^-, O_2^-, NO_3^-, CO_3^-, HNO_3^- etc and their hydrates) and positive ions (e.g. $H^+(H_2O)_n$) [113, 124, 155]. Specifically, α_{eff} defines the effective loss rate of electrons due to cascading photochemical reactions following electron production due to photoionization [117]. Sluggishness measurements, however obtained, can provide insight into D-region and mesospheric photochemistry and can also be used to validate models.

Here we report on the first study to compare the basic characteristics of sluggishness using both passive and active high frequency instruments, namely, riometers and SuperDARN HF radars, respectively. We present a statistical characterization of ionospheric sluggishness following solar flares, measured using different instruments and the parameters defined by equations (2-4), and report on variations of the sluggishness estimates with χ, $I_\infty^{\max}$, local time (LT), and latitude (ϕ). We describe how different ionospheric sounding techniques and choice of reference solar wavebands impact the measured sluggishness. Through a theoretical modeling study and using measured $\bar{\delta}$ from riometer data, we show how α_{eff} varies with peak solar soft X-ray flux. Specifically, the simulation study describes how negative ions chemistry influences the sluggishness. Finally, we discuss how our results inform the physics of

sluggishness and its variability, and our understanding of D-region photochemical processes.

4.2 Instrumentation & Datasets

In this study, we used GOES-15 X-ray sensor data for the solar X-ray irradiance information during solar flares and ionospheric absorption in the HF bands from ground-based riometers and SuperDARN HF radars, respectively [20]. Solar X-ray flux information was obtained from the solar X-ray sensor of the National Oceanic and Atmospheric Administration's (NOAA) GOES 15 satellite [93]. This instrument has two channels, namely hard (0.05-0.4 nm) and soft (0.1-0.8 nm), to detect variations in solar flux in these two wavebands. We primarily used soft X-ray (SXR) flux for our analysis; however, hard X-ray (HXR) information is also used for comparison.

A riometer is a ground-based passive radio receiver which provides information about ionospheric HF absorption by measuring variations in cosmic radio noise at 30 MHz frequency [e.g. 22, 46]. The CNA values used in this study are taken from a network of riometers distributed across Canada operated partially by Natural Resources Canada (NRCan) and partially by the University of Calgary (Geospace Observatory riometer, or GO-RIO) [80, 133].

SuperDARN is a global network of HF radars, operating between 8 and 18 MHz, located across the middle, high and polar latitudes of both hemispheres. Each radar observes the line-of-sight (LoS) component of plasma velocity along 16 to 20 beams in 75-110 range gates spaced 45 km apart beginning at 180 km range [33, 57, 112]. Typically, each beam sounding has a 3s or 6s integration period, resulting in a full radar sweep through all beams in 1 or 2 minutes. SuperDARN observations primarily consist of two types of backscatter, namely, ionospheric scatter and ground scatter. In the case of ground scatter, due to the high daytime vertical gradient in the refractive index, the rays bend toward the ground and are reflected

from surface roughness and return to the radar following the same paths. Ionospheric scatter is due to the reflection of the transmitted signal from ionospheric plasma irregularities. However, in this study, we will only use the ground scatter observations. Specifically, we use the "inverse ground scatter count" during a particular period, determined as the drop in ground scatter echo counts during an event (i.e., maximum count – actual count) to estimate the ionospheric sluggishness observed by the HF radars [27].

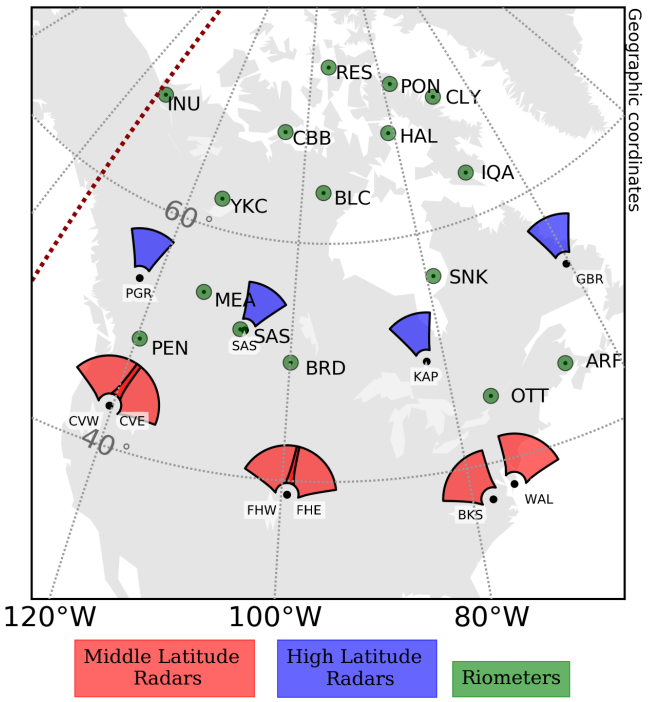

Figure 4.2: Location of the various instruments used in the study. The red line at -135.3^o longitude indicates the longitudinal location of the GOES 15 satellite. Colors represent the fields-of-view of the middle (red) and high (blue) latitude SuperDARN radars and riometers (green).

Figure 2 presents the location of the instruments used in this study. Radar fields-of-view of SuperDARN radars located in middle and high latitudes across the North American sectors are colored in red and blue, respectively. The fields-of-view indicated by the shading represents the first seven range gates (1-7) of the radars, where the radar signal transits the D-region of the ionosphere and SuperDARN radar is most sensitive to solar flare-driven HF

absorption. The green circles centered around the black dots represent the riometers used in this study. These filled circles denoting riometer station locations indicate the 100-km diameter region around each riometer station where absorption is detected. Tables 1 and 2 provide station name, code, geographic, and geomagnetic coordinates for all the riometers and SuperDARN radars used in this study, respectively.

Riometer Station	**Station Code**	**Geographic**	**Geomagnetic**
Alert	ALE	$(82.52^o, -62.27^o)$	$(87.09^o, 79.31^o)$
Resolute Bay	RES	$(74.7^o, -94.9^o)$	$(82.52^o, -33.93^o)$
Pond Inlet	PON	$(72.68^o, -77.95^o)$	$(80.80^o, 2.30^o)$
Clyde River	CLY	$(70.48^o, -68.51^o)$	$(78.06^o, 17.67^o)$
Cambridge Bay	CBB	$(69.1^o, -105.0^o)$	$(76.70^o, -46.45^o)$
Hall Beach	HAL	$(68.77^o, -81.25^o)$	$(77.45^o, -4.76^o)$
Inuvik	INU	$(68.3^o, -133.5^o)$	$(71.49^o, -82.03^o)$
Baker Lake	BLU	$(64.3^o, -96.0^o)$	$(73.21^o, -29.46^o)$
Iqaluit	IQA	$(63.7^o, -68.5^o)$	$(71.82^o, 14.62^o)$
Yellowknife	YKC	$(62.5^o, -114.5^o)$	$(69.35^o, -55.90^o)$
Sanikiluaq	SNK	$(56.3^o, -79.0^o)$	$(65.93^o, -2.03^o)$
Meanook	MEA	$(54.6^o, -113.3^o)$	$(62.10^o, -51.36^o)$
Saskatoon	SAS	$(52.2^o, -107.12^o)$	$(60.80^o, -42.74^o)$
Brandon	BRD	$(49.92^o, -99.95^o)$	$(59.56^o, -32.61^o)$
Penticton	PEN	$(49.32^o, -119.63^o)$	$(55.90^o, -57.52^o)$
St John's	STJ	$(47.6^o, -52.7^o)$	$(53.18^o, 31.08^o)$
Acadia	ARF	$(46.0^o, -66.0^o)$	$(54.55^o, 15.08^o)$
Ottawa	OTT	$(45.4^o, -75.5^o)$	$(55.44^o, 2.30^o)$

Table 4.1: List of Riometers used for statistical study.

4.3 Results

In this section, we characterize ionospheric sluggishness measured from riometer and SuperDARN observations, using the equations defined in Section 1, and describe a technique to estimate α_{eff} from the sluggishness measured by the riometer. Specifically, we present one classic example of ionospheric sluggishness in SuperDARN observations extracted using the

Radar station	Station Code	Geographic	Geomagnetic
Wallops Island	WAL	$(37.93^o, -75.47^o)$	$(48.47^o, 1.77^o)$
Blackstone	BKS	$(37.10^o$, -77.95$^o)$	$(47.97^o, -1.67^o)$
Fort Hays East	FHE	$(38.86^o$, -99.39$^o)$	$(49.16^o, -30.75^o)$
Fort Hays West	FHW	$(38.86^o$, -99.39$^o)$	$(49.16^o, -30.75^o)$
Christmas Valley East	CVE	$(43.27^o$, -120.36$^o)$	$(49.94^o, -56.80^o)$
Christmas Valley West	CVW	$(43.27^o$, -120.36$^o)$	$(49.94^o, -56.80^o)$
Goose Bay	GBR	$(53.32^o$, -60.46$^o)$	$(60.64^o, 23.01^o)$
Kapuskasing	KAP	$(49.39^o$, -82.32$^o)$	$(59.69^o, -7.20^o)$
Saskatoon	SAS	$(52.16^o$, -106.53$^o)$	$(60.85^o, -41.95^o)$
Prince George	PGR	$(53.98^o$, -122.59$^o)$	$(59.81^o, -62.33^o)$

Table 4.2: List of Radars used for statistical study.

peak time derivative and correlation methods proposed in Section 1. Next, we statistically characterize $\bar{\delta}$, $\bar{\delta}_s$, and $\bar{\delta}_c$ measured in the riometer and SuperDARN observations and describe their dependence on *chi*, ϕ, LT, and $I_\infty^{\max}$. Then, we discuss the typical practice of using solar SXR as a reference to measure sluggishness and compare it with the measurement considering solar HXR as a reference. Finally, we describe a theoretical method to estimate α_{eff} from the sluggishness measured by the riometer ($\bar{\delta}$), validate it with the theoretical values and get an insight into the D-region chemistry. Note, unlike the other two sluggishness parameters defined by equations (3) and (4), only $\bar{\delta}$ can be used to estimate α_{eff}.

We have introduced two new methods for estimating sluggishness from HF observations with equations (3) and (4), both of which are going to be used for statistical characterization along with the conventional method described in equation (2). Appleton described sluggishness as the time delay between the peak of solar flux and the peak in HF absorption described by equation (2). Recent studies have shown that HF radar undergoes complete radio blackouts during solar flares, which produces a saturation effect in the observations [27, 28]. This necessitates alternative definitions that can be used to estimate sluggishness from HF systems. The proposed definitions in equation (3) and (4) estimate sluggishness as the time difference

between the moments when effects are changing most rapidly rather than when the effects reach their peaks. One advantage of this approach is that the moments of most rapid rise are usually better defined than the moments of peak values.

4.3.1 SuperDARN Event Study: 11 March 2015

As an example, consider an X2.1 solar x-ray flare that erupted on 11 March 2015, peaking at 16:22 UT. Fiori et al. [47] used this event to demonstrate the potential of SuperDARN for monitoring the space weather impact due to solar X-ray flares using widespread observations of the event across Canada and the Northern United States.

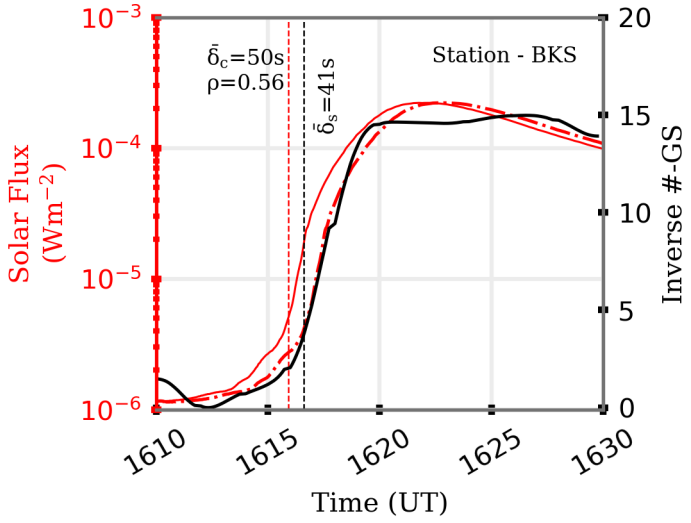

Figure 4.3: Ionospheric sluggishness in SuperDARN Blackstone radar ground scatter measurements estimated using peak time derivative and correlation methods during a solar flare event on 11 March 2015. Red and black colors represent SXR irradiance from GOES, and inverse ground scatter echoes from Blackstone SuperDARN radar, respectively. The solid and dashed red curves represent actual and time-delayed SXR irradiance, respectively. The dashed vertical lines represent peak time derivatives in both the datasets. Sluggishness values estimated using peak time derivative, correlation methods, and correlation coefficient are provided in the panel.

Figure 3 presents a time series of inverse ground scatter count data from the SuperDARN

Blackstone radar (black) in response to the sudden increase in solar SXR due to the solar flare (red) on 11 March 2015. The dashed red curve represents time delayed SXR data. The difference in timing of the peaks in the time derivatives, indicated by the red and black vertical dotted lines, represents the sluggishness associated with the peak time derivative method, which is $\bar{\delta}_{\mathrm{s}} = 38$s. The sluggishness estimated using correlation analysis is $\bar{\delta}_{\mathrm{c}} = 50$s. Both sluggishness values are significantly lower than the values obtained from the riometer measurements using peak time derivative and correlation method, $\bar{\delta}_{\mathrm{s}} = 139$s and $\bar{\delta}_{\mathrm{c}} = 80$s, respectively (see Figure 1(b-c)). This significant difference in the sluggishness measured by the two instruments is most likely due to the difference in their corresponding sounding techniques.

4.3.2 Correlation Analysis

To characterize the statistical behavior of $\bar{\delta}^{\mathrm{rio}}$ and $\bar{\delta}_{\mathrm{s}}^{\mathrm{rio}}$ estimated from riometer and $\bar{\delta}_{\mathrm{s}}^{\mathrm{SD}}$ and $\bar{\delta}_{\mathrm{c}}^{\mathrm{SD}}$ estimated from SuperDARN observations, we analyzed 92 C, 63 M, and 18 X class flares events between 2006 and 2017. Note that these solar flare events were selected from GOES XRS reports maintained by NOAA when the NRCan, GO-RIO riometers, and SuperDARN radars were online, to ensure the largest possible data set, and predominantly located on the dayside such that several riometers and radars observed absorption enhancements in association with the enhanced solar X-ray flux. To characterize $\bar{\delta}^{\mathrm{rio}}$ and $\bar{\delta}_{\mathrm{s}}^{\mathrm{rio}}$, we selected events showing an absorption peak of at least 0.5 dB and at least 0.2 dB greater than the minimum absorption during the flare interval and detectable positive slope (> 0.3) in the rising phase of the event, respectively. To analyze $\bar{\delta}_{\mathrm{c}}^{\mathrm{SD}}$ and $\bar{\delta}_{\mathrm{s}}^{\mathrm{SD}}$, we selected events showing more than 50% depletion in ground scatter counts and detectable positive slope (> 0.3) in the rising phase of the event, respectively. These differing event selection criteria for the four different sluggishness estimation techniques lead to varying numbers of events for correlation

analysis. On average, each solar flare event affects 4-5 riometers and 3-4 SuperDARN radars located on the dayside of the Earth. This collectively produces 640 and 250 individual riometer absorption events to characterize $\bar{\delta}^{\mathrm{rio}}$ and $\bar{\delta}_{\mathrm{s}}^{\mathrm{rio}}$ and 355 and 190 individual radar events to characterize $\bar{\delta}_{\mathrm{s}}^{\mathrm{SD}}$ and $\bar{\delta}_{\mathrm{c}}^{\mathrm{SD}}$, respectively.

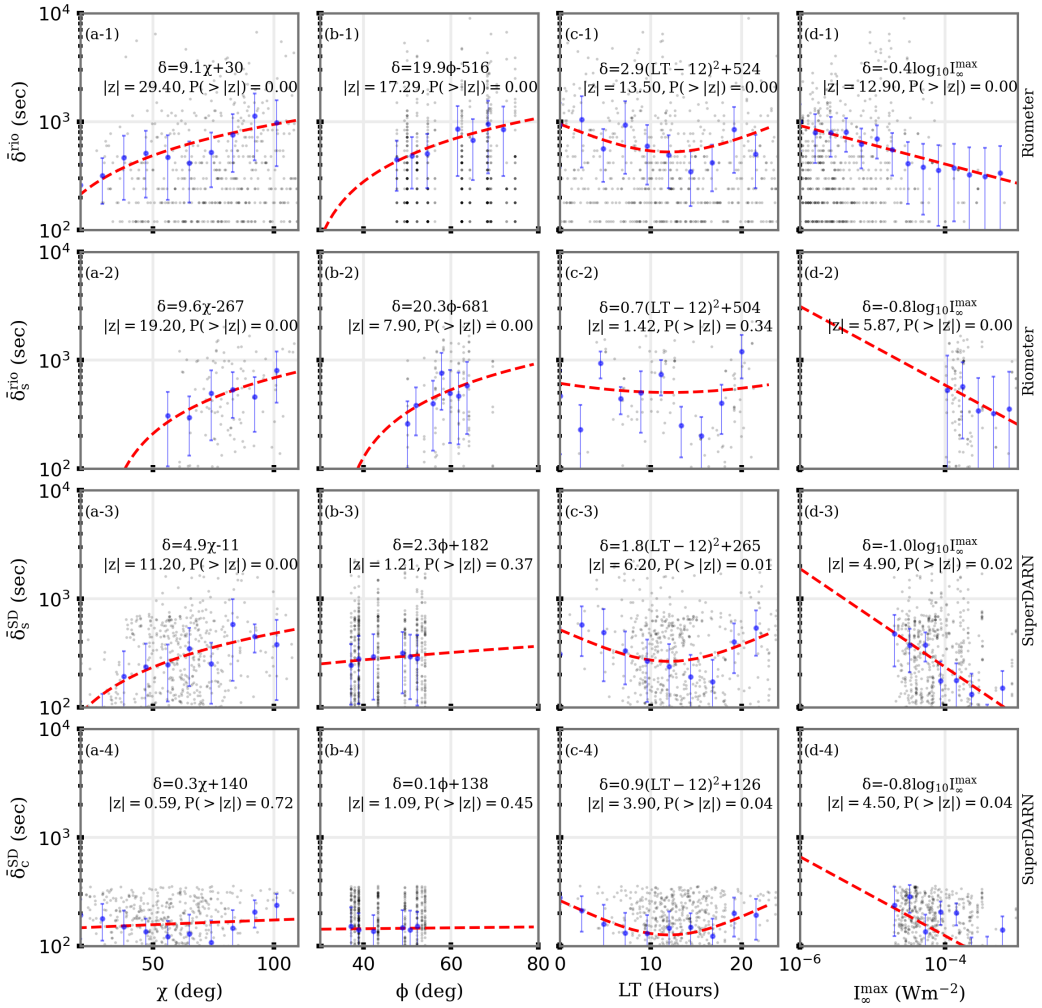

Figure 4.4: Correlation analysis between sluggishness estimated using equations (2-4) ($\bar{\delta}$, $\bar{\delta}_{\mathrm{s}}$, $\bar{\delta}_{\mathrm{c}}$) from riometer and SuperDARN observations with (a-1∼4) solar zenith angle (χ), (b-1∼4) latitude (ϕ), (c-1∼4) local time (LT), and (d-1∼4) peak flux ($I_{\infty}^{\max}$), respectively. The black dots represent estimated sluggishness for riometers and SuperDARN using equations (2-4). The blue dots with blue error bars represent binned median values with median absolute deviation, and the red curve in each panel represents the best-fitted curve through the binned median values. The associated fitting equations with coefficients, Z-test statistics, and P-values of the coefficients are provided in each panel.

Figure 4 presents a correlation analysis of the $\bar{\delta}^{\text{rio}}$, $\bar{\delta}_{\text{s}}^{\text{rio}}$o, $\bar{\delta}_{\text{s}}^{\text{SD}}$, and $\bar{\delta}_{\text{c}}^{\text{SD}}$ observed by riometers and SuperDARN radars with χ, ϕ, local time (LT), and $I_{\infty}{}^{\max}$ (panels a-d). A separate analysis is presented for $\bar{\delta}^{\text{rio}}$, $\bar{\delta}_{\text{s}}^{\text{rio}}$, $\bar{\delta}_{\text{s}}^{\text{SD}}$, and $\bar{\delta}_{\text{c}}^{\text{SD}}$ in each row from top to bottom, respectively. The black and blue dots represent estimated and binned median sluggishness values, respectively. The blue error bars associated with the binned median values represent the median absolute deviation (MAD), and the red dashed curve passing through each panel shows the best-fitted curve. We have assumed a linear dependence between sluggishness measurements and solar zenith angle, latitude, and logarithm of peak solar flux. The choice of linear analysis is motivated by previous studies [e.g. 113]. While the exact mathematical form of these dependencies is most likely non-linear, the linear regression analysis is used here primarily to show the presence positive/negative trend of measured sluggishness. Finally, the functional form of the fitted curve and the significant statistics (Z-score and p-value) of the coefficient are provided in each panel. A combination of high Z-score and low p-value ($\leq$0.05) indicates a dependence on the parameter with high confidence.

The correlation analysis shows that all four sluggishness estimates vary linearly with χ, ϕ and $\log_{10} I_{\infty}^{\max}$; while having a quadratic relation with LT. We found, $\bar{\delta}^{\text{rio}}$ has a strong dependence on all four parameters under consideration. In addition, $\bar{\delta}_{\text{s}}^{\text{rio}}$ shows a weak dependence on LT. Furthermore, the analysis reveals $\bar{\delta}_{\text{s}}^{\text{SD}}$ has a strong dependence on χ, LT, and $I_{\infty}^{\max}$. Note that, $\bar{\delta}_{\text{c}}^{\text{SD}}$ and $\bar{\delta}_{\text{s}}^{\text{SD}}$ show weak dependencies on latitude, while $\bar{\delta}^{\text{rio}}$ and $\bar{\delta}_{\text{s}}^{\text{rio}}$ have strong dependencies. We think the reason behind this discrepancy in riometer and SuperDARN measured sluggishness is the expansive fields-of-view of SuperDARN radars. Namely, the radar measurement integrates the effects from multiple encounters with the ionosphere over a propagation path that is extended in both latitude and longitude, which reduces sensitivity to latitudinal variations. We found $\bar{\delta}_{\text{c}}^{\text{SD}}$ shows a strong dependence on LT and $I_{\infty}^{\max}$. Determination of strong, weak, and no-dependence is made on the basis of

the values of regression coefficient, associated Z-score, and estimated p-value. A regression coefficient with a high Z-score ($\geq$4) and a low p-value ($\leq$0.05) is classified as high dependence. In comparison, regression coefficient with a marginal Z-score ($\sim$4) and p-value ($\sim$0.05) is classified as weak dependence. Finally, regression coefficient with a low Z-score ($<$4) and high p-value ($\geq$0.05) is considered as no dependence. The analysis shows the typical ranges of $\bar{\delta}^{\text{rio}}$, $\bar{\delta}^{\text{rio}}$, $\bar{\delta}_{\text{s}}^{\text{SD}}$, and $\bar{\delta}_{\text{c}}^{\text{SD}}$, which are 150 - 4000s, 90 - 2500s, 90 - 1400s, and 60 - 700s, respectively. Note that, all these values encompass the reported range of δ^{VLF}, which is typically 5 - 10 minutes [63, 113]. All four sluggishness estimates show minima at local noon (12 LT). Features observed in the correlation analysis can be described by our current understanding of the sluggishness [9]; sluggishness decreases in response to an increase in electron density and α_{eff}. The drops in sluggishness values with decreasing χ, increasing $I_{\infty}^{\max}$, and nearness to local noon are most likely due to enhancement in electron density. The enhancements in sluggishness estimates with ϕ may be due to two effects, namely, a decrease in electron density and a latitude-dependent change in ionospheric chemistry.

Figure 5, along with Table 3, presents pairwise difference statistics to show comparisons between the four types of sluggishness estimated using equations (2-4) and riometer and SuperDARN radar observations. Specifically, the figure shows the cumulative distributions of sluggishness estimated using four different methods. The table presents the Kolmogorov–Smirnov test (KS test) statistic [1, 146] and associated p-values for each pairwise comparison. KS test, a nonparametric test, is used to check the equality of two continuous, one-dimensional probability distributions. The KS test quantifies the distance between two empirical distribution functions. If the KS estimated distance is significant with a p-value $\leq$0.05, then we suggest that the two distributions are different from each other. In this case, we find that $\bar{\delta}^{\text{rio}}$, $\bar{\delta}_{\text{s}}^{\text{rio}}$, $\bar{\delta}_{\text{s}}^{\text{SD}}$, and $\bar{\delta}_{\text{c}}^{\text{SD}}$ are statistically different distributions.

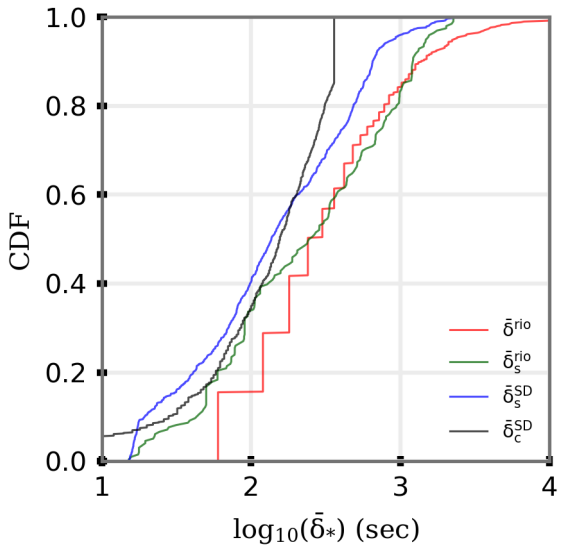

Figure 4.5: Cumulative distribution functions of different estimations of sluggishness from riometer and SuperDARN measurements. In the figure, $\bar{\delta}^{\text{rio}}$, $\bar{\delta}^{\text{rio}}_{\text{s}}$, $\bar{\delta}^{\text{SD}}_{\text{s}}$ and $\bar{\delta}^{\text{SD}}_{\text{c}}$ represent sluggishness measured using riometers with equation (2), riometers with equation (3), SuperDARN with equation (3), and SuperDARN with equation (4), respectively.

KS-Stat	$\bar{\delta}^{\text{rio}}$	$\bar{\delta}^{\text{rio}}_{\text{s}}$	$\bar{\delta}^{\text{SD}}_{\text{s}}$	$\bar{\delta}^{\text{SD}}_{\text{c}}$
$\bar{\delta}^{\text{rio}}$	$\kappa_{\text{s}} = 0, p = 1$	-	-	-
$\bar{\delta}^{\text{rio}}_{\text{s}}$	$\kappa_{\text{s}} = 0.24, p = 3 \times 10^{-8}$	$\kappa_{\text{s}} = 0, p = 1$	-	-
$\bar{\delta}^{\text{SD}}_{\text{s}}$	$\kappa_{\text{s}} = 0, p = 7.7 \times 10^{-31}$	$\kappa_{\text{s}} = 0.4, p = 10^{-23}$	$\kappa_{\text{s}} = 0, p = 1$	-
$\bar{\delta}^{\text{SD}}_{\text{c}}$	$\kappa_{\text{s}} = 0.38, p = 0.0$	$\kappa_{\text{s}} = 0.28, p = 1.3 \times 10^{-28}$	$\kappa_{\text{s}} = 0.38, p = 10^{-16}$	$\kappa_{\text{s}} = 0, p = 1$

Table 4.3: KS test statistics showing a relative comparison between two datasets. KS Stats >0.1 and P-value <0.05 represents two statistically different distributions.

4.3.3 Hard X-ray Waveband as Reference

Ever since Appleton first developed the theory of ionospheric sluggishness most of the observational VLF studies have considered the peak of solar SRX irradiance as the reference time for estimating sluggishness [44, 79, 113], under the assumption that solar SRX irradiance is the best proxy for photoionization. However, photoionization at different altitudes is regulated by solar irradiance wavebands, which peak at different times during a solar flare [67]. Consequently, the reference time should vary with ionospheric heights, which creates ambi-

guity when estimating sluggishness from height integrated ionospheric response considering SXR data as the only reference.

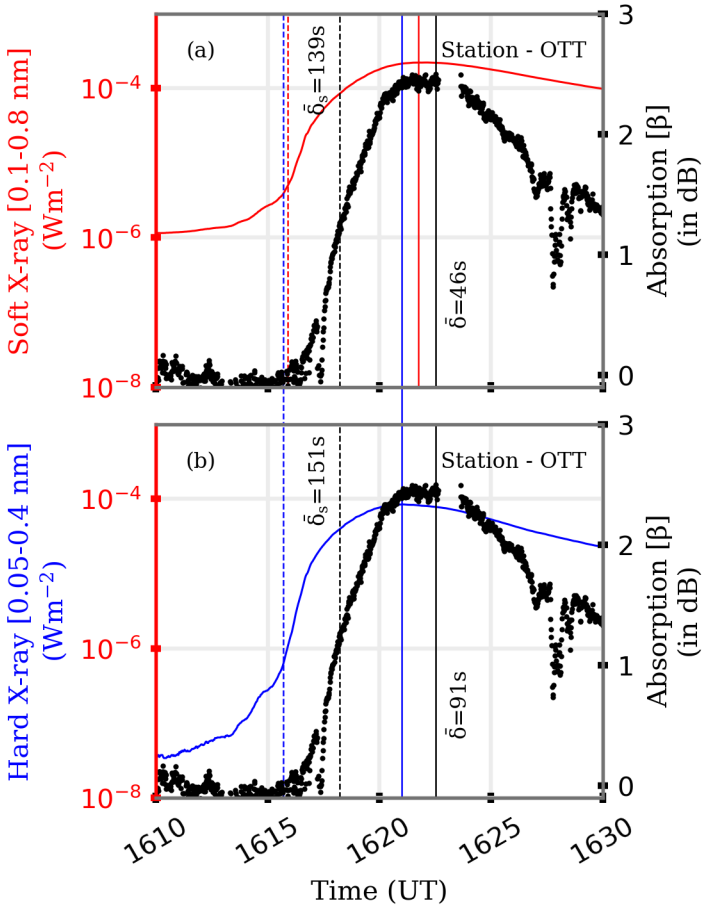

Figure 4.6: Sluggishness in Ottawa riometer measurement during a solar flare event on 11 March 2015, considering (a) SXR irradiance and (b) HXR irradiance observations as reference. Red, blue, and black colors represent SXR, HXR irradiance from GOES, and CNA observations from the riometer, respectively. The solid (dashed) red and black lines represent the peak times (peak time derivatives) in GOES SRX irradiance and riometer cosmic noise absorption, respectively. Sluggishness estimated using conventional and peak time derivative methods are mentioned in panels.

Figure 6 presents one example of the issue described in the previous paragraph. Panels (a) and (b) present sluggishness estimated using conventional and peak time derivative methods from Ottawa riometer measurements during a solar flare event on 11 March 2015, considering

SXR irradiance (in red) and HXR irradiance (in blue) as a reference. Black dots represent observations from the Ottawa riometer. The estimated sluggishness using conventional and peak time derivative methods considering SXR irradiance as the reference is $\bar{\delta} = 46$s and $\bar{\delta}_{\mathrm{s}} = 139$s, respectively. In contrast, using HRX irradiance as a reference the corresponding estimates for sluggishness are $\bar{\delta} = 91$s and $\bar{\delta}_{\mathrm{s}} = 151$s. There is thus a substantial difference in sluggishness estimation using HXR as a reference over SXR.

4.3.4 Theoretical Study: Effective Recombination Coefficient, α_{eff}

The focus of this section is to examine how chemical processes in the D-region play a role in regulating ionospheric sluggishness and estimate α_{eff} from the conventional sluggishness, $\bar{\delta}$, measured from riometer observations. There are a plethora of chemistry models that describe D-region dynamics in terms of the following constituents: electrons, positive ions, anions, and heavy positive ions or cluster ions [54, 99, 103, 104, 163]. Glukhov-Pasko-Inan (GPI) is a widely recognized model that describes chemistry at D-region altitudes [54]. In brief, the GPI model describes the ionosphere as a mixture of four constituents: electrons (n_e), negative ions (n^-), positive ions (n^+), and heavy positive cluster ions (n_x^+). Assuming charge neutrality, the effective recombination coefficient is

$$\alpha_{\mathrm{eff}} = \left[\frac{\beta - \gamma\lambda}{n_e} + \alpha_d^c \frac{n_x^+}{n_e} + \alpha_d\right] = \alpha_{\mathrm{eff}}^{n^-} + \alpha_{\mathrm{eff}}^{n_x^+} + \alpha_{\mathrm{eff}}^{n^+} \tag{4.6}$$

where: γ, β, α_d, α_d^c, and λ represent electron detachment rate, electron attachment rate, electron-ion dissociative coefficient, electron-cluster ion dissociative coefficient, and negative ion to electron ratio, respectively. Table 4 lists the parameters with corresponding symbols, descriptions, and units.

Note that the GPI model uses relatively constant values of α_d and α_d^c for D-region heights,

Symbol	Name	Description	Units
γ	Electron detachment rate	The rate at which electrons detach from negative ions under solar irradiance	s^{-1}
β	Electron attachment rate	The rate at which electrons attach to neutrals under solar irradiance	s^{-1}
α_d	Dissociative recombination coefficient	Effective electron-ion rate coefficient for the dissociation reaction	$m^3 s^{-1}$
α_d^c	Dissociative recombination coefficient for cluster ions	Effective electron-ion rate coefficient for cluster ion dissociation reaction	$m^3 s^{-1}$
λ	Negative ion to electron ratio	The ratio of negative ions to electrons in the ionosphere	1

Table 4.4: List of parameters used to determine D-region's effective recombination coefficient by GPI model [54].

however, γ and β are functions of electron temperature (T_e) [54, 82]. The effective recombination coefficient, α_{eff}, depends on negative ion chemistry (first term, $\alpha_{\text{eff}}^{n^-}$), positive cluster ion chemistry (second term, $\alpha_{\text{eff}}^{n_x^+}$), and dissociative recombination rates (third term, $\alpha_{\text{eff}}^{n^+}$), with typical ranges of $10^{-11} - 10^{-12}$ $m^3 s^{-1}$, $10^{-11} - 10^{-12}$ $m^3 s^{-1}$, and $3 \times 10^{-13} - 10^{-13}$ $m^3 s^{-1}$, respectively [8, 139]. A study by Žigman et al. [163] showed that α_{eff} can also be estimated from measured δ, peak electron density, and irradiance flux as:

$$\alpha_{\text{eff}} = \frac{3}{8\delta \left(n_e^{\max} - \frac{I_\infty^{\max} \delta g m_{avg}}{\rho e k T} \cos\chi \right)} \tag{4.7}$$

where: e is the Euler's number and the base of the natural logarithm, k is the Boltzmann constant, g is the gravitational acceleration, $m_{avg} = 4.8 \times 10^{-26}$kg is the mean molecular mass [106], $\rho = 34$ eV is the average energy required to produce one electron-ion pair [158], and T $\sim$ 210 K is the averaged electron temperature of the D-region [136, 141]. Equation 4.7 was explicitly formulated to estimate the effective recombination coefficient

from VLF measurements by assuming the D-region is thin relative to the wavelength (∼1 km) and that the VLF signal encounters the ionosphere at one point in space. In fact, the VLF signal encounters the ionosphere over a range of altitudes (50-75 km), over extended horizontal dimensions, and often has multiple encounters with the ionosphere through multi-hop propagation, which smears the measurement of sluggishness spatially. In this study, sluggishness estimated from HF observations also provides a spatially-averaged realization since the HF signal passes through an ionospheric volume. Equation 4.7 can be adopted to provide a gross estimate of the effective recombination coefficient from HF observations that is consistent with the practice in VLF studies. Note that equation 4.7 only holds for the peak of an event when the electron production rate goes to zero (i.e. $\frac{dn_e}{dt}$=0). Hence, in this study equation 4.7 is only valid for $\bar{\delta}^{\text{rio}}$ estimated from riometers and no other estimation of sluggishness.

Similar to ionospheric sluggishness, α_{eff} is microscopic in nature and depends on spatial coordinates, including height. We consider the following assumptions before using equation 4.7 to estimate the effective recombination coefficient using riometer measurements: (a) the D-region is a thin layer of plasma and (b) all contribution to sluggishness in riometer measurements $\bar{\delta}^{\text{rio}}$ are coming from the D-region. By using the thin-layer approximation for the D-region, we have reduced the problem to estimating the height integrated $\bar{\alpha}_{\text{eff}}$. Recent studies on solar flare-driven ionospheric HF absorption [83, 162] suggested that the D-region of the ionosphere controls the amount of HF absorption experienced by radiowaves. Considering the absorption effect observed by the riometer is manifested by the enhancement in the electron density at the D-region, we can use $\bar{\delta}^{\text{rio}}$ to estimate $\bar{\alpha}_{\text{eff}}$ for the D-region. The primary motive behind estimating $\bar{\alpha}_{\text{eff}}$ is to examine the role of the negative ion chemistry in the D-region and its variations with flare intensity. Note, $\bar{n}_e^{\text{max}}$ is taken from Levine et al. [83] considering D-region is one thin layer concentrated around h∼74.1km. These assumptions

lead to an estimation of height integrated $\bar{\alpha}_{\text{eff}}$ valid for a thin D-region and equation 4.7 is simplified to the following:

$$\bar{\alpha}_{\text{eff}} = \frac{3}{8\bar{\delta}\left(\bar{n}_e^{\max} - \frac{I_\infty^{\max}\bar{\delta}gm_{\text{avg}}}{\rho ekT}\cos\chi\right)} \tag{4.8}$$

We use equation 4.8 with simplified D-region assumptions (Assumptions: i. D-region is one thin layer; ii. all sluggishness in riometer measurements $\bar{\delta}$ coming from the D-region) to estimate $\bar{\alpha}_{\text{eff}}$ from sluggishness measured from riometer observations using the conventional method, $\bar{\delta}^{\text{rio}}$. Note that equation 4.8 has two unknowns, $\bar{\delta}$ and $\bar{n}_e^{\max}$, which can be estimated based on some simple assumptions. We assume the D-region is a thin layer of plasma ($\sim$ 60-90 km) concentrated around 74.1 km [163], which is the main source of HF absorption [162] such that riometer observation is mostly sensitive to D-region sluggishness. These assumptions help to estimate $\bar{n}_e^{\max}$ and $\bar{\delta}$ in equation 4.8. We use Levine et al. [83] to estimate $\bar{n}_e^{\max}$ around 74.1 km altitude, and $\bar{\delta}^{\text{rio}}$ estimated from riometers to replace $\bar{\delta}$ in equation 4.8. In this simulation study, we use fitted riometer data to produce smooth $\bar{\alpha}_{\text{eff}}$ results. We fit a linear regression model between observed $\bar{\delta}^{\text{rio}}$ and logarithm of peak solar irradiance ($\log_{10} I_\infty^{\max}$) to produce smooth sluggishness estimates.

Figure 7 presents the result of the simulation study. Panel (a) shows the two inputs to equation 4.8, estimated peak electron density at 74.1 km heights following Levine et al. [83] (in red) and the $\bar{\delta}^{\text{rio}}$-fitted riometer measurement (in blue). Panel (b) shows the estimated α_{eff} from equation 4.8, with peak solar flux intensity. The region shaded in blue shows the reported range for $\alpha_{\text{eff}}^{n_x^-}$ and $\alpha_{\text{eff}}^{n_x^+}$, while the red shaded region in panel (b) shows the reported range of $\alpha_{\text{eff}}^{n^+}$ [54]. Note that for C class flares estimated α_{eff} remains almost constant between $10^{-11} - 10^{-12}\ m^3 s^{-1}$, which is the typical range of $\alpha_{\text{eff}}^{n_x^-}$ and $\alpha_{\text{eff}}^{n_x^+}$. However, with increasing peak solar irradiance α_{eff} decreases and the value drops below $10^{-15}\ m^3 s^{-1}$. The slope of the

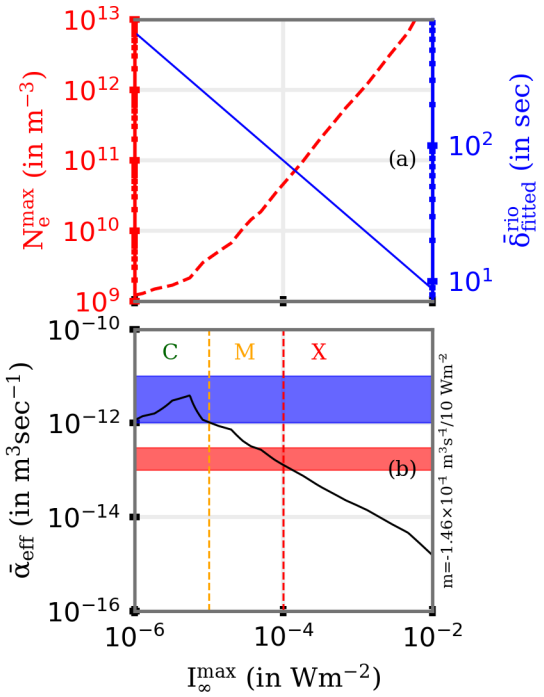

Figure 4.7: Model-data comparison of variations in (a) peak electron density at D-region heights from Levine et al. [83] (in red dashed curve) and $\bar{\delta}^{rio}$ are fitted riometer measurement, and (b) $\bar{\alpha}_{eff}$ from equation 4.8, with peak solar flux intensity. Red and blue shaded region in panel (b) represents typical ranges of the effective correlation coefficient for negative, positive cluster ion chemistry and simple ion chemistry, respectively. Vertical orange and red lines in panel (b) represent the separation between C, M, and X class flares. The slope of the black curve (m) in panel (b) is provided along the right vertical axis of the panel.

line is m $= -1.46 \times 10^{-1}\ m^3 s^{-1}/10 W m^{-2}$. One explanation for this drop in D-region α_{eff} could be an increase in D-region electron density and a decrease in electron photo-detachment rate (γ in equation (6)) under the influence of the increased solar irradiance. An increase in the electron photo-detachment rate decreases $\alpha_{eff}^{n^-}$ which leads to a decrease in the value of the effective correlation coefficient, α_{eff}.

4.4 Discussion

In this study, we have defined two new parameters for characterizing cumulative ionospheric sluggishness, $\bar{\delta}_s$ and $\bar{\delta}_c$, that are referenced to maximum slope and correlation analysis. We compared estimates of ionospheric sluggishness using both passive and active high frequency (HF, 3-30 MHz) instruments, namely riometers and SuperDARN HF radars, respectively. All three sluggishness estimates ($\bar{\delta}$, $\bar{\delta}_s$ and $\bar{\delta}_c$) from both instruments represent cumulative sluggishness along the ray path, which are indicative of the inertial property of the ionosphere and thus inherit the properties of δ. We performed a comprehensive characterization of $\bar{\delta}^{rio}$, $\bar{\delta}_s^{rio}$, $\bar{\delta}_s^{SD}$, and $\bar{\delta}_c^{SD}$ using riometers following 92 C, 63 M, and 18 X-class flares that occurred between 2006 and 2017 (Figures 4 and 5). We have also presented a comparison between the sluggishness estimates obtained with consideration of SXR and HXR (Figure 6). Finally, we used theoretical arguments to estimate $\bar{\alpha}_{eff}$ from fitted $\bar{\delta}^{rio}$ and gain some insights into the D-region chemistry (Figure 7). In this section, we summarize the findings and discuss how they inform our understanding of the physical processes that control ionospheric sluggishness.

As noted previously, sluggishness is an inertial property of the ionosphere [14, 44]. Early studies reported that sluggishness is related to recombination processes and inversely proportional to the product of electron density and α_{eff}, where α_{eff} is relatively constant for a particular latitude, local time and height. If this were the case, sluggishness would only be a function of electron density [113]. However, in this study, we found the measured sluggishness varies significantly with measuring technique (see Figures 1, 3, 4, and 5), and we also found the estimation of sluggishness using the peak time derivative (equation 3) is greater than that using the conventional definition (equation 2). The probable reason might be a larger electron density during the peak of a solar flare event than before the peak. This implies that ionospheric sluggishness is indeed inversely proportional to electron density but does not confirm that α_{eff} is a constant. This explanation does not fit the reasoning for the

smaller values of sluggishness determined from SuperDARN HF radar observations using the modified definition (refer Figure 3). The most likely explanation is the difference in the ionospheric sounding techniques between the instruments. In addition, from the KS test statistic (Figure 5 along with Table 3) described in Section 3 we found that the four different types of sluggishness estimation under consideration are statistically different from each other. Taking all these factors together we can conclude that the choice of ionospheric sounding technique impacts the sluggishness measurement. What matters then, are the relative differences in sluggishness measured by a single instrument under different conditions.

The choice of solar irradiance also impacts the sluggishness estimation, as presented in Figure 6. Historically, SXR has been used as reference data to estimate sluggishness [e.g. 113], the assumption being that SXR characterizes the intensity of ionizing radiation at D-region altitudes. However, HXR also produces a significant amount of ionization at the lower D-region heights, and photoionization at different heights is regulated by different solar irradiance wavebands that peak at different times during solar flares [67]. Moreover, because riometer observations provide a height integrated measurement of HF absorption, it is difficult to know the exact relationship of sluggishness estimates to ionospheric parameters without the help of modeling efforts. Hence, the question arises, which reference waveband should we use to extract sluggishness from the riometer measurements? We suggest referring to the ionizing solar radiation wavebands that have an optical depth associated with the altitude that is equal to the altitude of maximum HF absorption.

From the correlation analysis (Figure 4), we found that $\bar{\delta}^{\mathrm{rio}}$, $\bar{\delta}_{\mathrm{s}}^{\mathrm{rio}}$, $\bar{\delta}_{\mathrm{s}}^{\mathrm{SD}}$, and $\bar{\delta}_{\mathrm{c}}^{\mathrm{SD}}$ are positively correlated with increasing solar zenith angle, latitude, and decreasing solar SXR intensity, which is consistent with previous VLF studies [14, 113]. These results are also consistent with the physics described by Appleton [9]. Specifically, an increase in solar zenith angle produces a decrease in photoionization and electron density, which leads to an increase in

ionospheric sluggishness. All four sluggishness parameters show a quadratic dependence on local time (LT) with minima at local noon (12 LT). This finding was also reported by previous studies and easily fits into our understanding of the inverse relation between sluggishness and peak electron density. Naively, one might expect sluggishness to also decrease with latitude for similar reasons; however, panels (b-1∼4) show a positive correlation of $\bar{\delta}$ with latitude, but a strong correlation for $\bar{\delta}^{\text{rio}}$ and $\bar{\delta}_{\text{s}}^{\text{rio}}$. One possible explanation for this mixed latitude dependence is variability in α_{eff} which is known to have a strong dependence on anionic chemistry at higher latitudes [7, 103]. Further detailed analysis and modeling of sluggishness across latitudes and local time may provide further insights into the variability of D-region chemistry. Future work will also examine the statistical behavior of $\bar{\delta}_{\text{c}}$ and $\bar{\delta}_{\text{s}}$ measured from riometer and SuperDARN observations.

A focus of this study has been to estimate D-region's $\bar{\alpha}_{\text{eff}}$ from $\bar{\delta}$ measured using riometer measurements. Equation (6) describes the effective recombination coefficient in terms of negative ion formation and destruction (first term $\alpha_{\text{eff}}^{n^-}$), dissociative electron-cluster ion recombination (second term $\alpha_{\text{eff}}^{n_x^+}$), and dissociative electron-ion recombination (third term $\alpha_{\text{eff}}^{n^+}$) [54, 139, 163]. We have shown the height integrated D-region's effective ionospheric recombination coefficient ($\bar{\alpha}_{\text{eff}}$) varies by several orders of magnitude (typically between $10^{-15} - 10^{-11}\ m^3 s^{-1}$) with peak solar SXR irradiance (Figure 7). The range of values for $\bar{\alpha}_{\text{eff}}$ is consistent with those found in previous literature [52, 53, 139]. We conclude that reductions in estimated $\bar{\alpha}_{\text{eff}}$ are mainly due to drops in the negative and positive cluster ion effective recombination coefficients denoted by $\alpha_{\text{eff}}^{n^-}$ and $\alpha_{\text{eff}}^{n_x^+}$, respectively. Specifically, decreases in $\bar{\alpha}_{\text{eff}}$ are caused by enhancements in electron density (n_e) due to photoionization and to enhancements in electron detachment rate (γ) due to the sudden rise of molecular vibrational and rotational energy under the influence of energetic EM radiation [155]. Recent studies have also suggested that an increase in flare time D-region electron temperature

that changes the electron-ion dissociative coefficient (α_d) can lead to an overall drop in the effective recombination coefficient [see Figure 5 in 12, 111]. Taken all together, we conclude that intense solar flares alter the negative and positive cluster ion chemistry at the D-region altitude, which leads to a change in the inertial property of the ionosphere that is ionospheric sluggishness. More detailed data analysis and modeling efforts are required to fully understand D-region negative ion and positive cluster ion chemistry during solar flares and how it is affected by changes in D-region electron temperature.

4.5 Conclusion

In this study, we have compared estimates of ionospheric sluggishness obtained from riometer and SuperDARN HF radar observations using three different methodologies. A correlation analysis was conducted on the sluggishness estimated from riometer observations using a conventional method. The study uses two different D-region chemistry equations to describe the physical basis of sluggishness from the perspective of photochemical reactions. From the simulation study we estimated the height integrated D-region's effective recombination coefficient ($\bar{\alpha}_{\text{eff}}$) and examined its variation with peak solar soft X-ray flux. We found that the choice of ionospheric sounding technique and reference solar irradiance waveband affect the estimation of sluggishness. We also found that ionospheric sluggishness is anti-correlated with solar X-ray radiation intensity, as expected. We showed that sluggishness, estimated using different instruments and techniques, minimizes at local solar noon. We showed that the height integrated D-region's effective recombination coefficient ($\bar{\alpha}_{\text{eff}}$) varies by several orders of magnitude, typically between $10^{-15} - 10^{-11}$ $m^3 s^{-1}$, with the peak soft X-ray irradiance. The results suggest that electron density and negative ion chemistry under the influence of EUV and X-ray fluxes are major determinants of sluggishness. Future work

will examine how sluggishness depends on latitudinal factors and complex-ion (negative and positive cluster ion) chemistry and geomagnetic activity.

Acknowledgments

SC thanks to the National Science Foundation for support under grant AGS-1341918. KAZ acknowledges support from the Chief of Naval Research (CNR) under the NRL 6.1 Base Program. We wish to acknowledge the use of the NOAA/GOES X-ray data (from https://satdat.ngdc.noaa.gov/sem/goes/data/) for flare confirmation and analysis. We thank NRCan for providing the riometer data and the University of Calgary for providing riometer data directly via http://data.phys.ucalgary.ca/. We also thank all participants in the worldwide SuperDARN collaboration for the distribution of SuperDARN data via http://vt.superdarn.org/tiki-index.php?page=Data+Access. The majority of analysis and visualization was completed with the help of free, open-source software tools such as matplotlib [68], IPython [118], pandas [97], Spacepy [107], PyForecastTools [108], and others [e.g. 102]. All the analysis (code and datasets) used in the study are indexed in this webpage [30].

Chapter 5

A Modeling Framework for Estimating Ionospheric HF Absorption Produced by Solar Flares

S. Chakraborty[11], J. B. H. Baker[1], R. A. D. Fiori[2], J. M. Ruohoniemi[1], and K. A. Zawdie[3]

[1]Bradley Department of Electrical and Computer Engineering, Virginia Tech, Blacksburg, USA

[2]Geomagnetic Laboratory, Natural Resources Canada, Ottawa, Ontario, Canada

[3]Space Science Laboratory, US Naval Research Laboratory, Washington DC, USA

Chakraborty, S., Baker, J. B. H., Fiori, R. A. D., Ruohoniemi, J. M., & Zawdie, K. A. (2021). A Framework to Estimate Ionospheric HF Absorption in Response to a Solar Flare. Radio Science, Under Review.

Abstract

Over-the-Horizon (OTH) communication is strongly dependent on the state of the ionosphere, which is susceptible to solar flares. Trans-ionospheric high frequency (HF, 3-30 MHz) signals can experience strong attenuation following a solar flare that lasts typically for an hour, commonly referred to as Shortwave Fadeout (SWF). In this study, we examine the role of dispersion relation and collision frequency formulations on the estimation of SWF in riometer observations using a new physics-based model framework. The new framework first uses modified solar irradiance models incorporating high-resolution solar flux data from the GOES satellite X-ray sensors as input to compute the enhanced ionization produced during a flare event. The framework then uses different dispersion relation and collision frequency formulations to estimate the enhanced HF absorption. The modeled HF absorption is compared with riometer data to determine which formulation best reproduces the observations. We find the Appleton-Hartree dispersion relation in combination with the averaged collision frequency profile reproduces riometer observations with an average skill score of 0.4, representing 40% better forecast ability than the existing DRAP model. Our modeling results also indicate that electron temperature plays an important role in controlling HF absorption. We suggest that adoption of the Appleton-Hartree dispersion relation in combination with the averaged collision frequency be considered for improved forecasting of ionospheric absorption following solar flares.

Plain Language Summary

Sudden bursts of electromagnetic radiation from the Sun, also known as solar flares, alter the physical properties of the ionosphere. The sudden enhancement in incoming solar radiation affects over-the-horizon (OTH) radio communication channels on the dayside of the Earth, commonly known as shortwave fadeout (SWF). This study describes a new approach for estimating ionospheric radiowave absorption, using different formulations of wave dispersion

relation and collision frequency and compares their relative merits using direct observations of absorption in the ionosphere. We examine how different physical parameters, such as the location of the transmitter, intensity of the solar flare, ionospheric composition, and background conditions, such as electron temperature impact SWF.

5.1 Introduction

A solar flare is a sudden enhancement in the Sun's electromagnetic radiation, specifically in the EUV and X-ray wavebands of the solar spectrum, lasting for a few tens of minutes to several hours [60, 122, 142]. The intensification of solar radiation during a solar flare enhances the plasma density via photoionization in the Earth's lower ionosphere (D and lower E region, ∼60-105km) [39]. This sudden enhancement of electron density leads to an increase in ionospheric high-frequency (HF: 3-30 MHz) radiowave absorption that disrupts over-the-horizon (OTH) communication, commonly known as the Dellinger effect or Shortwave Fadeout (SWF) [40]. A statistical study by DeMastus and Wood [41] showed there is almost a one-to-one relationship between an earthward directed solar flare and the occurrence of SWF. More recent studies have shown how the duration and intensity of SWF depend on duration and peak intensity of the solar flare, location of the transmitter and receiver, frequency of the radiowave, and the background ionosphere [27, 47]. SWF impacts on HF radiowave propagation can have impacts on sensitive systems. For example, a recent study by Redmon et al. [123] demonstrates solar flare-driven impacts to emergency HF communications supporting humanitarian aid services in conjunction with Hurricane Irma relief efforts in the Caribbean. Further progress in understanding flare-driven enhanced HF absorption is essential for mitigating the impacts on trans-ionospheric radiowave systems, including ground-to-ground radio communications, amateur radio links, satellite communi-

cation systems, and Global Navigation Satellite Systems [50, 77].

Historically, riometers [e.g. 61, 66, 85] and ionosondes [e.g. 44, 150] have been the primary instruments used to study SWF. More recently, incoherent scatter radar (ISR) [e.g. 100, 115], Super Dual Auroral Radar Network (SuperDARN HF radars) [e.g. 47, 156], GPS TEC measurements [e.g. 4, 89], digisondes [e.g. 59, 161], and amateur radio networks [e.g. 50] have been used to study solar flare effects in the ionosphere. While ionosodes and digisondes provide information about the ionospheric plasma density enhancement, riometers directly observe the enhanced HF absorption due to D region plasma-neutral collisions. ISR observations are used to study ionospheric temperature, plasma density, and horizontal and vertical plasma drift parameters. SuperDARN radars have observed a different feature of flare-driven HF anomaly, namely the "Doppler flash" [see Fig. 3 25]. Digisondes and SuperDARN HF radars are affected severely by radio blackout while riometers are better suited to capture the full spatiotemporal evolution of HF absorption. Imaging riometers have also been used to study the spatial and frequency dependence of SWF [e.g. 66, 73]. We use riometer observations in this study.

Stonehocker [147] first developed an empirical relationship between solar irradiance and HF absorption observed by WWV station (call letters of National Bureau of Standards, NIST, radio station). That study laid a foundation for nowcasting solar flare-driven HF absorption and culminated in the development of an operational NOAA (National Oceanic and Atmospheric Administration) SWPC (Space Weather Prediction Center) DRAP (D Region Absorption Prediction) model. Some recent studies have focused on building data-driven nowcast models to predict enhanced HF absorption at different operating frequencies, its duration, and the highest frequency that is impacted by 1dB absorption (HAF) following a solar flare [116, 131]. Examples of nowcast models include DRAP [135], the data-driven ionosonde model of Sato [134], and HIDIVE (HF Investigation of D region Ionospheric Variation Exper-

iment) [42]. Some of these nowcast tools combine semi-empirical and physics-based models to capture radiation transport, ionization, chemical kinetics, and plasma-neutral collision dynamics [42, 83]. A recent study by Levine et al. [83] described a physics-based approach that provides significantly better estimates of HF absorption than the data-driven DRAP model [135]. Nevertheless, DRAP has proved to be an effective model for forecasting the operational impacts of solar X-ray flux on HF communication and is widely accepted by the space science and amateur radio communities [50]. Thus we have used DRAP as the baseline model in this study.

Despite the recent advances in our abilities to model and forecast HF absorption, we still do not have a clear understanding of flare time D-region dynamics. Most of the data-driven models, and DRAP in particular, only consider solar EUV and X-ray irradiances, solar zenith angle, and operating frequency as input parameters [5, 134, 135]. However, it is well known that ionospheric HF absorption is strongly dependent on plasma-neutral collisions and photochemistry at D region heights ($\sim$60-105 km), factors which are neglected in most of the existing prediction models [162]. Levine et al. [83] showed that during extreme events, the DRAP model underestimates HF absorption by more than 20 dB. Another largely overlooked influence is electron temperature. The study by Chakraborty et al. [28] suggested ionospheric electron temperature may be an important parameter through its impact on collision frequency. Accurate estimation of HF absorption may have to include electron temperature as well as a collision frequency model and a wave dispersion relation formulation [162].

This study presents a comprehensive analysis of HF absorption during SWF events by comparing different formulations of wave dispersion relation and collision frequency. We estimate the enhanced electron density from a physics-based model and then calculate HF absorption using different wave dispersion relations and collision frequency formulations. We compare

our estimates against riometer observations and DRAP model estimates to determine the influence of electron temperature and collision frequency. A secondary objective is to examine the role of collision frequency and electron temperature on HF absorption by conducting a simulation study. We find that the new modeling framework produces better estimates of HF absorption than DRAP estimations. The paper is organized as follows: Section 5.2 provides a brief introduction to instruments and datasets used in the study; Section 5.3 describes the architecture and parameterization of the model; Section 5.4 presents model-data comparisons and a simulation study to examine the influence of model parameters; and finally in Section 5.5 we discuss the results in the context of similar work.

5.2 Instrumentation

The primary datasets used in this study are solar flare information and ionospheric HF absorption observations from the GOES X-ray sensor and riometers, respectively. The GOES X-ray data provides information about the solar flares that is used as an input to the model while the riometer data provides information about the ionospheric HF absorption across various latitudes and longitudes that is used to validate the model outputs.

Solar X-ray flux information was obtained from the National Oceanic and Atmospheric Administration (NOAA) GOES 15 satellite [93]. The solar x-ray sensors on GOES 15 satellites have two channels, namely hard X-ray (0.05-0.4 nm, HXR) and soft X-ray (0.1-0.8 nm, SXR). The NOAA archive supports high resolution (2s) and low resolution (1-minute averaged over high resolution) X-ray data and our model can use either resolution as an input. We used 2s resolution data to run the model and output 1-minute resolution HF absorption data. The solar flux information from both the X-ray channels are used to capture the flare-driven dynamics in the model. While F10.7 index data captures solar cycle variations. The F10.7

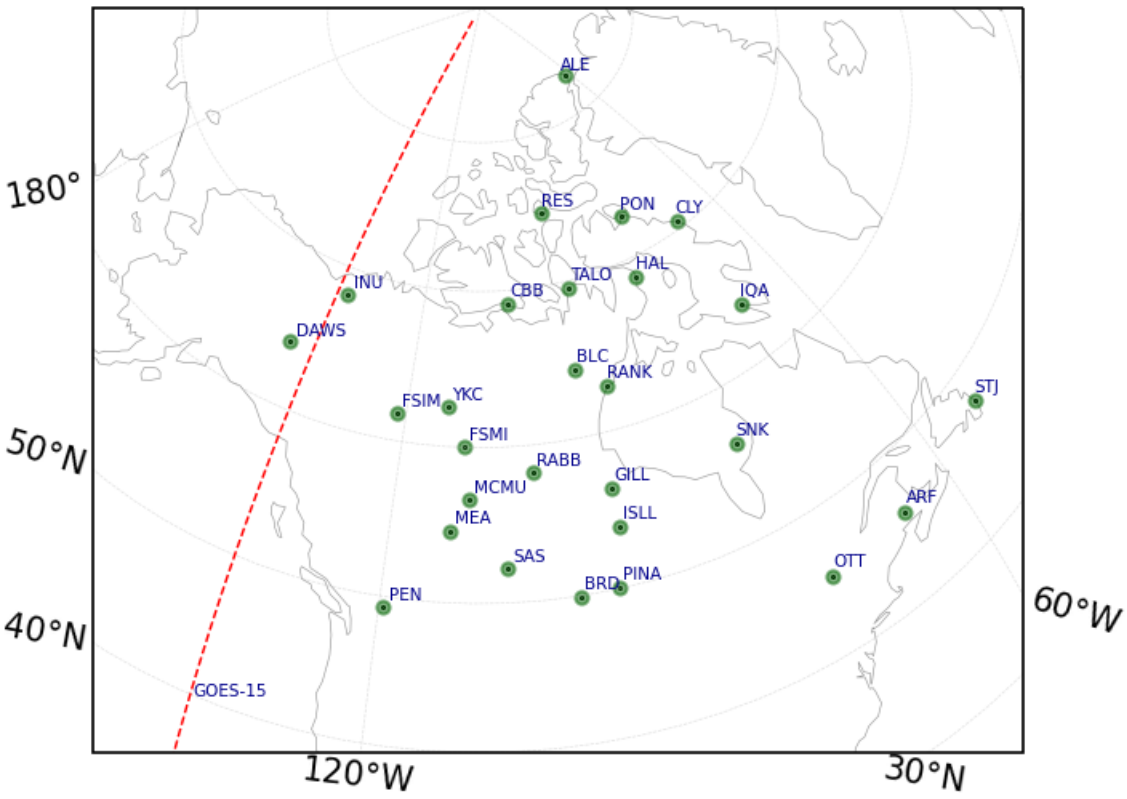

Figure 5.1: Locations of the various riometers used in the study. The black dots identify riometer locations while the green circles represent the 100-km fields-of-view. The red line at -135.3^o longitude indicates the longitudinal location of the GOES 15 satellite.

index is a measure of the noise level generated by the Sun at a wavelength of 10.7 cm and is widely used of longer time solar activity.

A riometer is a ground-based passive radio receiver that provides information about HF absorption in the ionosphere by measuring variations in cosmic radio noise at 30 MHz [22, 46, 85]. The cosmic noise absorption (CNA) values used in this study are taken from a network of riometers jointly operated by Natural Resources Canada (NRCan) and the University of Calgary (Geospace Observatory riometer, or GO-RIO) [e.g. 80, 133]. Riometer data from the NRCan and UofC sites were provided at 1s and 5s resolution, respectively. For this study we down-sampled both datasets to 1-minute averages for the purpose of data-model

comparison. Figure 5.1 presents the location of the instruments used in this study. Table 5.1 provide station name, code, geographic, and geomagnetic coordinates for all the riometers used in this study. The coverage is seen to extend nearly across the full expanse of the Canadian land mass.

Code	Geo-Latitude (^{o})	Geo-longitude (^{o})	Mag-Latitude (^{o})	Mag-Longitude (^{o})
TALO	69.5	266.4	77.5	-26.1
RANK	62.8	267.9	71.6	-22.0
PINA	50.0	264.0	59.6	-26.4
GILL	56.4	265.4	65.6	-25.0
DAWS	64.0	220.9	66.3	-83.2
FSIM	61.8	238.8	67.3	-62.7
FSMI	60.0	248.0	67.1	-50.3
RABB	58.2	256.3	66.5	-38.5
ISLL	53.9	265.3	63.2	-24.8
MCMU	56.7	248.8	64.1	-48.3
ALE	82.5	297.7	87.0	68.7
RES	74.7	265.1	82.0	-32.0
PON	72.7	282.0	80.2	2.0
CLY	70.5	291.5	77.5	16.8
CBB	69.1	255.0	76.3	-44.8
HAL	68.8	278.8	76.9	-4.6
INU	68.3	226.5	71.4	-80.4
BLC	64.3	264.0	72.7	-28.5
IQA	63.7	291.5	71.2	14.3
YKC	62.5	245.5	69.1	-54.7
SNK	56.3	281.0	65.3	-1.7
MEA	54.6	246.7	61.8	-50.4
SAS	52.2	252.9	60.5	-41.9
BRD	49.9	260.0	59.2	-31.8
PEN	49.3	240.4	55.7	-56.8
STJ	47.6	307.3	52.4	30.8
ARF	46.0	294.0	53.8	15.2
OTT	45.4	284.5	54.8	2.7

Table 5.1: List of riometers used in this study. Riometers with four and three letter station codes are operated by GO-RIO and NRCan, respectively.

5.3 Model Description

This section provides an overview of the HF absorption theory and describes the architecture, inputs, and outputs of our new model. The HF absorption experienced by an ionospheric radiowave is a consequence of plasma-neutral interactions. We use the following equation to estimate the total HF absorption (in dB) [39]:

$$\beta_a = -8.68 \int_S \kappa . ds$$

where: β_a, κ, and ds are the total HF absorption along path S, the imaginary part of the refractive index ($\eta = \mu + i\kappa$) derived from the wave dispersion relationship, and incremental distance along the path of propagation. The refractive index of a partially ionized media describes the plasma-neutral interaction [e.g. 15, 138] and is parameterized by the collision frequency. The collision frequency of a medium depends on electron temperature [e.g. 39, 139]. Following Zawdie et al. [162], we implement two separate dispersion relations, namely, Appleton-Hartree [e.g. 39] and Sen-Wyller [49, 95, 140], and four formulations of the plasma-neutral collision frequency (see Table 5.2). The Appleton-Hartree dispersion relation assumes a cold plasma approximation and only uses averaged collision frequencies (i.e., averaged over electron temperature/energy space) [139]. In contrast, the Sen-Wyller dispersion relation assumes that collisions depend on electron energy and uses a monoenergetic collision frequency to simulate plasma-neutral interaction and absorption [95, 162]. The Sen-Wyller dispersion relation is a generalized form of the Appleton-Hartree dispersion relation.

Figure 5.2 presents a schematic of the architecture of the model showing how the different modules, both borrowed and newly developed, are interconnected. Following Figure 5.2, our model estimates ionospheric HF absorption for a specific HF frequency and normal incident (i.e. vertical) O-mode propagating radiowave by utilizing the following steps. First,

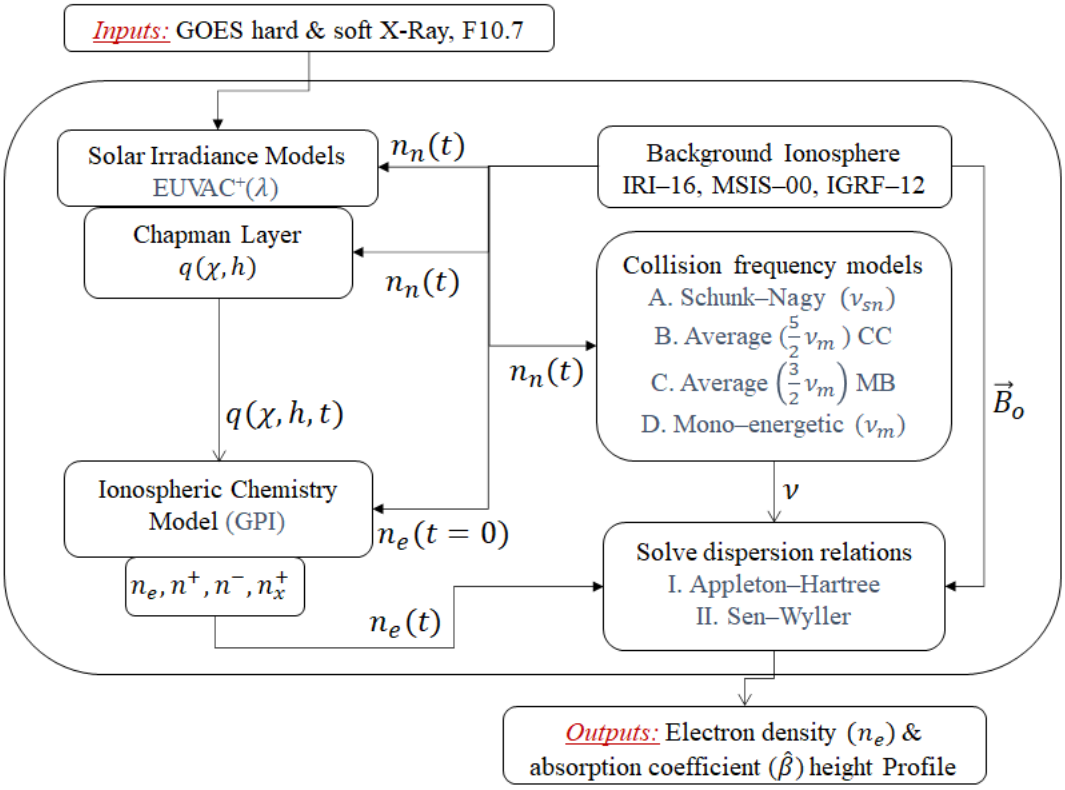

Figure 5.2: Model architecture for calculating electron density and HF absorption height profiles showing the component modules (borrowed, modified, and developed) and their interconnection.

Dispersion Relation	Collision Frequency	Notation
Appleton-Hartree	Schunk-Nagy (ν_{sn}) [eqn. (19-28) in, 162]	$\beta_{ah}(\nu_{sn})$
Appleton-Hartree	Average: Chapman-Cowling Integral (ν_{av}^{cc}) [eqn. (31) in, 162]	$\beta_{ah}(\nu_{av}^{cc})$
Appleton-Hartree	Average: Maxwellian-Boltzmann Integral (ν_{av}^{mb}) [eqn. (32) in, 162]	$\beta_{ah}(\nu_{av}^{mb})$
Sen-Wyler	Monoenergetic (ν_{me}) [eqn. (30) in, 162]	$\beta_{sw}(\nu_{me})$

Table 5.2: The four combinations of dispersion relation-collision frequency formulations used in the new model.

it simulates IRI-2016 [19], IGRF-2016 [151], and MSIS-2000 [119] to create a background ionosphere. Second, it takes F10.7, GOES HRX, and SRX as inputs and feeds them to a modified solar irradiance model (EUVAC$^+$) and Chapman layer profile to calculate the height profile of energy deposited by the flare-enhanced solar radiation [125, 126, 143]. To

capture the flare-enhanced solar radiation we modified the last two X-ray bins of the EUVAC model with GOES soft and hard X-ray observations. Next, an ionospheric chemistry model is used to estimate the electron density height profile [54, 103, 104]. We used the Glukhov-Pasko-Inan (GPI) model to describe the chemistry at D-region altitudes (∼60-90 km) [54], while chemistry equations for E and F-region altitudes are borrowed from Schunk and Nagy [139]. Finally, the model uses different dispersion relation and collision frequency formulations (listed in Table 5.2) to estimate HF absorption height profiles. Note that all four combinations of dispersion relation-collision frequency formulations are parameterized by electron temperature. Therefore, any changes in the ionospheric electron temperature should alter the collision frequencies and associated HF absorption estimations listed in Table 5.2.

Figure 5.3 presents an example output of the model run before (left column) and after (right column) a solar flare at 16:22 UT on 11 March 2015. The top row shows density profiles of four different plasma constituents, while the middle and lower rows show height profiles of the ion-neutral collision frequency and HF absorption at 30 MHz using the dispersion relation and collision frequency formulations listed in Table 5.2, respectively. The four different plasma constituents are, electrons (n_e), positive ions (n^+, i.e. O_2^+, NO^+), negative ions (n^-, i.e. O_2^-, HNO_3^-), and positive cluster ions (n_x^+, i.e. $(H_2O)_nH^+$). Finally, we integrate the HF absorption height profiles shown in the bottom panels of Figure 5.3 to get the total O-mode HF absorption experienced by the EM wave passing vertically through the ionosphere. The model framework is parameterized by electron temperature; thus, the model can adjust the collision frequencies and associated HF absorption based on electron temperature input. The model is more suited to capturing the flare time density and absorption enhancement at D and lower E region heights.

We comment on the uncertainties associated with the individual components of the modeling

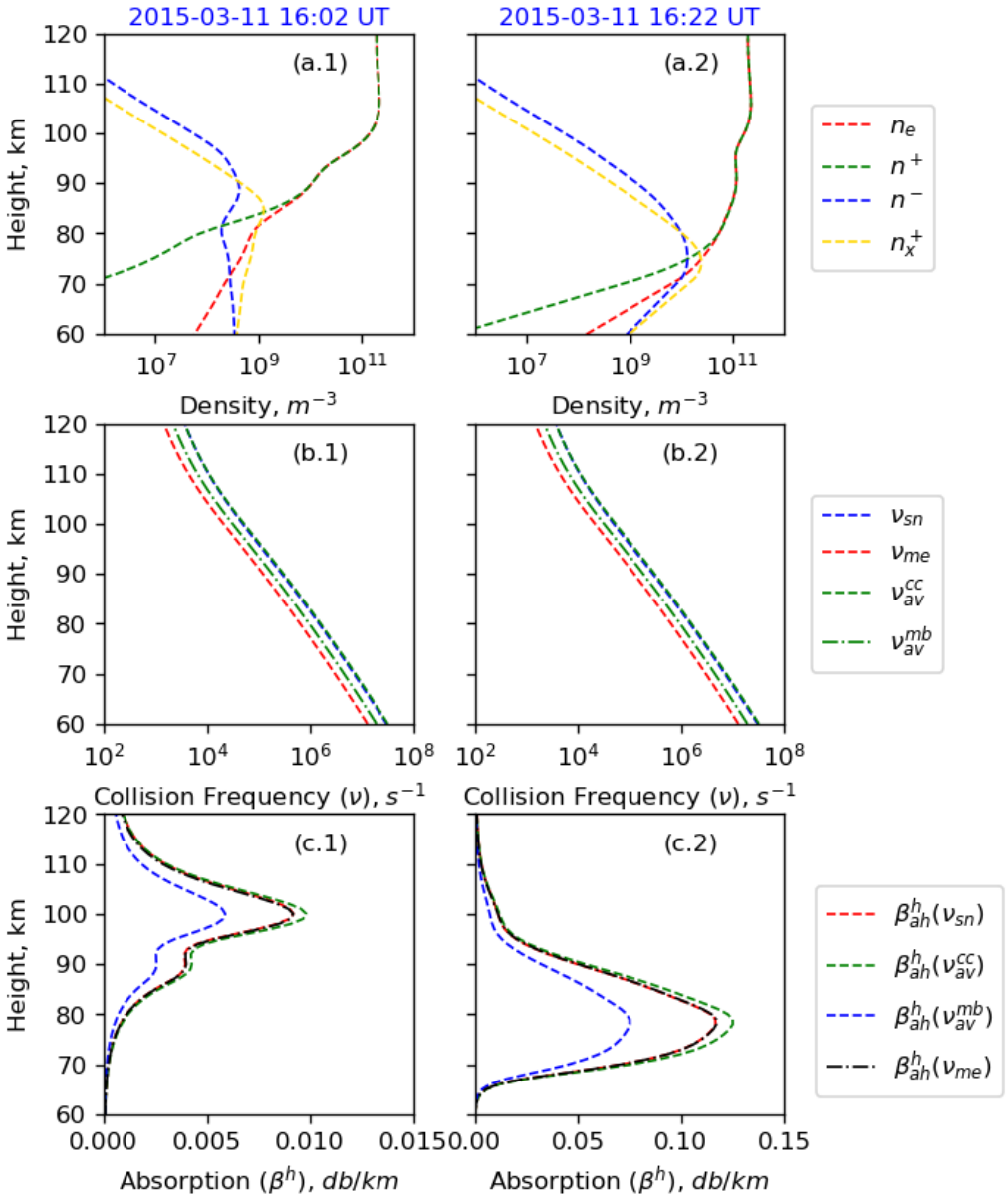

Figure 5.3: Modeled height profiles at 16:02 UT (left column) and 16:22 UT (right column) on March 11, 2015 (top to bottom): (a) densities of electrons, positive ions, negative ions, and positive cluster ions; (b) the four different collision frequency formulations (see Table 5.2); and (c) the corresponding HF absorption profiles. The left and right columns correspond to before and after a solar flare, respectively. Different ionospheric constituents (top row), collision frequencies (middle row), and HF absorption estimated using different formulations (bottom panel) are presented in different colors and mentioned in the legends on the right.

framework. The background daily ionospheric parameters, such as number densities, electron and neutral temperatures, and magnetic field strength that are obtained from IRI-2016, MSIS-2000, and IGRF-2016 models do not have uncertainties assigned to them [11]. Our framework uses these parameters from these model components to establish an initial background ionosphere for the simulation. In future work, we plan to characterize the impact of variability in parameter values on model outputs and to consider diurnal, seasonal, and solar-cycle variations. Also, the framework in its current form assumes that the ionospheric electron temperature following a solar flare remains unaltered. The framework can be run with a user specified initial electron temperature or with the electron temperature obtained from IRI-2016. We plan to model the evolution of the electron temperature of the ionosphere as a step towards more accurate estimations of collision frequencies and HF absorption.

The framework counts other components such as input solar irradiance, GPI ionospheric chemistry [54], collision frequency and dispersion relation formulations. In this study, we have tested the sensitivity of the model outputs to variation in the inputs of collision frequency and dispersion relation formulations. We plan to conduct a sensitivity analysis to examine the impact of variability in solar irradiance, ionospheric chemistry, and electron temperature.

5.4 Results

In this section, we compare the outputs from the four formulations listed in Table 5.2 with the DRAP model output and the riometer observations. First, we present a classic example of shortwave fadeout seen in the Ottawa riometer data; then, we provide a few extreme solar flare cases. We analyze the influence of operating frequency, collision frequency, and electron temperature, on the estimation of HF absorption. Finally, we benchmark and validate the model performance by comparing with the riometer observations and the DRAP model.

5.4.1 Event Study: 11 March 2015

On 11 March 2015 an X2.1 class solar X-ray flare erupted from a solar active region located at approximately -16^o latitude and 14^o longitude in the heliographic inertial coordinate system. The start, peak and end times of flare activity are approximately 16:10 UT, 16:22 UT, and ~17:00 UT, respectively. By examining the background geomagnetic conditions Fiori et al. [see Sec. 3, 47] argued that the enhancement in HF absorption observed by the riometer during this event is solely attributed to the solar flare. We chose this classic example of shortwave fadeout to do a preliminary analysis of the performance of our model predicting HF absorption produced by an X-class flare.

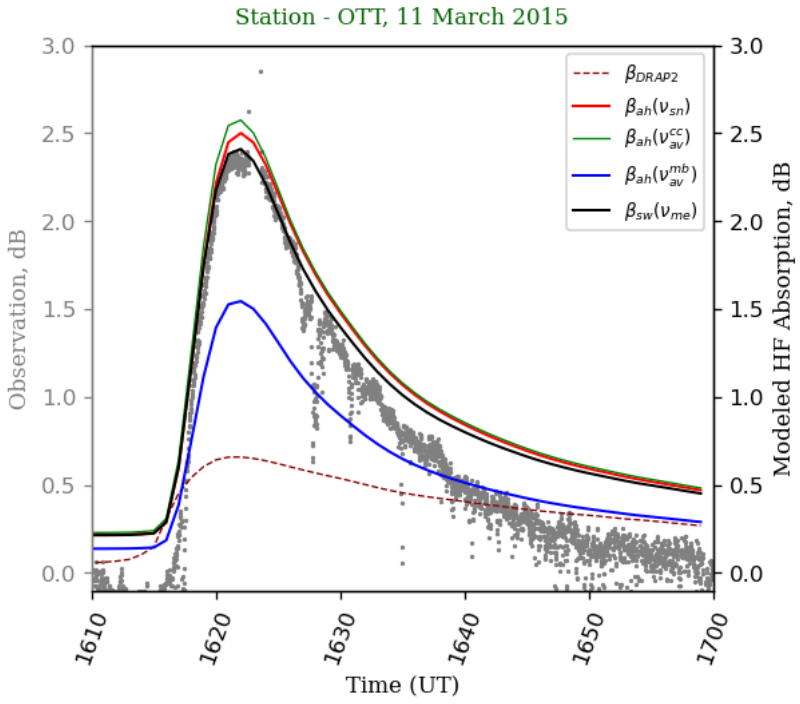

Figure 5.4: A data-model comparison of HF absorption for an SWF event observed using Ottawa riometer (gray dots) following a solar flare on 11 March 2015. The prediction of the new model using the four different dispersion and collision frequency formulations are shown by the solid red, green, blue, and black curves, respectively, while the prediction by DRAP is shown with the dark-red dashed curve. See Table 5.2 for an explanation of model notation.

Figure 5.4 presents the model-data comparison of the HF absorption observed by the Ottawa riometer (gray dots) compared to estimates from our model using the four formulations shown in Table 5.2 (solid curves) and the DRAP model (dashed curve). It can be seen that, (1) the Sen-Wyller dispersion relation with monoenergetic collision frequency $[\beta_{sw}(\nu_{me})]$ and the Appleton-Hartree dispersion relation with the Schunk-Nagy $[\beta_{ah}(\nu_{sn})]$ and averaged collision frequency (Chapman-Cowling Integral) $[\beta_{ah}(\nu_{av}^{cc})]$ formulations predict accurately the rise and peak in absorption for this event and (2) the Appleton-Hartree dispersion relation with averaged collision frequency (Maxwell-Boltzmann) $\left[\beta_{ah}(\nu_{av}^{mb})\right]$ formulation underestimates the HF absorption. The DRAP model (dashed curve) severely underestimates the HF absorption, a result that has been found previously [83]. Note that, Schumer [137] also recognizes the underestimation of HF absorption by the DRAP model. To compare these four formulations and the DRAP model more quantitatively, we computed root-mean-square errors (RMSE) of the absorption estimates with reference to the riometer observations. We computed overall RMSE and RMSE during the peak of the solar flare (RMSEp). The results are displayed in Table 5.3. It can be seen that RMSE and RMSEp are smallest for the Sen-Wyller dispersion relation with the monoenergetic collision frequency formulation. The Appleton-Hartree dispersion relation with Schunk-Nagy collision frequency and averaged collision frequency (Chapman-Cowling Integral) formulations produces the second and third best results for this event study. However, there are no significant differences between RMSE and RMSEp for these three formulations. This leads us to conclude that the the Sen-Wyller dispersion relation with the monoenergetic collision frequency formulation [162] produces the best comparison with the riometer measurements for this event.

Formulation	RMSE, dB	RMSEp, dB
$\beta_{ah}(\nu_{sn})$	0.32	0.16
$\beta_{ah}(\nu_{av}^{cc})$	0.31	0.18
$\beta_{ah}(\nu_{av}^{mb})$	1.34	1.12
$\beta_{sw}(\nu_{me})$	0.28	0.14
DRAP	0.82	2.28

Table 5.3: RMSE and RMSEp for four combinations of dispersion relation-collision frequency formulations and DRAP during the solar flare event at 16:22 UT on 11 March 2015.

5.4.2 Event Study: September 2017 Solar Storm

In this subsection, we use our new model to estimate HF absorption during three extreme solar flare events that occurred during the September 2017 solar storm [160] and compare the results with observations and simulation results presented in Levine et al. [83]. The data presented in Levine et al. [see their Fig. 5, 83] was recorded by ionosondes located in Bedford, MA (42.4906^{o}N, −71.2760^{o}E) and Stockbridge, NY (42.9912^{o}N, −75.5993^{o}E) using near-vertical ionospheric sounding (NVIS) propagation links.

Figure 5.5 presents data-model comparisons during the M2.9 flare (left), the X9.3 flare (middle) and the X1.7 flare (right). The upper row shows SXR and HXR solar flux data from the GOES satellite. The lower row shows HF absorption observed by the Bedford ionosonde (gray diamonds) compared to predictions from our model using the four different collision frequency formulations (solid curves), the DRAP model (dark red dashed), and the Levine et al. [83] model (red dots). The ionosonde observation presented in the figure is O mode attenuation at 6.4 MHz. As the ionosondes were operating in NVIS mode with an elevation angle of 55^o, we converted the one-way vertical path O mode absorption into a two-way oblique absorption (suggested by Levine et al. [83]).

It can be seen that the new model is able to accurately capture the trends in the O mode attenuation for the three different flare events. Among the four formulations, $\beta_{ah}(\nu_{sn})$,

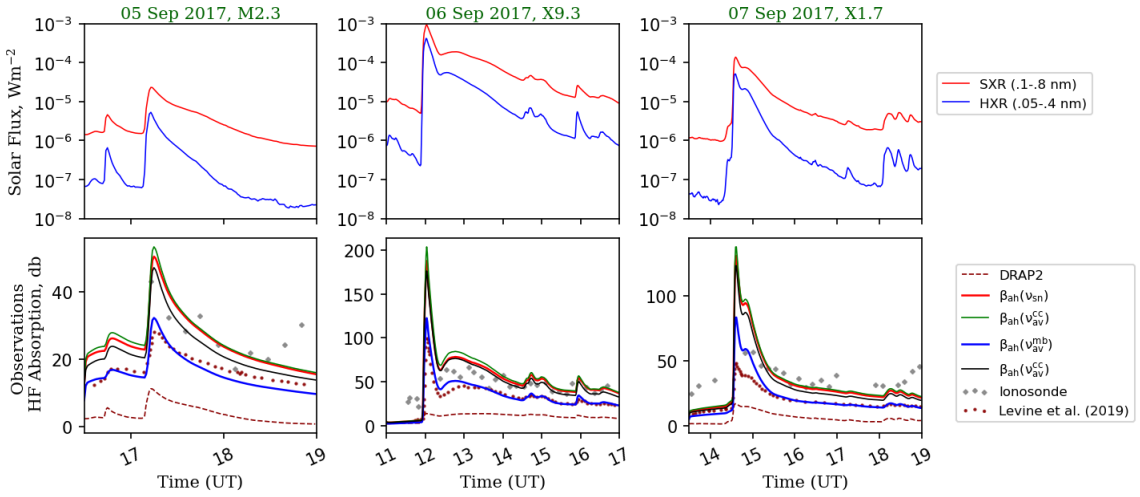

Figure 5.5: Modeled HF absorption during an M2.9 flare (left), an X9.3 flare (middle) and an X1.7 flare (right) from 5-7 September 2017.The upper row shows GOES SXR and HXR solar flux data. The lower row shows HF absorption observed by the Bedford and Stockbridge ionosondes (gray diamonds) compared to predictions from our model using the four different collision frequency formulations (solid curves), the DRAP model (dark red dashed), and the Levine et al., (2019) model (red dots). See Table 5.2 for an explanation of model notation.

$\beta_{ah}(\nu_{cc}^{av})$, and $\beta_{sw}(\nu_{me})$ are able to capture the attenuation trends more accurately than the $\beta_{ah}(\nu_{mb}^{av})$ formulation and the DRAP model. This is consistent with the case study we presented in the previous subsection. In addition, $\beta_{ah}(\nu_{sn})$, $\beta_{ah}(\nu_{cc}^{av})$, and $\beta_{sw}(\nu_{me})$ underestimate the attenuation before the peak of the solar flare for the X9.3 and X1.7 events. As suggested by Levine et al. [83], this might be due to the background condition of the ionosphere, such as the electron temperature. Chakraborty et al. [see Fig. 3 28] showed that co-occurring space weather events can alter the ionospheric background conditions, which in turn affects the flare response observed by the HF instruments.

5.4.3 Statistical Analysis

Here we present a statistical analysis of our model performance using 21 X-class and 37 M-class solar flare events recorded between 2011 to 2017. The solar flare events were selected

from GOES XRS reports maintained by NOAA when the GO-RIO and NRCan riometers were predominantly located on the dayside and measured an absorption peak of at least 0.5 dB and at least 0.2 dB greater than the minimum absorption during the flare interval. Each solar flare event affects five riometers on average, ∼410 individual riometer absorption events were collectively observed in total. To statistically compare the performance of the four model formulations we used a forecast skill score defined by $\left(\mathcal{S}_F = 1 - \frac{RMSE_{model}}{RMSE_{DRAP}}\right)$ [70]. The forecast skill score quantifies the relative accuracy of our new model forecasts against the "reference" forecasts of the DRAP model. A skill score of zero thus indicates no improvement over the DRAP forecast while negative and positive values indicate inferior and superior performance, respectively.

Figure 5.6 presents the distribution of forecast skill score across different local time (LT)-solar zenith angle (SZA) and magnetic local time (MLT)-magnetic latitude (MLAT) sectors in the left and right columns, respectively. From top to bottom, the rows present skill score distributions for the four different formulations listed in Table 5.2. Data are binned by 1 LT-9^{o}SZA and 1 MLT-9^{o}MLAT bins. Data are limited to geographic latitudes $> 45.4^o$ due to the location of the rioemeter network, which limits data to SZA $> 35^o$ and MLAT $> 50^o$. The mean value ($\bar{\mathcal{S}}_F$) and 2.5$^{\text{th}}$-97.5$^{\text{th}}$ percentile ($\{\mathcal{S}_F\}$) skill score values for each formulation is provided in the top left corner of the row. It can be seen that on average performance of all four formulations, $\beta_{ah}(\nu_{av}^{cc})$, $\beta_{ah}(\nu_{av}^{mb})$, $\beta_{ah}(\nu_{sn})$, and $\beta_{sw}(\nu_{me})$ are significantly better than the DRAP. Among four formulations, $\beta_{ah}(\nu_{av}^{cc})$, $\beta_{ah}(\nu_{sn})$, and $\beta_{sw}(\nu_{me})$ have comparable average skill score ∼0.4 and performing marginally well than $\beta_{ah}(\nu_{av}^{mb})$. Considering skill scores for all four formulations across different LT-SZA sectors, the data-model comparison clearly shows that the efficiency of the model maximizes after local solar noon (∼14-15 LT) and drops-off in the morning and dusk sectors. Similarly, from the skill score distribution across the MLT-MLAT sectors we find model efficiency maximizes in the 6-9 MLT sector. The model

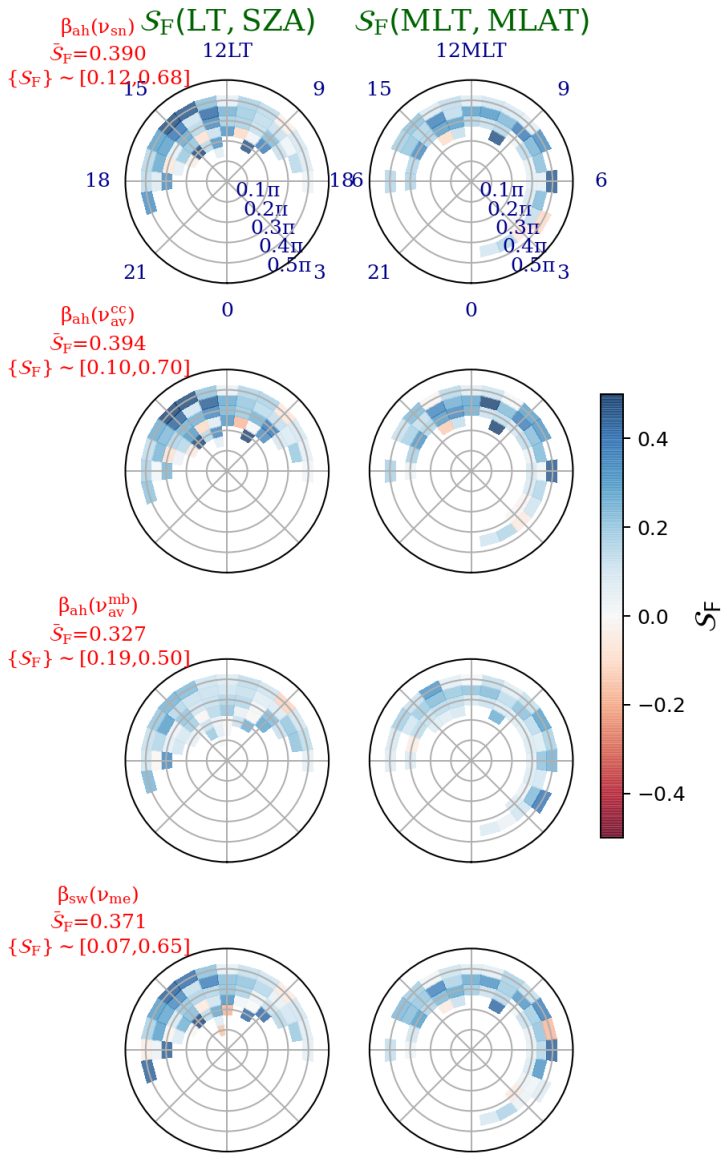

Figure 5.6: Modeled forecast skill scores ($\mathcal{S}_F$) maps: (left) in local time (LT) and solar zenith angle (SZA) axis, (right) in magnetic local-time, and magnetic latitude. Each row corresponds to skill associated with the formulations listed in Table 5.2. Mean skill score ($\bar{\mathcal{S}}_F$) and 2.5$^{\text{th}}$-97.5$^{\text{th}}$ percentile values ($\{\mathcal{S}_F\}$) of the each type of formulation are provided in the top left corner of each row. See Table 5.2 for an explanation of model notation.

skill scores for all four formulations show dependencies on solar zenith angle and magnetic latitude as well.

Figure 5.7 presents a correlation analysis of the model forecast skill ($\mathcal{S}_F$) with solar zenith an-

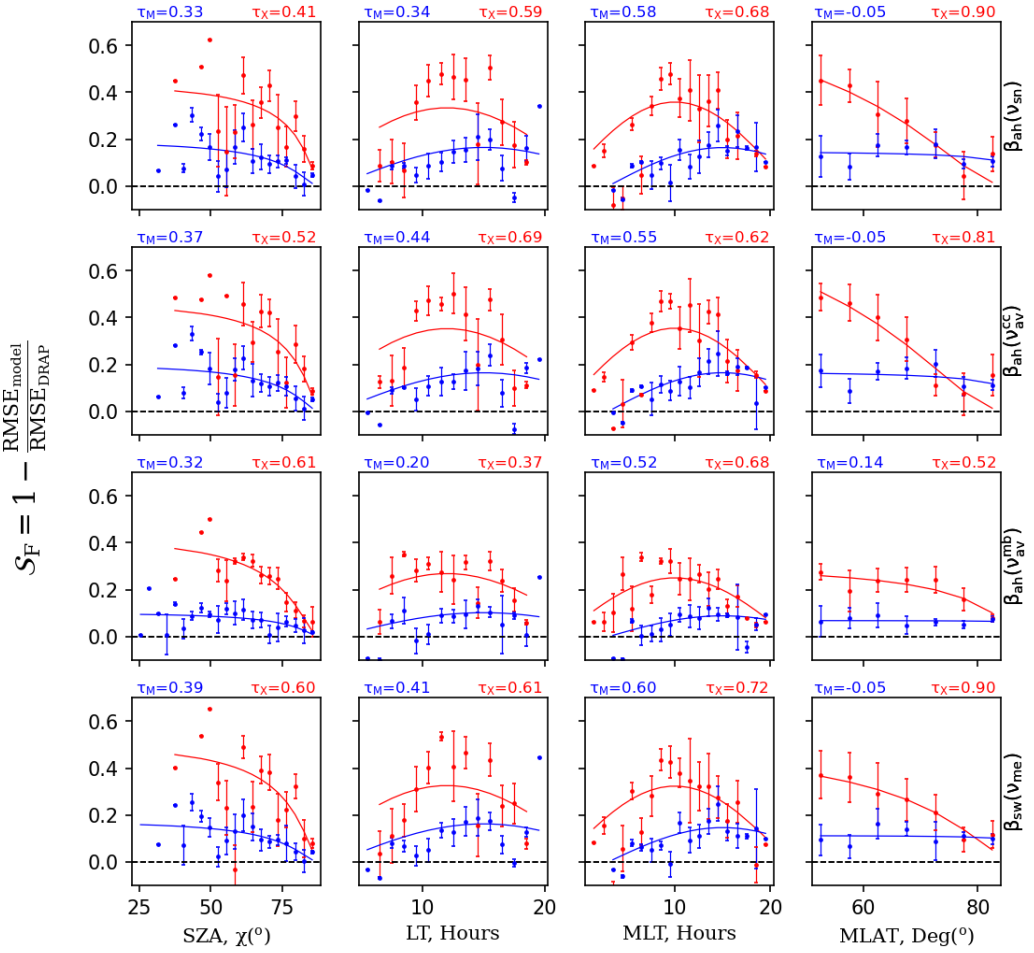

Figure 5.7: Modeled forecast skill scores ($\mathcal{S}_F$) versus (left to right) solar zenith angle, local time, magnetic local time, and magnetic latitude. Each row corresponds to skill associated with the formulations listed in Table 5.2. Red and blue dots represents skill score associated with X and M class flares, respectively. Error bars associated with each data point represents the median absolute deviation. Red and blue solid curves represent best fit curves through the data for X and M-class flares, respectively. The correlation coefficients (τ_*) between the data and fitted curves are provided in the top corners of each panel. See Table 5.2 for an explanation of model notation.

gle (SZA, χ), local time (LT), magnetic local-time (MLT), and magnetic latitude (MLAT). A separate analysis is presented for the four formulations (listed in Table 5.2), $\beta_{ah}(\nu_{sn})$, $\beta_{ah}(\nu_{av}^{cc})$, $\beta_{ah}(\nu_{av}^{mb})$, and $\beta_{sw}(\nu_{me})$ in each row from top to bottom, respectively. Data presented in red and blue colors in each panel are the model skills against X and M-class flares,

respectively. The solid line represents the best fit curve through the data. The correlation coefficients (τ_*) between the observed and fitted skill scores are provided in the top corners of each panel. The correlation coefficients show the fitting quality is better for X-class flares with all four parameters. It can be seen that the skill scores for all four formulations have a negative correlation with SZA and MLAT. Model skill scores for all formulations maximize near local solar noon (∼12 LT) for X-class flares and in the afternoon sector (∼15 LT) for M-class flares. Note, some trends are pronounced while others are weak and less significant. On average all four formulations produced better forecasts across all LT, SZA, MLT, and MLAT than the DRAP model ($\mathcal{S}_F > 0$). The decreases in $\mathcal{S}_F$ with SZA and MLAT are most likely due to variations in background ionospheric conditions with solar zenith angle and magnetic latitudes. If so, this would suggest our model is more suitable for HF absorption estimations at lower and middle latitudes near solar noon. Conclusive verification of this dependence requires more riometer observations at middle and lower latitudes.

5.4.4 Effects of Signal Frequency and Electron Temperature

Among the many ionospheric parameters responsible for controlling HF absorption, electron density in the D-region is considered to be the primary factor for HF absorption. However, studies have suggested signal frequency, collision frequency, and electron temperature are also important [e.g. 12, 16, 49]. These parameters are all interrelated. For example, any change in electron temperature alters the collision frequency and associated HF absorption experienced by the traveling radiowave [12]. In this section we examine how signal frequency and electron temperature impact HF absorption following a solar flare.

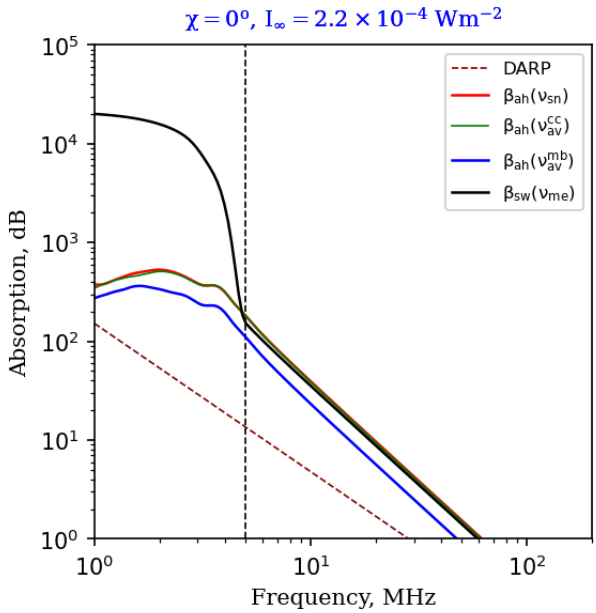

Figure 5.8: Impact of operating frequency on HF absorption for an X2.2 class flare estimated using the four different dispersion and collision frequency formulations (solid curves) and the DRAP model (dark red dashed curve). Black dashed vertical line represents 5 MHz signal frequency. See Table 5.2 for an explanation of model notation.

Effects of Signal Frequency

Figure 5.8 shows how HF absorption produced by an X2.2 class flare on 11 March 2015 depends on signal frequency for the DRAP model and the four formulations of our new model. The absorption is estimated for one-way vertical path O-mode transmission at the subsolar point (i.e. $\chi = 0^o$). It can be seen that the DRAP results are significantly lower than those estimated by all four formulations of our new model across the frequency range under consideration. Furthermore, all four formulations of our model show a nonlinear dependence on signal frequency below 5 MHz (denoted by the vertical black dashed line in Figure 5.8) while DRAP shows a linear dependence over the entire range of frequencies under consideration. Our model formulations indicate that absorption saturates for frequencies below 4 MHz.

Effects of Electron Temperature

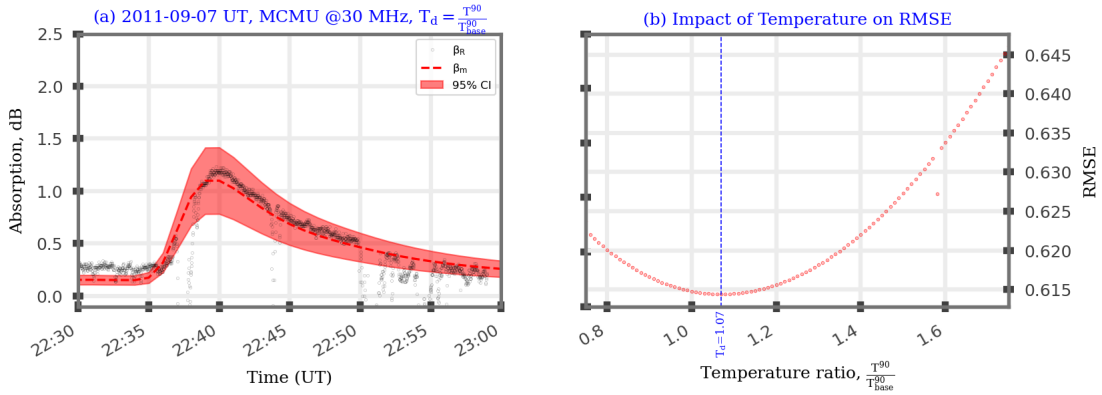

Figure 5.9: Impact of electron temperature on the estimation of HF absorption for the X-class solar flare event on 7 September 2011. (a) HF absorption observed by MCMU riometer station (black dots) and estimated using the Appleton-Hartree and the Schunk-Nagy formulations with 95% confidence interval (red shading). (b) Variation in RMSE with D-region electron temperature (red dots) with the minimum temperature ratio identified at 1.12 (blue dashed vertical line).

Figure 5.9 shows how HF absorption depends on electron temperature for modeling of the X-class solar flare on 7 September 2011. Panel (a) presents HF absorption observed by the MCMU riometer station (black dots) and estimated using the Appleton-Hartree dispersion relation and Schunk-Nagy collision frequency formulation (red dashed curve). The red shaded region represents a 95% confidence interval for the estimated absorption. Panel (b) presents the variation of RMSE with electron temperature ratio $T_d = \frac{T}{T_{init}}$, which represents the ratio of electron temperature to the background obtained from IRI-2016. For example $T_d = 1.2$ corresponds to an electron temperature that is 1.2 times of the background electron temperature from IRI-2016. The confidence interval of absorption presented in panel (a) was obtained by random sampling (bootstrapping [43]) over the electron temperature range showed in panel (b). It can be seen that the minimum RMSE corresponds to an electron temperature ratio $T_d = 1.07$ (blue dashed line) which produces the best results shown by the mean dashed red line in panel (a). This simplistic analysis suggests that one way to pro-

duce better model-data agreement is to increase the IRI electron temperature by 7% while keeping all other parameters fixed. However, the various parameters are interrelated and some of them will likely vary, perhaps significantly, if the temperature were to change by this full amount. Finally, it can be seen that the pre-flare absorption observations are underestimated by the model, suggesting the assumed background conditions of the ionosphere were inaccurate for this particular flare event.

5.5 Discussion

In this study we have presented a new HF absorption prediction model with four different dispersion relation and ion-neutral collision frequency formulations. We compared outputs from the four proposed formulations with the DRAP model and riometer observations (see Figures 5.4-5.5). We used skill score analysis to determine how the performance of the four model formulations vary with solar zenith angle, LT, MLT and MLAT (see Figures 5.6-5.7). We also examined how the model predictions of HF absorption vary with important controlling parameters, namely, frequency of the radiowave, plasma-neutral collision frequency, and electron temperature (Figures 5.8-5.9). We find that all four formulations listed in Table 5.2 are performing significantly better than the DRAP model. Among four models listed in Table 5.2 the Appleton-Hartree dispersion relation with averaged collision frequency (Chapman-Cowling integral) [$\beta_{ah}(\nu_{av}^{cc})$], the Appleton-Hartree dispersion relation with Schunk-Nagy collision frequency [$\beta_{ah}(\nu_{sn})$], and the Sen-Wyller Dispersion relation with mono-energetic collision frequency [$\beta_{sw}(\nu_{mb})$] are performing marginally better than the Appleton-Hartree dispersion relation with averaged collision frequency (Maxwellian-Boltzmann integral) [$\beta_{ah}(\nu_{av}^{mb})$]. In this section, we further discuss the significance of these results and compare them with previous studies.

The statistical study presented in Figures 5.6 and 5.7, reveals that the four formulations, listed in Table 5.2, showed a negative trend with solar zenith angle and MLAT. In addition, all four formulation had maximum skill scores near and after local solar noon for X and M-class flares, respectively. These statistical results suggest all four formulations listed in Table 5.2 generally do better than the DRAP model on the dayside (SZA$\leq 90^o$) for all magnetic latitudes with average skills scores $\bar{\mathcal{S}}_F \sim 0.4$, 0.39, 0.327, and 0.371, respectively. Also, our model performs better for X-class flares over M-class flares. This suggests that we can use all four formulations to estimate solar flare-driven HF absorption. In a recent study, Heino et al. [65] found that the Sen-Wyller dispersion relation overestimates riometer observations for subauroral latitudes for Auroral Absorption (AA) and Polarcap Absorption (PCA) events; however, with higher magnetic latitudes, the error decreases. Our findings for solar flare-driven absorption shows skill scores for all formulations drops with MLAT, which is in contrast with the observation from Heino et al. [65]. Kero et al. [73] also reported that the Sen-Wyller dispersion relation overestimates riometer observation at most by 7 dB. Kero et al. [73] suggests that the discrepancy in estimation might come from one of the following reasons: (1) invalid D region assumptions by the Sen-Wyller theory, or (2) additional electron loss processes which are not accounted for in the model. In contrast, Zawdie et al. [162] suggested both the Appleton-Hartree and Sen-Wyller dispersion relations are appropriate for estimating HF absorption provided one uses the right collision frequency estimates. We suggest that all four formulations including the Sen-Wyller dispersion relation listed in Table 5.2 can be used to estimate solar flare-driven HF absorption as all four formulations . Clearly, further study is required to definitively determine which combinations of model formulations are most appropriate for various latitudinal regimes and geomagnetic conditions.

One of the major findings in the event analysis and statistical study is that DRAP underestimates the HF absorption throughout the HF spectrum ($\sim$ 1-30 MHz, refer to Figure

5.8). This is likely due to the narrow bandwidth of solar spectrum used as input by DRAP. Our model uses the EUVAC solar irradiance model [143] modified by the GOES SXR and HXR dataset to capture a wider spectral range of flare-time dynamics. In contrast, DRAP assumes SXR alone is a good proxy for solar flare dynamics and is solely responsible for producing enhancement in D-region ionization [5, 135]. In reality, the SXR, HXR and Lyman-α radiation controls D-region and lower ionospheric ionization, while the extreme ultraviolate (EUV) and other wavebands control E and F region ionization. During a solar flare the HXR and EUV wavebands can be significantly enhanced [126, 143] and the scaling factors vary with wavebands and flare type [125]. In a recent study, Berngardt et al. [17] found that their HF absorption model performs better when EUV emissions are used as an input. Clearly, a broader range of solar spectrum is required to accurately model flare-time ionospheric HF absorption.

In a partially ionized medium, free electrons are the carriers of the O-mode radiowave [39]. The plasma-neutral interaction can be parametrized by the collision frequency (ν), while both signal (f_0) and collision frequencies are significant factors for HF absorption (ν) [138, 139]. The amount of EM energy transferred to heat is controlled by the temperature of the electrons [39, 139]. Figures 5.8 and 5.9 show the impacts of radiowave frequency and electron temperature on HF absorption, respectively. From Figure 5.8, we observe DRAP does not produce saturation effects at the lower end ($\leq$ 5 MHz) of the HF spectrum. Most empirical models, including DRAP, use a power-law $f^{-p}, p \in \mathbb{R}$ relation with signal frequency [e.g. 137]. One limitation of this relationship is it assumes the dispersion effect of radiowaves is similar across all frequencies. In reality, a dispersive magneto-ionic medium, such as the ionosphere has complicated dependencies on frequency [e.g. 139]. A study by Schumer [137] found the f^{-2} dependence of the SWPC model was inappropriate and the accuracy of the DRAP model degraded with increasing signal frequency. Improving the accuracy of

empirical models of HF absorption requires incorporation of plasma-neutral interactions at all frequencies of the HF spectrum.

Another focus of this paper has been to study the impact of electron temperature on HF absorption. The electron temperature is important because it controls the plasma-neutral interaction and the collision frequency [e.g. 49, 138, 139]. Specifically, the electron collision frequency is a strong function of temperature, which is known to vary as a function of time of day, season, solar activity, and latitude [162]. Zawdie et al. [162] argued that although most variability in electron collision frequency occurs above 150 km altitude, a small change in collision frequency at D-region heights can significantly affect HF absorption. Bajčetić et al. [12] showed that flare-driven D-region temperature changes also alter recombination rates in the D region and thus increases the recovery time of SWF. This suggests that a small change in D-region electron temperature can impact the HF absorption significantly. An in-depth analysis of the change in flare-driven ionospheric electron temperature and its impacts on HF absorption will be a focus of future study.

5.6 Conclusion & Future Study

In this study, we have proposed a new framework for estimating solar flare-driven HF absorption. We found that HF absorption has a strong dependence, collision frequency, and electron temperature. The primary goal of this study has been to find which combination of dispersion relation and collision frequency model best reproduces riometer observations of HF absorption. In addition, we analyzed the impact of electron temperature on HF absorption. The primary findings are:

1. Our model performs significantly better than the DRAP model across all the dayside of the Earth and for all magnetic latitudes. Four formulations listed in Table 5.2

generally outperforms DRAP with average skill scores $\bar{\mathcal{S}_S} \sim 0.4$, 0.39, 0.327, and 0.371, respectively.

2. Among the four formulations listed in Table 5.2 the following three formulations do marginally better: (a) the Appleton-Hartree dispersion relation with average collision frequency (Chapman-Cowling Integral) $[\beta_{ah}(\nu_{av}^{cc})]$, the Appleton-Hartree dispersion relation with Schunk-Nagy collision frequency $[\beta_{ah}(\nu_{sn})]$, and the Sen-Wyller dispersion relation with mono-energetic collision frequency $[\beta_{sn}(\nu_{me})]$

3. A broad range of solar irradiance wavebands is required to improve the forecasting of flare-time ionospheric HF absorption. By introducing additional terms, empirical models can incorporate plasma-neutral interactions at all frequencies of the HF spectrum and improve HF absorption prediction.

4. Change in the D-region electron temperature plays an important role in HF absorption experienced by traveling radiowaves.

The results and conclusion in this study are based on the newly developed model framework that can not only be used to estimate HF absorption, but also be adopted to do HF radio-propagation analysis during solar flares.

We have demonstrated the ability with our model to substantially reproduce riometer observations of HF absorption by applying various combinations of modeling inputs that include a dispersion relation formulation, a collision frequency formulation, and a temperature profile. In future studies, we plan to conduct sensitivity analyses to elucidate the impact of variability in the modeling inputs on model predictions and to gain physical insight into ionospheric physics.

Acknowledgments

SC also thanks to the National Science Foundation and the NASA for support under grant AGS-1935110 and 80NSSC20K1380, respectively. We acknowledge the use of the NOAA/-GOES X-ray data (from https://satdat.ngdc.noaa.gov/sem/goes/data/) for flare confirmation, analysis, and use as model inputs. We thank NRCan for providing the riometer data and the University of Calgary for providing riometer data directly via http://data.phys.ucalgary.ca/. The authors acknowledge Advanced Research Computing at Virginia Tech for providing computational resources and technical support that have contributed to the results reported within this paper (https://198.82.212.30). The majority of analysis and visualization was completed with the help of free, open-source software tools such as matplotlib [68], IPython [118], pandas (McKinney, 2010), Spacepy [107], PyForecastTools [108], and others [e.g. 102].

Chapter 6

The Role of Flare-Driven Ionospheric Electron Density Changes on the Doppler Flash Observed by SuperDARN HF Radars

S. Chakraborty[1], L. Qian[2], J. M. Ruohoniemi[1], J. B. H. Baker[1], J. M. Mclnerney[2], N. Nishitani[3]

[1]Bradley Department of Electrical and Computer Engineering, Virginia Tech, Blacksburg, Virginia, USA

[2]National Center for Atmospheric Research, Boulder, CO, USA

[3]Institute for Space-Earth Environmental Research, Nagoya University, Nagoya 464–8601, Japan

Chakraborty, S., Qian, L., Ruohoniemi, J. M., Baker, J. B. H., & Mclnerney, J. M. (2021). Role of Flare-Driven Electron Density Change on Doppler Flash. JGR Space Physics, Under Review.

Abstract

Trans–ionospheric high frequency (HF: 3-30 MHz) signals experience strong attenuation following a solar flare-driven sudden ionospheric disturbance (SID). Solar flare-driven HF absorption, referred to as short-wave fadeout (SWF), is a well-known impact of SIDs, but the initial Doppler frequency shift phenomena, also known as "Doppler flash" in the traveling radiowave is not well understood. This study seeks to advance our understanding of the initial impacts of solar flare-driven SID using a physics-based whole atmosphere model for a specific solar flare event. First we demonstrate that the Doppler flash phenomenon observed by SuperDARN radars can be successfully reproduced using first-principles based modeling. The output from the simulation is validated against SuperDARN LoS Doppler velocity measurements. We then examine which region of the ionosphere, D, E, or F, makes the largest contribution to the Doppler flash. We also consider the relative contribution of change in refractive index through the ionospheric layers versus lowered reflection height. We find: (i) the model is able to reproduce radar observations with an RMdSE and a mean percentage error (MPE, δ) of 3.72 ms^{-1} and 0.67%, respectively; (ii) the F-region is the most significant contributor to the total Doppler flash ($\sim$48%), 30% of which is contributed by the change in F-region's refractive index, while the other $\sim$18% is due to change in ray reflection height. Our analysis shows lowering of the F-region's ray reflection point is a secondary driver compared to the change in refractive index.

Plain Language Summary

Sudden eruption of electromagnetic radiation from the Sun, also known as a solar flares, alters the physical properties of the ionosphere, creating ionospheric perturbations, commonly referred to as a sudden ionospheric disturbance (SID). The ionosphere perturbation following a solar flare disrupts the over the horizon radio communication channels on the dayside of the Earth, also known as shortwave fadeout (SWF). The ionospheric radiowave absorption

effect during a solar flare-driven SID is a well known and understood phenomena. However, the initial Doppler frequency shift, also known as "Doppler flash", in the traveling radiowave is a newly discovered phenomena and not yet fully understood. This paper seeks to advance our understanding of the initial impacts of solar flares on the ionospheric properties.

6.1 Introduction

A solar flare is a sudden intensification of the Sun's electromagnetic radiation, specifically in the EUV and X-ray wavebands of the solar spectrum, that lasts for a few tens of minutes to several hours [e.g. 60, 122, 142]. The intensification of solar electromagnetic radiation during a solar flare enhances the plasma density via photoionization in the dayside of the Earth's ionosphere that leads to sudden ionospheric disturbances (SIDs) [e.g. 39, 40]. SID affects trans-ionospheric high frequency (HF: 3-30 MHz) communication by disrupting the signal properties, namely, signal amplitude [e.g. 27, 39], frequency [75, 156], and phase [e.g. 74]. Disruption of HF signal amplitude following SIDs, is commonly referred to as shortwave fadeout (SWF) [e.g. 28, 47], while disruptions of signal frequency and phase are known as sudden frequency deviation (SFD) [e.g. 88] and sudden phase anomaly (SPA) [e.g. 74], respectively. Disruption of signal amplitude or shortwave fadeout (SWF) has been a topic of research for almost a century and has produced hundreds of publications. In contrast, the relatively newly discovered phenomenon of sudden frequency deviation (SFD) that occurs during the initial phase of SID is not well understood. The manifestation of SFD signature in HF radar observations is a sudden rise in the apparent Doppler velocity of the backscatter signal, commonly referred to as the "Doppler flash" Chakraborty et al. [27] showed that the Doppler flash is the earliest signature recorded by HF radar during a flare-driven SID event. A detailed study of Doppler flash can enable us to gain insight about the spatiotemporal evo-

lution of flare-driven HF absorption and unveil knowledge into ionospheric electrodynamics including ionospheric conductivity, the equatorial fountain effect, the equatorial electrojet [e.g. 148], and the S_q current systems [e.g. 38].

Historically, VLF receivers [e.g. 74], and ionosondes [e.g. 44] have been the primary instruments used to study SFDs. Incoherent scatter radar (ISR) [e.g. 100, 115], and Super Dual Auroral Radar Network (SuperDARN HF radars) [e.g. 47, 156] have been used to study solar flare-driven Doppler anomalies in the ionosphere. While ionosondes and VLF receivers provide information about ionospheric plasma density enhancement, the ISRs observes changes in a more complete set of ionospheric properties, namely, ionospheric temperature, plasma density, and ion-drift parameters. Some studies exploit data from ISRs and magnetometers to study changes in the ionospheric S_q current system [e.g. 6]. In comparison, SuperDARN radars observe a sudden rise in Doppler velocity in the backscatter signal, which can provide insights into propagation conditions in the ionosphere. Although SuperDARN HF radars are affected severely by radio-blackout during the peak of HF absorption [e.g. 27], they can be used to study the spatiotemporal evolution of the initial and recovery phases of SIDs.

Prior studies have suggested that the Doppler flash is caused by a sudden change in the phase path length of the travelling radiowaves [e.g. 75, 156]. Kikuchi et al. [75] suggested two possible sources that might contribute to the change in phase path length: first, change in refractive index due to the enhancement of plasma density in the non-deviative part of the ionosphere, i.e., D and lower E-regions; and second, change in the F-region ray reflection height. They postulated that change in the F-region ray reflection height is associated more with geomagnetic storms and travelling ionospheric disturbances while the change in refractive index of the non-deviative slab of the ionosphere is predominantly due to enhanced photoionization following a solar flare. In a statistical study, Watanabe and Nishitani [156] showed that the Doppler flash originating from a solar flare is predominately driven by

changes in the ionospheric refractive index. However, that study did not discuss which region of the ionosphere is primarily responsible for the Doppler flash phenomenon.

Clearly, we do not have a robust understanding of the sources and driving mechanisms of the flare-driven Doppler flash phenomenon. Observations and modeling efforts regarding the manifestation and evolution of the Doppler flash are very limited. Our primary objective in this study is to demonstrate that first-principles based modeling of HF signal propagation through the flare-modified ionosphere can reproduce radar observations. Next we apply the results to answer the following questions: (i) Is the Doppler Flash primarily a D and lower E-region phenomenon?; (ii) Does a solar flare impact the HF signal through the height change of the F-region?; and (iii) What drives the change in F-region ray reflection height? We present a comprehensive data-model analysis of the Doppler flash that follows an X-class solar flare. Specifically, we use the Flare Irradiance Spectrum Model (FISM) to capture flare-time changes in the solar spectrum and the Whole Atmosphere Community Climate Model with thermosphere and ionosphere extension (WACCM-X) to simulate the flare-enhanced electron density. We then use a ray-tracing model, Provision of High-Frequency Ray-tracing Laboratory for Propagation Studies (PHaRLAP), to geolocate HF rays. Finally we use the Doppler model described by Kikuchi et al. [75] to calculate the Doppler flash and compare it with the SuperDARN radar observations. This paper is organized as follows: Section 6.2 provides a brief introduction to the instruments and datasets used in the study; Section 6.3 describes different models used in this study; Section 6.4 presents model results, comparison of the model results with observations, and a statistical study examining sources of the Doppler flash; Section 6.5 provides discussion of the results in the context of similar work.

6.2 Instrumentation & Datasets

SuperDARN is a network of HF radars, operating between 8 and 18 MHz, distributed across the middle, high, and polar latitudes of both hemispheres. Each radar measures the line-of-sight (LoS) component of the $\vec{E} \times \vec{B}$ drift velocity of decameter-scale ionospheric plasma irregularities [e.g. 33, 57, 112]. The field-of-view (FoV) is typically comprises 16 to 20 azimuth beams and in 75-110 range gates spaced 45 km apart beginning in the 180 km range. Typical integration time of each beam sounding is 3s or 6s, which results in a full radar sweep through all beams in 1 or 2 minutes. Figure 1 shows the location of the SuperDARN Blackstone radar and its field-of-view (FoV).

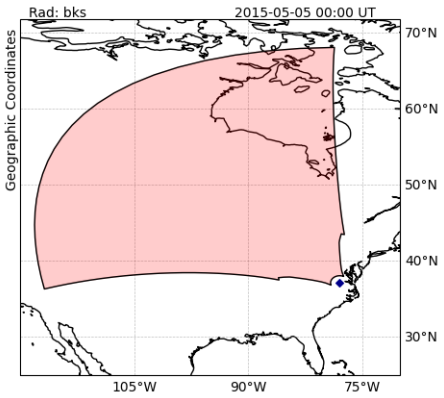

Figure 6.1: Field-of-view (FoV) of the SuperDARN Blackstone radar located at middle latitude used in this study.

SuperDARN observations primarily consist of two types of backscatter, namely, ionospheric scatter and ground scatter. Figure 2 presents an illustration of the generating mechanisms and an example of a Doppler velocity FoV plot of ground and ionospheric scatter data. In the case of ground scatter [corresponds to Ray (1) in Figure 2a], due to the high daytime vertical gradient in the refractive index, the rays bend toward the ground and are reflected from surface roughness and return to the radar following the same paths. This simulates a one-hop ground-to-ground communication link that passes through the D-region four times.

Ionospheric scatter [corresponds to Ray (2) of Figure 2a] is due to the reflection of the transmitted signal from ionospheric plasma irregularities. Typically, ground and ionospheric scatters are associated with relatively lower & higher Doppler velocities and narrower & wider spectral widths, respectively. Figure 2b presents a SuperDARN field-of-view Doppler velocity scan plot from the Blackstone radar showing ground scatter (in gray) and ionospheric scatter (color coded by Doppler velocity). Daytime SuperDARN observations typically consist of a band of ground scatter that extends over several hundred kilometers in range. The effects of solar flares can be easily identified as a sudden bite-out in the daytime ground scatter band and so we will only use the ground scatter observations in this study.

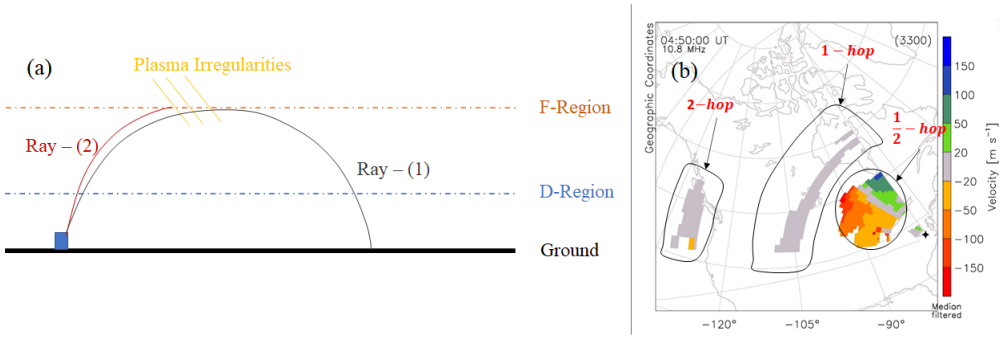

Figure 6.2: (a) Schematic plot of SuperDARN radar ray paths of ground scatter and ionospheric scatter, (b) SuperDARN field-of-view (FoV) scan plot, showing line-of-sight Doppler velocity measured by the Blackstone radar on 17 March 2015 at 4:50 UT. Velocity is color coded according to the scale on the right and ground scatter is marked gray. Different hops of scatter are identified and tagged by the enclosed regions and texts in red.

6.3 Models

In this section we describe the different models used to numerically estimate the Doppler flash. We used four models, namely FISM, WACCM-X, PHaRLAP ray-tracing, and Kikuchi's Doppler model. The FISM and WACCM-X models provide estimates of enhanced solar irradiance and ionospheric electron density following a solar flare. The PHaRLAP ray-tracing

model is used to geo-locate trans-ionospheric HF waves. Finally, we apply the Doppler theory described by Kikuchi et al. [75] to estimate Doppler frequency shifts experienced by the travelling HF radiowaves and the associated velocities measured by SuperDARN radars.

6.3.1 Flare Irradiance Spectral Model: FISM

The Flare Irradiance Spectral Model (FISM) is an empirical model that estimates the solar irradiance at wavelengths from 0.1 to 190 nm at 1 nm resolution with a time cadence of one day [32] and 60s [31]. FISM with time resolutions of one day and 60 seconds are referred to as the daily and flare component, respectively. The FISM flare component algorithm is parameterized by F10.7 and outputs 1-minute high resolution solar irradiance data. This high resolution data is used by ionospheric general circulation models to reproduce the flare time dynamics. FISM is built on Solar EUV Experiment (SEE) data, modified by the GOES 3 seconds data as a solar flare proxy. The FISM flare component predicts the solar irradiance variations from both the impulsive and gradual phases of solar flares. FISM outputs quantify the changes in solar irradiance that directly affect satellite drag and radio communications, as well as the accuracy in the Global Positioning System (GPS).

6.3.2 WACCM-X Model

Whole Atmosphere Community Climate Model with thermosphere and ionosphere extension or WACCM-X is WACCM with an extension into the thermosphere/ionosphere. WACCM is a whole atmosphere climate-chemistry general circulation model, with an upper boundary at $\sim$140 km [51, 96, 109]. It is a configuration of the NCAR Community Earth System Model (CESM) [69]. WACCM chemistry is based on the MOZART Model [76] (The Model for Ozone and Related Chemical Tracers), which includes all of the reactions that are known

to be important for the middle and upper atmosphere. In the mesosphere and lower thermosphere region, a radiative transfer algorithm for CO_2 is employed [48]. Detailed discussion of chemistry, radiative transfer, and other forcings such as volcanic aerosols are described in Marsh et al. [96].

WACCM-X has a $1.9^o \times 2.5^o$ horizontal resolution and a 0.25 scale height vertical resolution above 1 hPa (∼50 km), with an upper boundary at ∼600 km, depending on solar activity [86, 87]. The thermosphere/ionosphere extension adds a self-consistent ionosphere module that includes computation of electron and ion temperatures, self-consistent solution of global electrodynamics including an interactive electric wind dynamo at mid- and low-latitudes, and O^+ transport in the ionospheric F-region. At high latitudes, the electric field of magnetospheric origin is parameterized according to Heelis et al. [64] or Weimer [157], or provided by the Assimilative Mapping Ionospheric Electrodynamics (AMIE) procedure [92, 128]. Default solar ultraviolet irradiance is parameterized by F10.7 index, or supplied by measurements [143]. To capture flare time solar irradiance variations, WACCM-X uses solar irradiance information from the FISM. Details of the model are described in Liu et al. [87] and Liu et al. [90]. Additional validation and recent studies using this model can be found in Liu et al. [90], Pedatella et al. [114], Qian et al. [121], and Solomon et al. [144, 145].

6.3.3 PHaRLAP: HF Ray-tracing Model

To geolocate the HF rays in the ionosphere we have used the PHaRLAP ray tracing model [24]. PHaRLAP implements a variety of ray tracing engines of varying sophistication from 2D ray tracing to full 3D magnetoionic ray tracing. The 2D and 3D ray tracing modules are the implementations of the 2D equations developed by Coleman [36, 37] and Haselgrove [62] equations. In the case of 2D ray tracing the model takes ionospheric parameters, HF

ray properties, elevation and bearing angle of the ray as inputs and produces height and ground-range of the traveling HF ray in km as output. The 3D ray tracing module produces height, latitude, and longitude of the traveling HF ray as output. We used the 2D ray tracing module to geolocate rays along each individual beam of the SuperDARN Blackstone radar.

6.3.4 Kikuchi's Doppler Flash Model

Kikuchi et al. [75] suggests that the following drivers are the main sources of the change in phase path length that are associated with the Doppler flash: (a) change in refractive index of the non-deviative slab of the ionosphere following a solar flare, and(or) (b) change in ray reflection height following a geomagnetic storm. Figure 6.3 presents an illustration of how these two drivers reduce the phase path length of the traveling radiowave. In case (a) shown in Figure 6.3(a), Kikuchi's model assumes that the change in refractive index (η) is caused by increased ionization in the non-deviative slab with a thickness of d (D and lower E-region), electron density n_e, and ray incident angle α. The Doppler frequency shift due to the change in refractive index is mathematically described by equation (6.1). We have the numerical capability to estimate the change in refractive index (η) along the ray path. Figure 6.3(b) presents case (b) of Kikuchi's Doppler model, where ϕ_0 is the angle of the incident ray and Δh is the change in reflection height. Equation (6.2) provides the amount of Doppler frequency shift due to the change in ray reflection height.

$$\Delta f_{d\eta} = \frac{k}{cf}\frac{dn_e}{dt}\frac{d}{\cos\alpha} \tag{6.1}$$

$$\Delta f_{dh} = \frac{2f}{c}\frac{dh}{dt}\cos\phi_0 \tag{6.2}$$

$$\Delta v = 2c \times \frac{\sum \Delta f_*}{f} \tag{6.3}$$

where: c, h, ϕ_0, η, n_e, k =, α, and f are the speed of light, height of the reflecting layer, incident angle at the reflecting layer, refractive index, electron density, incident angle at each height interval, and signal frequency, respectively. The Δf_* and Δv in equation (6.3) are the change in signal frequency resulting from change in ionospheric refractive index or from change in the F-region ray reflection height and total Doppler velocity observed by the radar, respectively.

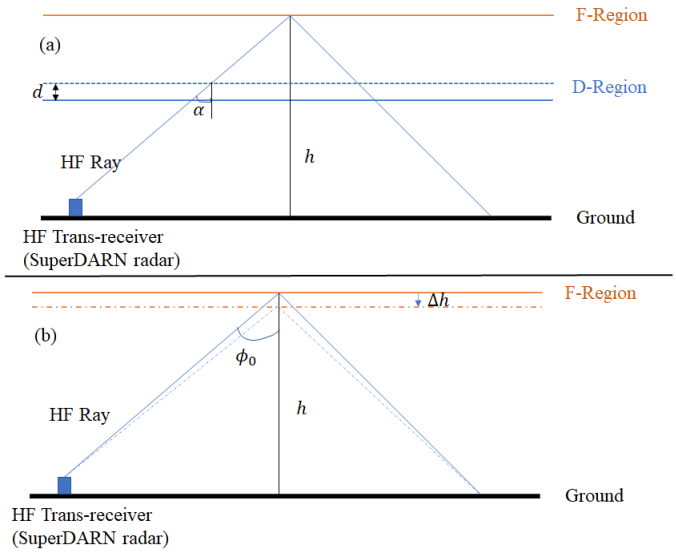

Figure 6.3: Illustration of two sources of Doppler shifts in the HF signal (Adopted from Kikuchi et al. [75]). Change in phase path length due to: (a) the change in refractive index (due to the enhanced electron density) in the non-deviative part of the ionosphere below the reflecting F-region and (b) the lowering of the F-region ray reflection height.

6.4 Results

In this section, we present a classic example of a Doppler flash event observed by the Blackstone radar in response to an X class solar flare (X2.7) on 5 May 2015 at 22:11 UT. Then, we provide simulated Doppler flash output from the model and compare it with radar observations. Finally, we present a statistical study of Doppler flash signatures observed by the Blackstone radar based on the model simulation. We will examine the relative contributions by the three ionospheric regions, D, E, and F, to the total Doppler flash. In addition, we analyze the influence of refractive index versus lowering of the reflection height on the Doppler flash.

6.4.1 Event Study: The Doppler Flash on 5 May 2015

On 5 May 2015 an X2.7 class solar flare erupted from the solar active region 2339. The flare started, reached its peak, and ended at 22:05 UT, 22:11 UT, and $\sim$ 22:25 UT, respectively. The maximum K_p value on this UT day was 2^+, thus we conclude the background geomagnetic conditions during this flare were mild and thus suitable to study the solar flare effects on the ionosphere [27]. We have selected this event as an exemplar to showcase the X-class flare-driven Doppler flash phenomenon.

Figure 6.4 presents images of the SWF event seen by the SuperDARN Blackstone radar. The upper nine panels (Figure 6.4(a)[i-ix]) present a series of field-of-view scan plots of line-of-sight Doppler velocity at 4-minute cadence, while the bottom panel (Figure 6.4(b)) shows a range-time plot of line-of-sight Doppler velocity for all beams. Panel 6.4(a)[iv] shows a complete wipeout of backscatter signal at 22:12 UT, consistent with the HF absorption phase of SWF, while Figure 6.4(b) shows that the SWF phenomenon lasted on the order of tens of minutes. The radio blackout event was preceded by a sudden enhancement of

apparent backscatter Doppler velocity at 22:08 UT (panel 6.4(a)[iii]), which is also evident in Figure 6.4(b). This feature is referred to as the Doppler flash [27]. The observations indicate a slight negative Doppler velocity during the recovery phase of the event. The location of the ground scatter band is not significantly perturbed during the Doppler flash so we can conclude that the geometry of the ray path is not greatly affected by the solar flare-driven SID.

6.4.2 Data-Model Comparison

This subsection describes the model outputs and compares them with the SuperDARN Blackstone radar observations. Figure 6.5 presents a data-model comparison for the SuperDARN Blackstone radar at the peak of the Doppler flash (5 May 2015, 22:08 UT). The left and right panels show Doppler velocity estimated using the model and observations from the Blackstone radar, respectively. Velocity is color-coded by the color-bar on the right. To compare the modeled output against the observations we have used two difference metrics, root-median-squared-error (RMdSE) and mean percentage error (MPE, δ). The RMdSE represents the square root of medianed squared differences between predicted and observed values. The MPE represents the mean of the ratio taken between the difference in observation and modeled values and the observation. The RMdSE and MPE for this case are provided in the right panel of the figure. Note that as radar observations are affected by the initial phase of the SWF, the radar did not receive backscattered echoes for all the range-cells uniformly. Hence, to estimate RMdSE and MPE we only consider range-cells with valid observations. The region enclosed by the red dashed lines represents beam 7 of the radar. The model is able to replicate the radar observations during the peak of the Doppler flash with an RMdSE of 4.51 ms^{-1} and a MPE (δ) of 1.43%. Next we will use one beam (beam 7 indicated by the red dashed line in Figure 6.5) to do a comprehensive data-model

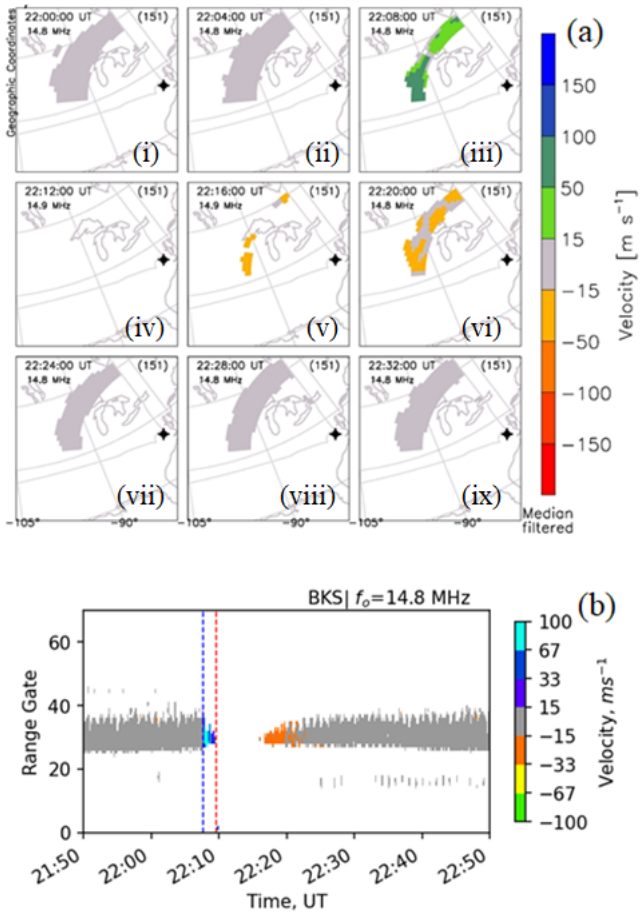

[!ht]

Figure 6.4: Response of the SuperDARN Blackstone radar to a solar flare on 5 May 2015: (a)[i-ix] Series of field-of-view (FoV) scan plots showing line-of-sight (LoS) Doppler velocity color coded according to the scale on the right and (b) Range-Time-Interval (RTI) plot showing backscattered Doppler velocity from all beams, color coded according to the scale on the right. Blue and red vertical lines represent the start of the Doppler flash and start of the radio blackout, respectively.

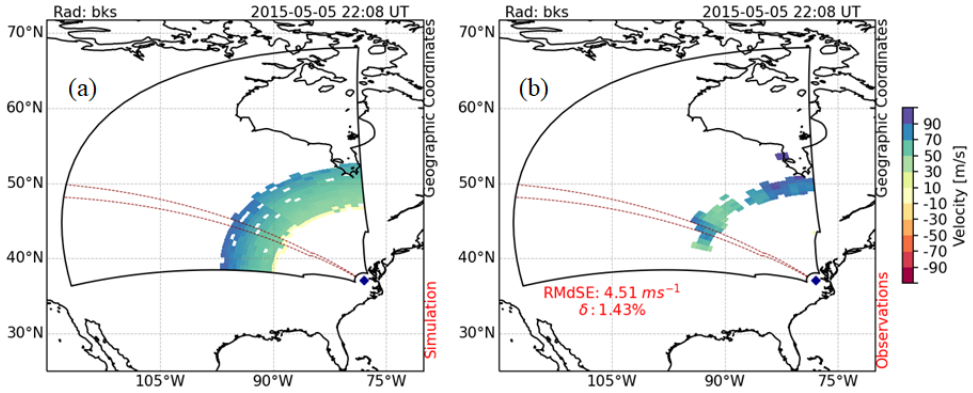

[!ht]

Figure 6.5: Data-model comparison for SuperDARN Blackstone radar measurements at the peak of the Doppler flash (22:08 UT). FoV scan plots showing: (a) Doppler velocity simulated using the model and (b) observations from the Blackstone radar. Doppler velocity is color coded according to the scale on the right. Root-median-squared-error (RMdSE) and mean percentage error (MPE, δ) between modeled and observed Doppler velocity is provided in panel (b). The region enclosed by the red dashed lines represents beam 7 of the radar.

comparison.

Figure 6.6 presents the data-model comparison from beam 7 of the SuperDARN Blackstone radar observations for the 1-hour time interval 21:51-22:52 UT. Panels (a) and (b) present modeled Doppler velocity contributed by the change in refractive index and change in the ray reflection height, respectively. The bottom panel (c) presents total Doppler velocity estimated using the model. The red dots in panel (c) are observations from beam 7 of the SuperDARN Blackstone radar. Error bars in all panels represent variations of Doppler velocity along beam 7. Similar to the previous comparison, we used RMdSE and MPE to validate our model predictions against the radar observations along beam 7. The radar observations are severely affected by the blackout (peak of HF absorption [27]) during 22:10-22:17 UT, and thus the observations suffer from the bite-out effects of the SWF. The comparison metrics are estimated based on the available data points. The analysis indicates that the model is able to replicate velocity observations during pre-flare, at the peak of the Doppler flash, and post-flare with an RMdSE of 3.72 ms^{-1} and an MPE of 0.67%. From the data-model

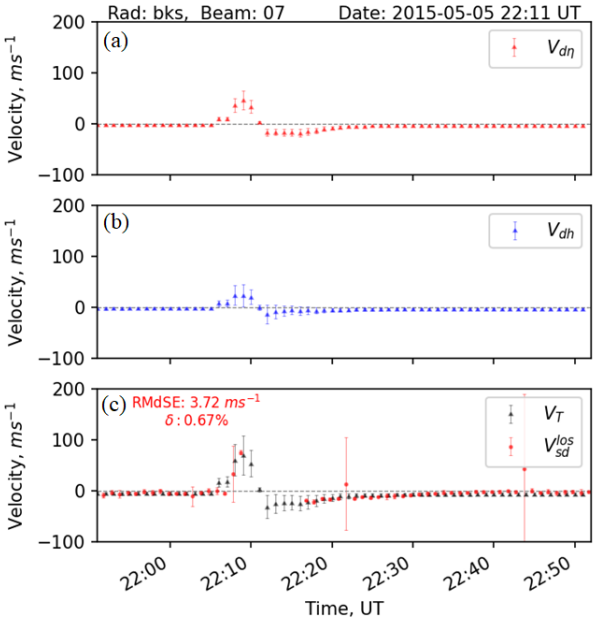

[!ht]

Figure 6.6: Time series plot of data-model comparison along beam 7 (region enclosed by the red dashed lines in Figure 6.5) of the SuperDARN Blackstone radar: (a) modeled Doppler velocity due to the change in refractive index , (b) modeled Doppler velocity due to the change in ray reflection height, and (c) total Doppler velocity. The red dots in panel (c) are observations from the SuperDARN Blackstone radar along beam 7. Error bars in all panels present the variation of Doppler velocity along beam 7. Root-median-squared-error (RMdSE) and MPE between modeled and observed Doppler velocity are provided in panel (c). Outliers are characterized by the large uncertainty values indicated by the vertical red lines.

comparison in Figures 6.5 and 6.6 we conclude that the modeling framework, described in Section 6.3, can reproduce the Doppler phase shift experienced by a traveling radiowave through the modeled ionosphere reasonably accurately. Therefore, we can analyze the model outputs to gain insight into the driving mechanisms of Doppler flash.

To compare the evolution of ionospheric conditions following the solar flare, Figure 6.7 presents ionospheric electron density and propagation conditions along beam 7 of the Blackstone SuperDARN radar. As flare-driven photoionization produces large perturbations in the ionospheric electron density, we prefer to use electron density subtracted from the previous time instance, referred to as differential electron density ($\Delta n_e = n_e^{(t)} - n_e^{(t-1)}$), to better characterize ionospheric conditions. Top, middle, and bottom panels of Figure 6.7 present differential electron density, modeled Doppler velocity due to the change in refractive index, and modeled Doppler velocity due to the change in ray reflection height, respectively. The Doppler velocity estimation is done using equations (6.1)-(6.3). Small popup panels at the bottom of the figure present the zoomed-in version of the rays presented in the panels (c-1∼2). Left and right columns present simulation results before (22:03 UT) and during the solar flare (22:09 UT), respectively. Horizontal blue, orange, and red lines passing through panels (b) and (c) represent approximate lower boundaries of the D, E and F-regions, respectively. The blue dotted rays in panels (c-1∼2) and (c-1∼2:i) represent rays from the previous time step (t_{i-1}). The zoomed-in panels are added to provide a close-up look to compare the lowering of the F-region reflection height during pre-flare and flare times. The modeled result shows solar flare-driven electron density enhancement is predominantly in the E and F-regions.

The simulation results presented in Figure 6.7 indicate that the rise in Doppler velocity is due to a decrease in refractive index as well as to a lowering of the ray reflection height. By analyzing the pre-flare and flare-time propagation conditions, we find the following: during

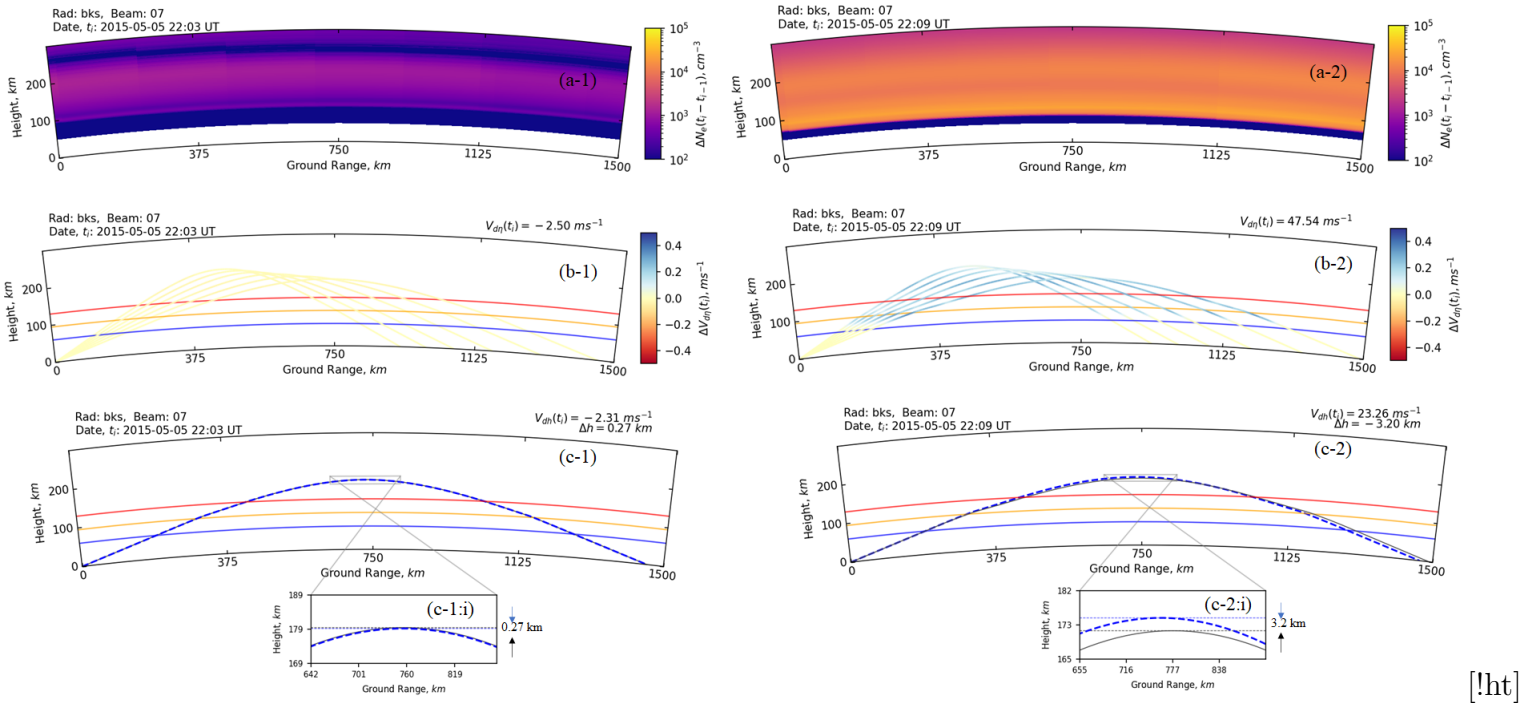

[!ht]

Figure 6.7: Change in the ionospheric electron density and the HF propagation condition along beam 7 of the SuperDARN Blackstone radar simulated using the model, before (at 22:03 UT) and during (at 22:09 UT) the solar flare on 5 May 2015: (a-1∼2) differential electron density (in cm^{-3}) simulated using the WACCM-X model color coded according to the scale on the right, (b-1∼2) modeled Doppler velocity along the transmitted rays due to the change in refractive index (in ms^{-1}) color coded according to the scale on the right, (c-1∼2) modeled Doppler velocity due to the change in ray reflection height (in ms^{-1}), and (c-1∼2:i) zoomed-in version of panel (c-1∼2) to show the drop in the F-region ray reflection point. Left and right columns present before and peak of the Doppler flash event. Dotted rays in panels (c-1∼2) and (c-1∼2:i) are the rays from the previous time stamp (t_{i-1}). Horizontal blue, orange, and red lines in panels (b) and (c) represent approximate lower boundaries of the D, E, and F-regions, respectively. Median Doppler velocity due to the change in refractive index and lowering of the F-region ray reflection height are provided in the top right corners of panels (b), and (c), respectively.

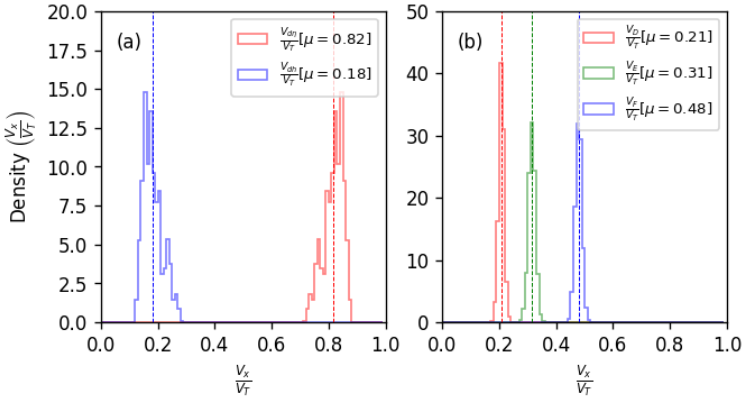

[!ht]

Figure 6.8: Histograms of (a) percentage of Doppler velocity contributed by the change in refractive index (in red) and change in ray reflection height (in blue), (b) percentage of Doppler velocity contributed by the D, E, and F-regions in red, green, and blue. Mean (μ) for each population is provided in the legend.

the solar flare (a) there is a significant enhancement in absolute electron density in the upper F and E-regions (deviative part of the ionosphere); (b) the change in Doppler velocity along the ray path due to change in refractive index is predominantly observed in the F and E-regions; and (iii) the drop in ray reflection height is almost 3.2 km (refer to panel c-2:i) which is ∼12 times greater than the pre-flare condition that is 0.27 km (refer to panel c-1:i) which is caused by the background change in the ionospheric propagation condition. The simulation also suggests that, on average, relative contributions to the Doppler flash along beam 7 from the change in refractive index and lowering the F-region reflection height are $\frac{2}{3}$ and $\frac{1}{3}$, respectively. In addition, we found relative contributions to the Doppler flash from the D, E, and F-regions are ∼20%, ∼30%, and ∼50%, respectively. By analyzing the simulation results along beam 7 of the SuperDARN Blackstone radar, we found that both the change in refractive index and change in the ray reflection height contribute to the solar flare-driven Doppler flash. However, the change in refractive index is the dominant among the two factors under consideration. The simulation also shows that the F-region is the primary contributor to the Doppler flash.

To demonstrate further that the change in refractive index is the major driver and the F-region is the primary contributor to the Doppler flash, we conducted a statistical study based on the simulation results from all beams of the SuperDARN Blackstone radar. The estimations of percentage contributions by the ionospheric layers or the two factors to the Doppler flash mentioned in the previous paragraph use modeled values averaged along one beam of the Blackstone radar during the peak of the Doppler flash. In this statistical analysis we use simulated data for all beams (0-23), with different elevation angles ($20^o - 35^o$), and during the whole period of Doppler flash observed by the radar ($\sim$ 22:07-22:09 UT), which gives $\sim$1080 simulated data points. Figure 6.8(a) presents histograms of relative contributions of the Doppler flash due to the change in refractive index (in red) and the change in ray reflection height (in blue). Figure 6.8(b) presents histograms of relative contributions of the Doppler flash by the D, E and F-regions in red, green and blue, respectively. Colored vertical dashed lines in both the panels represent the mean (μ) of each population. From the statistical analysis, we found that, on average, (i) relative contributions to the Doppler flash from the change in refractive index and change in the ray reflection height are $\sim$82% and $\sim$18%, respectively; and (ii) relative contributions of D, E and F-regions are $\sim$21%, $\sim$31%, and $\sim$48%, respectively. As HF rays are reflected at the F-region heights, therefore, among the total contribution by the F-region, $\sim$18% is due to the change in ray reflection height and $\sim$30% is due to the change in refractive index.

6.4.3 Vertical Ion-Drift and the Change of the Ray Reflection Height

Prior studies have suggested that enhanced electron density due to photoionization caused by flare-increased EUVs and X-rays is a source of change in the ionospheric refractive index, which is the primary driver of the Doppler flash [75, 156]. However, change in reflection

height may also play a role. In a recent study, Chum et al. [35] provided a mathematical construct of the Doppler frequency shift (f_D) observed by a normally incident radiowave:

$$f_D = -2.\frac{f}{c}\left(\int_0^h \frac{\partial \eta}{\partial n_e}\frac{\partial n_e}{\partial t}.dr\right) \tag{6.4}$$

where: c, η, n_e, h, f are the speed of light, real part of the refractive index, electron density, ray reflection height, and frequency of the radiowave, respectively. The term $\frac{\partial n_e}{\partial t}$ indicates change in electron density, which can be contributed by various sources and can be decomposed using the equation of continuity as [88]:

$$\frac{\partial n_e}{\partial t} = -\nabla n_e.w_I - n_e(\nabla.w_I) + p - l \tag{6.5}$$

where: w_I, p, and l are vertical plasma-drift, electron production via photo ionization, and loss of free electrons. The first term of equation (6.5) corresponds to vertical transport of plasma (advection) driven via $\vec{E} \times \vec{B}$ drift motion [149], while the second term represents plasma compression and rarefaction [34]. During a solar flare the electron production rate in equation (6.5) is predominantly controlled by photoionization, but we suggest vertical plasma-drift effect also contributes to the flare-driven Doppler flash via lowering the ray reflection height. We next present arguments and simulation results that support this contention.

Vertical ion-drift of the plasma is typically generated by the $\vec{E}_{zonal} \times \vec{B}_{meridional}$, where $\vec{E}_{zonal}$ and $\vec{B}_{meridional}$ are the east-west electric field and north-south magnetic field [127]. Typically, $\vec{B}_{meridional}$ in the mid-latitude northern hemisphere is northward directed and has a positive dip angle. In an observational study, Richmond et al. [127] showed that during the summer season at ~17 LT (22 UT), $\vec{E}_{zonal}$ is weak and eastward directed resulting in a northward ion-flow [see Figure 1 in 127]. Figure 6.9 presents the vertical ion-drift velocity

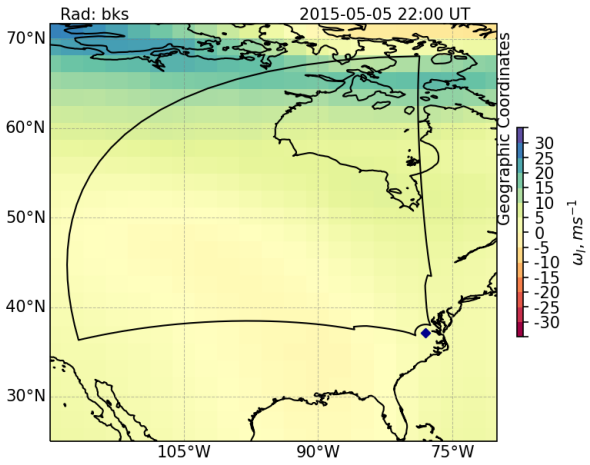

[!ht]

Figure 6.9: Vertical ion-drift velocity (ω_I) at 200 km altitude simulated using WACCM-X model before (at 22:00 UT) the solar flare on 5 May 2015. The velocity is color coded according to the scale on the right. The SuperDARN Blackstone radar's FoV is overlaid on top of the data.

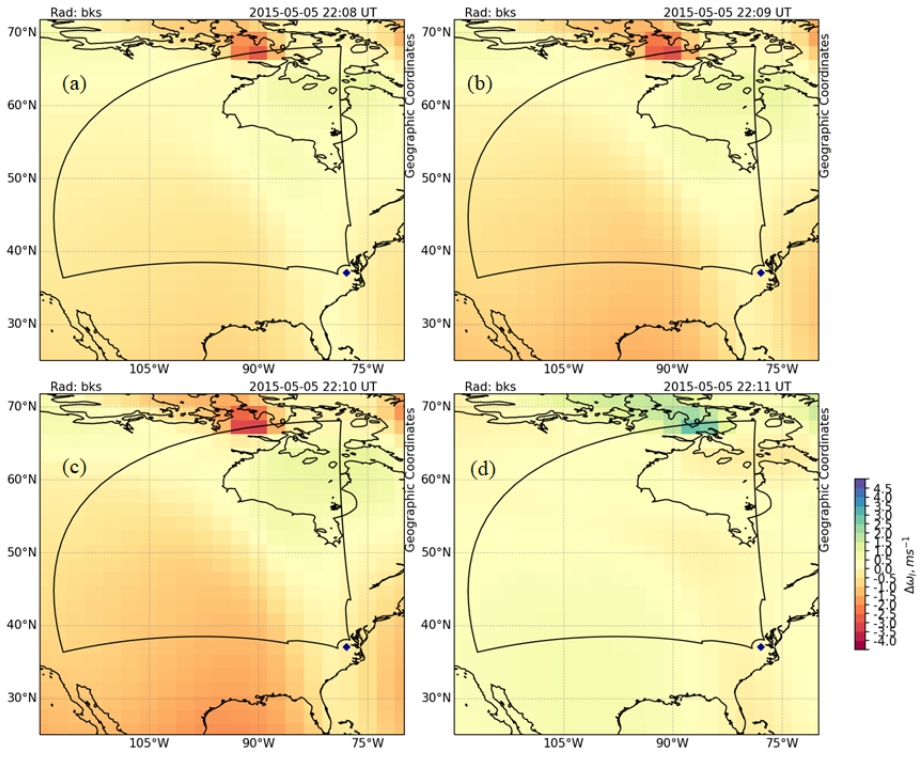

[!ht]

Figure 6.10: Differential vertical ion-drift velocity ($\Delta\omega_I$) from WACCM-X model at 200 km altitude during different phases of the flare evolution: (a) 22:08 UT, (b) 22:09 UT, (c) 22:10 UT, and (d) 22:11 UT. The difference uses 22:00 UT as the reference time.

(ω_I) simulated using the WACCM-X model at an altitude of 200 km during pre-solar flare (at 22:00 UT) conditions. The simulation result shows a slight positive (upward) motion of vertical ion-drift across the field-of-view of the Blackstone radar. This is consistent with a background zonal electric field that is weak and uniform across the field-of-view of the radar.

To present the temporal evolution of vertical ion-drift during the initial phase of the flare-driven SID, Figure 6.10 presents the differential vertical ion-drift ($\Delta\omega_I$) at an altitude of 200 km. This is estimated by subtracting ω_I from the previous time stamp (t_{i-1}). The four panels of Figure 6.10 present differential vertical ion-drift velocity at 1-minute cadence starting from 22:08 UT. This result is consistent with the results presented in Qian et al. [120]. With intensification of solar flare intensity through the rising phase of the event, there is a weakening effect on the upward motion of the ions that reduces the upward flow of plasma, which leads to an increased plasma density and, consequently, an increased Doppler frequency shift. The accumulation of plasma due to increased photoionization and decreased vertical outflow creates suitable conditions to reflect rays at relatively lower heights during solar flares than during quiet times. This suggests a flare-driven SID alters the background ionospheric current system that can be observed in ground magnetometer data as magnetic crochet [122].

6.5 Discussion

This paper has presented a modeling framework to reproduce the Doppler flash observed by SuperDARN radars. The paper explains the drivers of the flare-driven Doppler flash phenomenon observed in SuperDARN radars using the model results. The study has presented model simulations of the Doppler flash observed by the SuperDARN Blackstone radar triggered by the solar flare on 5 May, 2015. We find that the framework is able to predict the

SuperDARN radar observations reasonably accurately, with an RMdSE of 3.72 ms^{-1} and an MPD of 0.67% (refer to Figure 6.5 and Figure 6.6). We explored the two competing hypotheses described in Kikuchi et al. [75] and argue which might be the primary driver of Doppler flash in this event. By comparing simulation outputs with observations, we found: (i) the change in ionospheric refractive index is the major driver of solar flare-driven Doppler flash, (ii) among all three ionospheric regions, the F-region makes the largest contribution to the Doppler flash, and (iii) lowering of the ray reflection height can be caused by increases in the flare-driven refractive index and weakening of the vertical ion-drift. In this section, we further discuss the significance of these results and compare them with previous studies.

Kikuchi et al. [75] first postulated a theory of the Doppler anomaly recorded in HF observations following solar flares and during geomagnetic storms. The study suggested two possible factors, manifested by two different geophysical phenomena: first, changes in refractive index of the non-deviative part of the ionosphere, the lower D and E-region, following a solar flare; second, changes in the F-region ray reflection height during a geomagnetic storm. In a more recent study, Watanabe and Nishitani [156] showed that the change in the ionospheric refractive index is the major driver of the flare-driven Doppler flash. That study used Doppler velocity observations from the SuperDARN Hokkaido radar to empirically validate their hypothesis. However, the study did not determine which region of the ionosphere is most responsible for the Doppler flash. We found, on average, the relative contributions from the change in ionospheric refractive index and the change in ray reflection height are ∼82% and ∼18%, respectively (refer to Figure 6.8). This indicates that the ionospheric refractive index is the major driver of the flare-driven Doppler flash, consistent with the conclusions of Watanabe and Nishitani [156] and Kikuchi et al. [75], respectively. In addition, statistical analysis suggests on average the F and E-regions contribute ∼48% and ∼31% of the flare-driven Doppler flash (refer to Figure 6.8), respectively. The relative

contribution due to the change in refractive index and the change in ray reflection height on the F-region are ∼30% and ∼18%, respectively. Taking all of these results together, we can say the change in refractive index in the E and F-region is the major driver of the Doppler flash.

Another focus of this study was to investigate the sources of change in ray reflection point in the F-region following a solar flare. To our knowledge only a handful of prior studies have delved into this question for flare-driven SIDs. We found there are two factors which drive the lowering of the ray reflection height, first, the production of electrons via photoionization, and second, the weakening of the ionospheric vertical plasma-drift. The flare-enhanced refractive index forces rays to refract further and as a result they do not reach as high compare to non-flare conditions. Sudden weakening of the ionospheric vertical ion-drift enhances plasma accumulation by reducing the vertical outflow of plasma at the F-region heights. A sudden reduction of vertical plasma motion at the low and middle latitude F-region could be driven by sudden change in the zonal electric field ($\vec{E}_{east}$) and(or) in the ionospheric conductivity [38, 91]. In a recent study by Liu et al. [91] showed that the reduction in the upward ion drifts at the lower and middle latitudes are partially associated with changes in the flare-driven enhancement of electron density in the E-region which alters ionospheric conductivities and associated ionospheric currents. This sudden modification of ionospheric currents leading to the magnetic crochet effect [122]. Our future work will conduct a statistical study to quantify the percentage contributions by different possible factors that lower the ray reflection height following a solar flare.

6.6 Conclusions

In this study, we have presented a physics-based ray-tracing model framework for estimating the Doppler flash observed by the SuperDARN Blackstone radar following an X-class solar flare. We used the modeling results to gain insight about the generating mechanisms of the Doppler flash. We compared the relative contributions of two possible drivers of Doppler flash and the relative influence of the D, E, and F-regions. By analyzing and comparing the modeled estimates against observations, we found:

1. The model is able to reproduce the Doppler flash observation with an RMdSE of 3.72 ms^{-1} and a MPE of 0.67%.

2. Change in refractive index is the major driver of the Doppler Flash (∼82%).

3. The refractive index contribution to the Doppler flash is predominantly an E and F-region phenomenon.

4. Among the D, E, and F-regions, the F-region is the major contributor to the Doppler flash (∼48% in total: ∼18% is due to change in ray reflection height and ∼30% is due to a change in refractive index).

5. The apparent downward movement of the ray reflection height in the F-region is related to the increase in ionospheric refractive index and weakening of the vertical ion-drift.

For our future work, we will conduct a comprehensive statistical analysis using more solar flare events including M-class flares to find out whether these results apply to other solar flares in general.

Acknowledgments

SC thanks to the HAO laboratory at NCAR for supporting the NCAR's Advanced Study

Program's Graduate Student (GVP) Fellowship. SC also thanks to the National Science Foundation and the NASA for support under grant AGS-1935110 and 80NSSC20K1380, respectively. This material is based upon work supported by the National Center for Atmospheric Research, which is a major facility sponsored by the National Science Foundation under Cooperative Agreement No. 1852977. Any opinions, findings and conclusions or recommendations expressed in this material do not necessarily reflect the views of the National Science Foundation. We would like to acknowledge the use of computational resources (doi:10.5065/D6RX99HX) at the NCAR-Wyoming Supercomputing Center provided by the National Science Foundation and the State of Wyoming, and supported by NCAR's Computational and Information Systems Laboratory for the WACCM-X simulations. We wish to acknowledge the use of the NOAA/GOES X-ray data (from https://satdat.ngdc.noaa.gov/sem/goes/data/) for flare confirmation, analysis, and use as model inputs. We thank all participants in the worldwide SuperDARN collaboration for the distribution of SuperDARN data via http://vt.superdarn.org/tiki-index.php?page=Data+Access. The authors acknowledge Advanced Research Computing at Virginia Tech for providing computational resources and technical support that have contributed to the results reported within this paper (https://198.82.212.30). The majority of analysis and visualization was completed with the help of free, open-source software tools such as matplotlib [68], IPython [118], pandas [97], PyForecastTools [108], and others [e.g. 102].

Chapter 7

Conclusions & Future Work

The primary objective of this research has been to gain a better understanding of various solar flare effects observed by HF instruments and their driving mechanisms. In Chapter 2, we statistically characterized the signature of solar flare-driven shortwave fadeout (SWF) in SuperDARN HF radar observations. We identified three distinct phases in the observations, namely, onset, blackout, and recovery with typical durations of 100 s, 10 min, and 42 min, respectively. We identified and characterized the Doppler flash feature and determined the functional dependencies of peak Doppler velocity on solar zenith angle, radiowave frequency, and solar irradiance. We found that the effects in the HF radar observations are mostly controlled by solar zenith angle and less by radar frequency and flare intensity, whereas peak Doppler velocity is mostly dependent on radar operating frequency. In addition, observations showed that the physical parameters investigated in this chapter are unable to influence the onset phase timing and duration across different radars.

In Chapter 3, we examined the ionospheric response to an event study of multiple solar flares, SEPs, and geomagnetic storms co-occurring during the September 2017 solar storm. We examined the nonlinear response of the ionosphere during successive solar flares occurring in quick succession and segregated the influences of three different kinds of radiowave absorption, namely, shortwave fadeout, PCA, and auroral absorption in SuperDARN observations. We found that successive solar flares extend the ionospheric relaxation time, and one possible explanation for this phenomenon might be the enhancement in D-region

electron temperature.

In Chapter 4, we identified an intrinsic property of the ionosphere, sluggishness, which is the initial time delay of the ionospheric response following a solar driver, here solar flares. Sluggishness can be understood as an inertial property of the ionosphere that manifests as a lag of the ionospheric response. We used three different methodologies to estimate ionospheric sluggishness from riometer and SuperDARN HF radar observations. A correlation analysis was conducted on the sluggishness estimated from the instruments with solar zenith angle, latitude, local time, and peak X-ray intensity. We found that ionospheric sluggishness is anti-correlated with zenith angle and solar X-ray radiation intensity. We showed that sluggishness, estimated using different instruments and techniques, minimizes at local solar noon and is inversely proportional to electron density. We also presented a simulation study to estimate the D-region's height integrated effective ionospheric recombination coefficient ($\bar{\alpha}_{\text{eff}}$) and described the physical basis of sluggishness from the perspective of photochemical reactions. We found that $\bar{\alpha}_{\text{eff}}$ varies by several orders of magnitude with peak solar flare intensity. The simulation result suggested that decrease in $\bar{\alpha}_{\text{eff}}$ with flare intensity is likely caused by the enhancements in electron density and enhancements in electron detachment rate due to the sudden rise of molecular vibrational and rotational energy under the influence of energetic EM radiation.

In Chapter 5, we proposed a physics-based model framework for estimating solar flare-driven HF absorption. We compared four different dispersion relation and collision frequency formulations for estimating HF absorption. The four formulations were: (1) the Appleton-Hartree dispersion relation with Schunk-Nagy collision frequency [$\beta_{ah}(\nu_{sn})$], (2) Appleton-Hartree dispersion relation with average collision frequency (Chapman-Cowling Integral) [$\beta_{ah}(\nu_{av}^{cc})$], (3) Appleton-Hartree dispersion relation with average collision frequency (Maxwellian-Boltzmann Integral) [$\beta_{ah}(\nu_{av}^{mb})$], and (4) Sen-Wyller dispersion relation with

mono-energetic collision frequency [$\beta_{sw}(\nu_{mb})$]. Simulated results from the new framework were compared with the DRAP model and validated against riometer observations. All four formulations outperform the DRAP model with average skill scores $\bar{\mathcal{S}}_F$ ∼0.4, 0.39, 0.327, and 0.371, respectively. Among the four formulations $\beta_{ah}(\nu_{av}^{cc})$, $\beta_{ah}(\nu_{sn})$, and $\beta_{sn}(\nu_{me})$ do marginally better. We showed that a broad range of solar irradiance wavebands is required to improve the forecasting of flare-time ionospheric HF absorption.

In Chapter 6, we presented a physics-based ray-tracing model framework for estimating the Doppler flash observed by the SuperDARN Blackstone radar following an X-class solar flare. We used the modeling results to gain insight about the generating mechanisms of the Doppler flash. We found, (1) the model is able to reproduce the Doppler flash observation with an RMdSE of 3.72 ms^{-1} and a MPE of 0.67%, (2) change in E and F region refractive index is the major driver of the Doppler flash (∼82%), and (3) the apparent downward movement of the ray reflection height in the F-region is related to the increase in ionospheric refractive index and weakening of the vertical ion-drift.

In summary, utilizing riometer and SuperDARN measurements in conjunction with a first-principal physics-based modeling framework, we characterized the solar flare effects on radiowave propagation and investigated the driving mechanisms of these flare effects. This study answers the questions raised in Section 1.9, and provides insights into the driving influences of increased HF absorption or shortwave fadeout, sudden ionospheric disturbance or Doppler flash, D-region chemistry, and ionospheric sluggishness. Through coordinated observations from space and ground-based HF instruments we identified the signatures of HF absorption, the Doppler flash, and ionospheric sluggishness in Chapter 2, 3, and 4. Finally, using simulation and modeling efforts we confirmed the driving mechanisms of ionospheric sluggishness, HF absorption, and Doppler flash in Chapter 4, 5, and 6, respectively. The research in this dissertation will likely lead to improved forecasting of HF absorption and

frequency deviation following solar flares.

Below we provide suggestions for future directions that one could take to make use of the research findings presented in this dissertation:

1. In the statistical characterization study presented in Chapter 2, we used only X-class solar flares to characterize the impact of solar flares in the ionosphere. However, M-class solar flares also create SIDs that leads to follow on questions such as, "Do M and C-class solar flares disrupt trans-ionospheric radiowaves?" and "Do M and C-class solar flares produce the Doppler flash?". We suggest carrying out a comprehensive statistical characterization of SuperDARN ground-scatter data to understand the signature of M and C-class flares in radar observations, and check the viability of using SuperDARN radars to monitor relatively less intense solar flare-effects on HF propagation conditions.

2. Changes in electron temperature alter D-region properties including the collision frequency and chemical composition, which impact HF absorption. In the case study and modeling study presented in Chapter 3 and 5, respectively, we showed that a small flare-driven change in D-region electron temperature can significantly impact ionospheric HF absorption. However, the precise role of electron temperature and collision frequency in the estimation of HF absorption is still poorly understood. The studies presented in these two chapters suggest different physical processes might drive HF absorption at higher latitudes, the source of which is also less understood. We therefore, suggest using a comprehensive first-principal based model, such as WACCM-X or TIME-GCM, to estimate changes in electron temperature and collision frequencies in the D-region region and compare to our findings. Such a modeling study might also provide explanations for the latitudinal variation of HF absorption.

3. We used data from HF instruments to measure height integrated ionospheric sluggishness and inferred characteristics of ionospheric sluggishness, which is microscopic in nature. Follow on work could use a coupled ionosphere-mesosphere chemistry model, such as WACCM-X or TIME-GCM to estimate ionospheric sluggishness and then validate it against the observations presented in Chapter 4. Such a modeling study would also enable us to answer follow on questions such as: (a) "What is the height variation of sluggishness?", (b) "Which chemical reaction(s) is(are) responsible for creating ionospheric sluggishness?", and (c) "How do solar flares alter the D-region chemistry?".

4. Flare-driven ionospheric effects and its impact on background electrodynamics (Sq, EEJ, fountain effects) are not well understood. We have used one case study analysis and model simulation in Chapter 6 to gain insight about the generating mechanisms of the Doppler flash. However, the results presented in this single case study needs to be validated against more events and modeling of those events. We therefore suggest a comprehensive modeling study on multiple solar flare events to statistically validate our findings. The study presented here argued the dominant driver was lowering of the F-region reflection height, however, to validate this postulate, comprehensively, we suggest a follow-up study be conducted using data from various other data sources, such as ionosondes and magnetometers.

5. Shortwave Fadeout (SWF) and Sudden Frequency Deviation (SFD) are the first space weather impacts to occur in the magnetosphere-ionosphere system in response to a solar flare. Insights obtained from this research can be used to develop a real-time monitoring capability to specify the occurrence of SWF and SFD in the ionosphere using a sub-network of SuperDARN HF radars. Extension of this research to implement a real-time radio blackout monitoring system "Specification and Modeling of Radio Blackout Following Solar Flare" has already been awarded from the NASA SWO2R

program. Our plan is to combine real-time observations from the North American suite of SuperDARN radars to specify in near real-time the occurrence of SWF. A display for space weather operators will be created that depicts the severity of blackout across the continent with a short-term forecast of how an event is expected to evolve. The HF absorption model framework described in Chapter 5 can also be used to predict ionospheric conditions following solar flares.

Results from this research have been published in Radio Science [27], Space Weather [28], Journal of Geophysical Research: Space Physics [26], and IEEE Xplore [29]. We have also submitted two papers related to studies presented in Chapter 5 and 6 to Radio Science and Journal of Geophysical Research: Space Physics, which are currently under review. One co-authored paper has been published in Space Weather [47]. The solar flare effects have been recognized to play an important role in disruption of ionospheric HF communication channel. The improved understanding of flare-driven sudden ionospheric disturbances developed in this dissertation is a step forward in improving future space weather forecasts, which is a critical active area of research that is directly relevant to the National Research Council's (NRC) most recent decadal survey "Solar and Space Physics, A Science for a Technological Society" and "2018 NASA Strategic Plan".

Bibliography

[1] *Kolmogorov–Smirnov Test*. Springer New York, New York, NY, 2008. ISBN 978-0-387-32833-1. doi: 10.1007/978-0-387-32833-1_214. URL https://doi.org/10.1007/978-0-387-32833-1_214.

[2] M. A. Abdu, P. A. B. Nogueira, J. R. Souza, I. S. Batista, S. L. G. Dutra, and J. H. A. Sobral. Equatorial electrojet responses to intense solar flares under geomagnetic disturbance time electric fields. *Journal of Geophysical Research: Space Physics*, 122(3):3570–3585, 2016. doi: 10.1002/2016JA023667. URL https://agupubs.onlinelibrary.wiley.com/doi/abs/10.1002/2016JA023667.

[3] E. L. Afraimovich. GPS Global Detection of the Ionospheric Response to Solar Flares. *Radio Science*, 35(6):1417–1424, 2000.

[4] E. L. Afraimovich. GPS global detection of the ionospheric response to solar flares. *Radio Science*, 35(6):1417–1424, 11 2000. ISSN 00486604. doi: 10.1029/2000RS002340. URL http://doi.wiley.com/10.1029/2000RS002340.

[5] R A Akmaev, M Codrescu, C Schulz, and E Nerney. D-RAP Model Validation: I. Scientific Report. Technical report, 2010. URL https://www.ngdc.noaa.gov/stp/drap/DRAP-V-Report1.pdf.

[6] Patrick Alken and Stefan Maus. Relationship between the ionospheric eastward electric field and the equatorial electrojet. *Geophysical Research Letters*, 37(4), 2010. doi: https://doi.org/10.1029/2009GL041989. URL https://agupubs.onlinelibrary.wiley.com/doi/abs/10.1029/2009GL041989.

[7] Hiroshi Amemiya and Yoshiharu Nakamura. Measurement of Negative Ions in the Lower Ionosphere (D-Layer) in the Polar Region. *Journal of geomagnetism and geoelectricity*, 48(4):391–401, 1996. doi: 10.5636/jgg.48.391.

[8] S. Ananthakrishnan, M.A. Abdu, and L.R. Piazza. D-Region Recombination Coefficients and the Short Wavelength X-Ray Flux during a Solar Flare. *Planetary and Space Science*, 21(3):367 – 375, 1973. ISSN 0032-0633. doi: https://doi.org/10.1016/0032-0633(73)90035-4. URL http://www.sciencedirect.com/science/article/pii/0032063373900354.

[9] Edward V. Appleton. A note on the "sluggishness" of the ionosphere. *Journal of Atmospheric and Terrestrial Physics*, 3(5):282 – 284, 1953. ISSN 0021-9169. doi: https://doi.org/10.1016/0021-9169(53)90129-9. URL http://www.sciencedirect.com/science/article/pii/0021916953901299.

[10] ARRL. 2017 hurricane season after-action report. retrieve from – http://www.arrl.org/files/file/Public%20Service/ARES/2017%20Hurricane%20Season%20AAR.pdf. 2017.

[11] Weihua Bai, Guangyuan Tan, Yueqiang Sun, Qifei Du, and Junming Xia. Error analysis on nmf2 predicted by iri-2016 model during geomagnetic quiet and storm periods. In *IGARSS 2019 - 2019 IEEE International Geoscience and Remote Sensing Symposium*, pages 1927–1930, 2019. doi: 10.1109/IGARSS.2019.8897816.

[12] Jovan Bajčetić, Aleksandra Nina, Vladimir M. Čadež, and Branislav M. Todorović. Ionospheric D-region temperature relaxation and its influences on radio signal propagation after solar X-flares occurrence. 5 2017. doi: 10.2298/TSCI141223084B. URL http://arxiv.org/abs/1705.07657http://dx.doi.org/10.2298/TSCI141223084B.

[13] J. R. Bartels. The standardized index, K_s and the planetary index, K_P. *IATME*, 97 (12b), 1949.

[14] Tamal Basak and Sandip K. Chakrabarti. Effective recombination coefficient and solar zenith angle effects on low-latitude d-region ionosphere evaluated from VLF signal amplitude and its time delay during x-ray solar flares. 348(2):315–326, 2013. ISSN 1572-946X. doi: 10.1007/s10509-013-1597-9. URL https://doi.org/10.1007/s10509-013-1597-9.

[15] M. Beharrell and F. Honary. A new method for deducing the effective collision frequency profile in the D-region. *Journal of Geophysical Research: Space Physics*, 113(A5):n/a–n/a, 5 2008. ISSN 01480227. doi: 10.1029/2007JA012650. URL http://doi.wiley.com/10.1029/2007JA012650.

[16] Robert F Benson. Electron Collision Frequency in the Ionospheric D Region. *Radio Science*, 68D(10), 1964.

[17] O. I. Berngardt, J. M. Ruohoniemi, J.-P. St-Maurice, A. Marchaudon, M. J. Kosch, A. S. Yukimatu, N. Nishitani, S. G. Shepherd, M. F. Marcucci, H. Hu, T. Nagatsuma, and M. Lester. Global Diagnostics of Ionospheric Absorption During X-Ray Solar Flares Based on 8- to 20-MHz Noise Measured by Over-the-Horizon Radars. *Space Weather*, 17(6):907–924, 6 2019. ISSN 1542-7390. doi: 10.1029/2018SW002130. URL https://onlinelibrary.wiley.com/doi/abs/10.1029/2018SW002130.

[18] O.I. Berngardt, J.M. Ruohoniemi, N. Nishitani, S.G. Shepherd, W.A. Bristow, and E.S. Miller. Attenuation of decameter wavelength sky noise during x-ray solar flares in 2013-2017 based on the observations of midlatitude hf radars. *Journal of Atmospheric and Solar-Terrestrial Physics*, 173:1 – 13, 2018. ISSN 1364-6826. doi: https://doi.org/10.

1016/j.jastp.2018.03.022. URL http://www.sciencedirect.com/science/article/pii/S1364682617305163.

[19] D. Bilitza, D. Altadill, V. Truhlik, V. Shubin, I. Galkin, B. Reinisch, and X. Huang. International reference ionosphere 2016: From ionospheric climate to real-time weather predictions. *Space Weather*, 15(2):418–429, 2017. doi: https://doi.org/10.1002/2016SW001593. URL https://agupubs.onlinelibrary.wiley.com/doi/abs/10.1002/2016SW001593.

[20] Emma C. Bland, Erkka Heino, Michael J. Kosch, and Noora Partamies. Superdarn radar-derived hf radio attenuation during the september 2017 solar proton events. *Space Weather*, 16(10):1455–1469, 2018. doi: https://doi.org/10.1029/2018SW001916. URL https://agupubs.onlinelibrary.wiley.com/doi/abs/10.1029/2018SW001916.

[21] David Brodrick, Steven Tingay, and Mark Wieringa. X-ray magnitude of the 4 november 2003 solar flare inferred from the ionospheric attenuation of the galactic radio background. *Journal of Geophysical Research: Space Physics*, 110(A9), 2005. doi: 10.1029/2004JA010960. URL https://agupubs.onlinelibrary.wiley.com/doi/abs/10.1029/2004JA010960.

[22] S. Browne, J. K. Hargreaves, and B. Honary. An imaging riometer for ionospheric studies. *Electronics and Communication Engineering Journal*, 7(5):209–217, 1995. ISSN 09540695. doi: 10.1049/ecej:19950505.

[23] R. K. Burton, R. L. McPherron, and C. T. Russell. An empirical relationship between interplanetary conditions and dst. *Journal of Geophysical Research*, 80(31):4204–4214, 1975. doi: 10.1029/JA080i031p04204. URL https://agupubs.onlinelibrary.wiley.com/doi/abs/10.1029/JA080i031p04204.

[24] M. A. Cervera and T. J. Harris. Modeling Ionospheric Disturbance Features in Quasi-Vertically incident Ionograms using 3-D Magnetoionic Ray Tracing and Atmospheric Gravity Waves. *Journal of Geophysical Research: Space Physics*, 119(1): 431–440, 2014. doi: https://doi.org/10.1002/2013JA019247. URL https://agupubs.onlinelibrary.wiley.com/doi/abs/10.1002/2013JA019247.

[25] Sandip K. Chakrabarti, Sudipta Sasmal, Suman Chakraborty, Tamal Basak, and Robert L. Tucker. Modeling D-region ionospheric response of the Great American TSE of August 21, 2017 from VLF signal perturbation. *Advances in Space Research*, 62(3):651–661, 8 2018. ISSN 0273-1177. doi: 10.1016/J.ASR.2018.05.006. URL https://www.sciencedirect.com/science/article/pii/S0273117718304022.

[26] S. Chakraborty, J. M. Ruohoniemi, J. B. H. Baker, R. A. D. Fiori, S. M. Bailey, and K. A. Zawdie. Ionospheric sluggishness: A characteristic time-lag of the ionospheric response to solar flares. *Journal of Geophysical Research: Space Physics*, n/a(n/a):e2020JA028813. doi: https://doi.org/10.1029/2020JA028813. URL https://agupubs.onlinelibrary.wiley.com/doi/abs/10.1029/2020JA028813. e2020JA028813 2020JA028813.

[27] S. Chakraborty, J. M. Ruohoniemi, J. B. H. Baker, and N. Nishitani. Characterization of Short-Wave Fadeout Seen in Daytime SuperDARN Ground Scatter Observations. *Radio Science*, 53(4):472–484, 2018. doi: https://doi.org/10.1002/2017RS006488. URL https://agupubs.onlinelibrary.wiley.com/doi/abs/10.1002/2017RS006488.

[28] S. Chakraborty, J. B. H. Baker, J. M. Ruohoniemi, B. Kunduri, N. Nishitani, and S. G. Shepherd. A Study of SuperDARN Response to Co-occurring Space Weather Phenomena. *Space Weather*, 17(9):1351–1363, 2019. doi: https://doi.org/10.1029/

2019SW002179. URL https://agupubs.onlinelibrary.wiley.com/doi/abs/10.1029/2019SW002179.

[29] S. Chakraborty, J. M. Ruohoniemi, J. B. H. Baker, R. Fiori, K. Zawdie, S. Bailey, N. Nishitani, and D. Drob. Sluggishness of the ionosphere: Characteristic time-lag in response to solar flares, 2020.

[30] Shibaji Chakraborty. shibaji7/sd_rio_sluggishness: Sluggishness, October 2020. URL http://doi.org/10.5281/zenodo.4085833.

[31] Phillip C. Chamberlin, Thomas N. Woods, and Francis G. Eparvier. Flare Irradiance Spectral Model (FISM): Daily component algorithms and results. *Space Weather*, 5(7), 2007. doi: https://doi.org/10.1029/2007SW000316. URL https://agupubs.onlinelibrary.wiley.com/doi/abs/10.1029/2007SW000316.

[32] Phillip C. Chamberlin, Thomas N. Woods, and Francis G. Eparvier. Flare Irradiance Spectral Model (FISM): Flare component algorithms and results. *Space Weather*, 6(5), 2008. doi: https://doi.org/10.1029/2007SW000372. URL https://agupubs.onlinelibrary.wiley.com/doi/abs/10.1029/2007SW000372.

[33] G. Chisham, M. Lester, S. E. Milan, M. P. Freeman, W. A. Bristow, A. Grocott, K. A. McWilliams, J. M. Ruohoniemi, T. K. Yeoman, P. L. Dyson, R. A. Greenwald, T. Kikuchi, M. Pinnock, J. P. S. Rash, N. Sato, G. J. Sofko, J.-P. Villain, and A. D. M. Walker. A decade of the Super Dual Auroral Radar Network (SuperDARN): scientific achievements, new techniques and future directions. 28(1): 33–109, 2007. ISSN 1573-0956. doi: 10.1007/s10712-007-9017-8. URL https://doi.org/10.1007/s10712-007-9017-8.

[34] Jaroslav Chum, Jann-Yenq Liu, Jan Laštovička, Jiří Fišer, Zbyšek Mošna, Jiří Baše, and Yang-Yi Sun. Ionospheric signatures of the april 25, 2015 nepal earthquake and

the relative role of compression and advection for doppler sounding of infrasound in the ionosphere. *Earth, Planets and Space*, 68(1):24, Feb 2016. ISSN 1880-5981. doi: 10.1186/s40623-016-0401-9. URL https://doi.org/10.1186/s40623-016-0401-9.

[35] Jaroslav Chum, Jaroslav Urbář, Jan Laštovička, Miguel Angel Cabrera, Jann-Yenq Liu, Fernando Alberto Miranda Bonomi, Mariano Fagre, Jiří Fišer, and Zbyšek Mošna. Continuous Doppler sounding of the ionosphere during solar flares. *Earth, Planets and Space*, 70(1):198, Dec 2018. ISSN 1880-5981. doi: 10.1186/s40623-018-0976-4. URL https://doi.org/10.1186/s40623-018-0976-4.

[36] C. J. Coleman. A ray tracing formulation and its application to some problems in over-the-horizon radar. *Radio Science*, 33(4):1187–1197, 1998. doi: https://doi.org/10.1029/98RS01523. URL https://agupubs.onlinelibrary.wiley.com/doi/abs/10.1029/98RS01523.

[37] C.J. Coleman. On the simulation of backscatter ionograms. *Journal of Atmospheric and Solar-Terrestrial Physics*, 59(16):2089 – 2099, 1997. ISSN 1364-6826. doi: https://doi.org/10.1016/S1364-6826(97)00038-2. URL http://www.sciencedirect.com/science/article/pii/S1364682697000382.

[38] J. J. Curto, S. Marsal, E. Blanch, and D. Altadill. Analysis of the Solar Flare Effects of 6 September 2017 in the Ionosphere and in the Earth's Magnetic Field Using Spherical Elementary Current Systems. *Space Weather*, 16(11):1709–1720, 2018. doi: https://doi.org/10.1029/2018SW001927. URL https://agupubs.onlinelibrary.wiley.com/doi/abs/10.1029/2018SW001927.

[39] K Davies. *Ionospheric Radio*. 1990.

[40] J. H. Dellinger. Sudden ionospheric disturbances. *Terrestrial Magnetism and Atmospheric Electricity*, 42(1):49–53, 1937. doi: https://doi.org/10.1029/

TE042i001p00049. URL https://agupubs.onlinelibrary.wiley.com/doi/abs/10.1029/TE042i001p00049.

[41] Howard DeMastus and Marion Wood. Short-wave fadeouts without reported flares. *Journal of Geophysical Research*, 65(2):609–611, 2 1960. ISSN 0148-0227. doi: 10.1029/jz065i002p00609. URL https://agupubs.onlinelibrary.wiley.com/doi/full/10.1029/JZ065i002p00609https://agupubs.onlinelibrary.wiley.com/doi/abs/10.1029/JZ065i002p00609https://agupubs.onlinelibrary.wiley.com/doi/10.1029/JZ065i002p00609.

[42] J. V. Eccles, R. D. Hunsucker, D. Rice, and J. J. Sojka. Space weather effects on midlatitude HF propagation paths: Observations and a data-driven D region model. *Space Weather*, 3(1):n/a–n/a, 1 2005. ISSN 15427390. doi: 10.1029/2004SW000094. URL http://doi.wiley.com/10.1029/2004SW000094.

[43] B. Efron. Second thoughts on the bootstrap. *Statistical Science*, 18(2):135–140, 2003. URL https://doi.org/10.1214/ss/1063994968.

[44] M. A. Ellison. The Hα radiation from solar flares in relation to sudden enhancements of atmospherics on frequencies near 27 Kc/s. *Journal of Atmospheric and Terrestrial Physics*, 4(4-5):226–239, 1953. ISSN 00219169. doi: 10.1016/0021-9169(53)90057-9.

[45] M. A. Ellison. The Solar Flare Radiation Responsible for Sudden Frequency Deviation and Geomagnetic Fluctuation. *Journal of of Geophysical Research*, 101, May 1996.

[46] R A D Fiori and D W Danskin. Examination of the relationship between riometer-derived absorption and the integral proton flux in the context of modeling polar cap absorption. *Space Weather*, 14(11):1032–1052, 11 2016. ISSN 1542-7390. doi: 10.1002/2016SW001461.

[47] R. A. D. Fiori, A. V. Koustov, S. Chakraborty, J. M. Ruohoniemi, D. W. Danskin, D. H. Boteler, and S. G. Shepherd. Examining the Potential of the Super Dual Auroral Radar Network for Monitoring the Space Weather Impact of Solar X-Ray Flares. *Space Weather*, 16(9):1348–1362, 9 2018. ISSN 15427390. doi: 10.1029/2018SW001905. URL http://doi.wiley.com/10.1029/2018SW001905.

[48] V.I. Fomichev, A.A. Kutepov, R.A. Akmaev, and G.M. Shved. Parameterization of the 15 μm CO_2 Band Cooling in the Middle Atmosphere (15-115 km). *Journal of Atmospheric and Terrestrial Physics*, 55(1):7 – 18, 1993. ISSN 0021-9169. doi: https://doi.org/10.1016/0021-9169(93)90149-S. URL http://www.sciencedirect.com/science/article/pii/002191699390149S.

[49] M. Friedrich and K.M. Torkar. Collision frequencies in the high-latitude D-region. *Journal of Atmospheric and Terrestrial Physics*, 45(4):267–271, 4 1983. ISSN 00219169. doi: 10.1016/S0021-9169(83)80048-8. URL https://linkinghub.elsevier.com/retrieve/pii/S0021916983800488.

[50] Nathaniel A Frissell, Joshua S Vega, Evan Markowitz, Andrew J Gerrard, William D Engelke, Philip J Erickson, Ethan S Miller, R Carl Luetzelschwab, and Jacob Bortnik. High-Frequency Communications Response to Solar Activity in September 2017 as Observed by Amateur Radio Networks. *Space Weather*, 17(1):118–132, 2019. doi: 10.1029/2018SW002008. URL https://agupubs.onlinelibrary.wiley.com/doi/abs/10.1029/2018SW002008.

[51] R. R. Garcia, D. R. Marsh, D. E. Kinnison, B. A. Boville, and F. Sassi. Simulation of Secular Trends in the Middle Atmosphere, 1950–2003. *Journal of Geophysical Research: Atmospheres*, 112(D9), 2007. doi: https://doi.org/10.1029/2006JD007485. URL https://agupubs.onlinelibrary.wiley.com/doi/abs/10.1029/2006JD007485.

[52] A. García-Rigo, M. Hernández-Pajares, J.M. Juan, and J. Sanz. Solar flare detection system based on global positioning system data: First results. *Advances in Space Research*, 39(5):889 – 895, 2007. ISSN 0273-1177. doi: https://doi.org/10.1016/j.asr.2006.09.031. URL http://www.sciencedirect.com/science/article/pii/S0273117706006016.

[53] J. A. Gledhill. The effective recombination coefficient of electrons in the ionosphere between 50 and 150 km. *Radio Science*, 21(3):399–408, 1986. doi: https://doi.org/10.1029/RS021i003p00399. URL https://agupubs.onlinelibrary.wiley.com/doi/abs/10.1029/RS021i003p00399.

[54] V. S. Glukhov, V. P. Pasko, and U. S. Inan. Relaxation of transient lower ionospheric disturbances caused by lightning-whistler-induced electron precipitation bursts. *Journal of Geophysical Research*, 97(A11):16971, 11 1992. ISSN 0148-0227. doi: 10.1029/92JA01596. URL http://doi.wiley.com/10.1029/92JA01596.

[55] J. A. Gonzalez-Esparza, M. A. Sergeeva, P. Corona-Romero, J. C. Mejia-Ambriz, L. X. Gonzalez, V. De la Luz, E. Aguilar-Rodriguez, M. Rodriguez, and E. Romero-Hernández. Space weather events, hurricanes, and earthquakes in mexico in september 2017. *Space Weather*, 16(12):2038–2051, 2018. doi: 10.1029/2018SW001995. URL https://agupubs.onlinelibrary.wiley.com/doi/abs/10.1029/2018SW001995.

[56] E. M. Greenberg and J. LaBelle. Measurement and modeling of auroral absorption of hf radio waves using a single receiver. *Radio Science*, 37(2):6–1–6–12, 2002. doi: 10.1029/2000RS002550. URL https://agupubs.onlinelibrary.wiley.com/doi/abs/10.1029/2000RS002550.

[57] R. A. Greenwald, K. B. Baker, R. A. Hutchins, and C. Hanuise. An HF phased-array radar for studying small-scale structure in the high-latitude ionosphere. *Radio Science*,

20(1):63–79, 1985. doi: https://doi.org/10.1029/RS020i001p00063. URL https://agupubs.onlinelibrary.wiley.com/doi/abs/10.1029/RS020i001p00063.

[58] J. B. Gregory and R. E. Newdick. Twenty-seven-day recurrence of solar protons. *Journal of Geophysical Research*, 69(11):2383–2385, 1964. doi: 10.1029/JZ069i011p02383. URL https://agupubs.onlinelibrary.wiley.com/doi/abs/10.1029/JZ069i011p02383.

[59] R. Handzo, J. M. Forbes, and Bodo Reinisch. Ionospheric electron density response to solar flares as viewed by Digisondes. *Space Weather*, 12(4):205–216, 4 2014. ISSN 15427390. doi: 10.1002/2013SW001020. URL http://doi.wiley.com/10.1002/2013SW001020.

[60] Richard Hansen and Josip Kleczek. Coincidence of Sudden Ionospheric Disturbances with the Explosive Phase of Solar Flares. Technical report, 1962.

[61] J. K. Hargreaves and M. J. Birch. On the relations between proton influx and D-region electron densities during the polar-cap absorption event of 28-29 October 2003. *Annales Geophysicae*, 23(10):3267–3276, 11 2005. ISSN 1432-0576. doi: 10.5194/angeo-23-3267-2005. URL http://www.ann-geophys.net/23/3267/2005/.

[62] Jenifer Haselgrove. The Hamiltonian ray path equations. *Journal of Atmospheric and Terrestrial Physics*, 25(7):397 – 399, 1963. ISSN 0021-9169. doi: https://doi.org/10.1016/0021-9169(63)90173-9. URL http://www.sciencedirect.com/science/article/pii/0021916963901739.

[63] Laura A. Hayes, Peter T. Gallagher, Joseph McCauley, Brian R. Dennis, Jack Ireland, and Andrew Inglis. Pulsations in the earth's lower ionosphere synchronized with solar flare emission. *Journal of Geophysical Research: Space Physics*, 122

(10):9841–9847, 2017. doi: https://doi.org/10.1002/2017JA024647. URL https://agupubs.onlinelibrary.wiley.com/doi/abs/10.1002/2017JA024647.

[64] R. A. Heelis, J. K. Lowell, and R. W. Spiro. A model of the High-latitude Ionospheric Convection Pattern. *Journal of Geophysical Research: Space Physics*, 87(A8):6339–6345, 1982. doi: https://doi.org/10.1029/JA087iA08p06339. URL https://agupubs.onlinelibrary.wiley.com/doi/abs/10.1029/JA087iA08p06339.

[65] Erkka Heino, Pekka T. Verronen, Antti Kero, Niilo Kalakoski, and Noora Partamies. Cosmic Noise Absorption During Solar Proton Events in WACCM-D and Riometer Observations. *Journal of Geophysical Research: Space Physics*, 124(2):1361–1376, 2 2019. ISSN 2169-9380. doi: 10.1029/2018JA026192. URL https://onlinelibrary.wiley.com/doi/abs/10.1029/2018JA026192.

[66] B. Honary, J.K. Hargreaves, and S. Browne. An imaging riometer for ionospheric studies. *Electronics & Communication Engineering Journal*, 7(5):209–217, 10 1995. ISSN 0954-0695. doi: 10.1049/ecej:19950505. URL https://digital-library.theiet.org/content/journals/10.1049/ecej_19950505.

[67] Yanshi Huang, Arthur D. Richmond, Yue Deng, Phillip C. Chamberlin, Liying Qian, Stanley C. Solomon, Raymond G. Roble, and Zuo Xiao. Wavelength dependence of solar irradiance enhancement during x-class flares and its influence on the upper atmosphere. *Journal of Atmospheric and Solar-Terrestrial Physics*, 115-116:87 – 94, 2014. ISSN 1364-6826. doi: https://doi.org/10.1016/j.jastp.2013.10.011. URL http://www.sciencedirect.com/science/article/pii/S1364682613002824. Sun-Earth System Exploration: Moderate and Extreme Disturbances.

[68] J D Hunter. Matplotlib: A 2D graphics environment. *Computing In Science & Engi-*

neering, 9(3):90–95, 2007. doi: 10.1109/MCSE.2007.55. URL https://ieeexplore.ieee.org/document/4160265.

[69] James W. Hurrell, M. M. Holland, P. R. Gent, S. Ghan, Jennifer E. Kay, P. J. Kushner, J.-F. Lamarque, W. G. Large, D. Lawrence, K. Lindsay, W. H. Lipscomb, M. C. Long, N. Mahowald, D. R. Marsh, R. B. Neale, P. Rasch, S. Vavrus, M. Vertenstein, D. Bader, W. D. Collins, J. J. Hack, J. Kiehl, and S. Marshall. The Community Earth System Model: A Framework for Collaborative Research. *Bulletin of the American Meteorological Society*, 94(9):1339 – 1360, 01 Sep. 2013. doi: 10.1175/BAMS-D-12-00121.1. URL https://journals.ametsoc.org/view/journals/bams/94/9/bams-d-12-00121.1.xml.

[70] I. T. Jolliffe and D. B. Stephenson. *Forecast Verification: A Practitioner's Guide in Atmospheric Science*. John Wiley & Sons Ltd, Hoboken, 2003.

[71] Y. Kamide and G. Rostoker. What is the physical meaning of the ae index? *Eos, Transactions American Geophysical Union*, 85(19):188–192, 2004. doi: 10.1029/2004EO190010. URL https://agupubs.onlinelibrary.wiley.com/doi/abs/10.1029/2004EO190010.

[72] M. C. Kelley. *The Earth's Ionosphere: Plasma Physics and Electrodynamics*. 2009.

[73] A Kero, C-f Enell, Th Ulich, E Turunen, M T Rietveld, and F H Honary. Statistical signature of active D-region HF heating in IRIS riometer data from 1994-2004. 25: 407–415, 2007. URL www.ann-geophys.net/25/407/2007/.

[74] Ibrahim Khan, M. Indira Devi, T. Arunamani, and D. N. Madhusudhana Rao. A synoptic study of VLF sudden phase anomalies recorded at Visakhapatnam. *Earth, Planets and Space*, 57(11):1073–1081, Nov 2005. ISSN 1880-5981. doi: 10.1186/BF03351886. URL https://doi.org/10.1186/BF03351886.

[75] Takashi Kikuchi, Hidetoshi Sugiuchi, Tsuyoshi Ishimine, Hideo Maeno, and Shigehisa Honma. Solar-Terrestrial Disturbances of June-September 1982, IV. Ionospheric Disturbances, 11. HF Doppler Observations. *Journall of the Radio Research Laboratory*, 33(1):239–255, 1986.

[76] D. E. Kinnison, G. P. Brasseur, S. Walters, R. R. Garcia, D. R. Marsh, F. Sassi, V. L. Harvey, C. E. Randall, L. Emmons, J. F. Lamarque, P. Hess, J. J. Orlando, X. X. Tie, W. Randel, L. L. Pan, A. Gettelman, C. Granier, T. Diehl, U. Niemeier, and A. J. Simmons. Sensitivity of chemical tracers to meteorological parameters in the MOZART-3 chemical transport model. *Journal of Geophysical Research: Atmospheres*, 112(D20), 2007. doi: https://doi.org/10.1029/2006JD007879. URL https://agupubs.onlinelibrary.wiley.com/doi/abs/10.1029/2006JD007879.

[77] D J Knipp, A C Ramsay, E D Beard, A L Boright, W B Cade, I M Hewins, R H McFadden, W F Denig, L M Kilcommons, M A Shea, and D F Smart. The May 1967 great storm and radio disruption event: Extreme space weather and extraordinary responses. *Space Weather*, 14(9):614–633, 9 2016. ISSN 15427390. doi: 10.1002/2016SW001423. URL https://agupubs.onlinelibrary.wiley.com/doi/abs/10.1002/2016SW001423http://doi.wiley.com/10.1002/2016SW001423.

[78] A. Kouznetsov, D. J. Knudsen, E. F. Donovan, and E. Spanswick. Dynamics of the correlation between polar cap radio absorption and solar energetic proton fluxes in the interplanetary medium. *Journal of Geophysical Research: Space Physics*, 119(3):1627–1642, 2013. doi: 10.1002/2013JA019024. URL https://agupubs.onlinelibrary.wiley.com/doi/abs/10.1002/2013JA019024.

[79] L. Křivský. Flare maximum and the "sluggishness" of the ionospheric D-region. *Bulletin of the Astronomical Institutes of Czechoslovakia*, 13:59, January 1962.

[80] Hing-Lan Lam. From Early Exploration to Space Weather Forecasts: Canada's Geomagnetic Odyssey. *Space Weather*, 9(5):n/a–n/a, 5 2011. ISSN 1542-7390. doi: 10.1029/2011sw000664.

[81] Huijun Le, Libo Lui, Han He, and Weixing Wan. Statistical Analysis of Solar EUV and X-Ray Flux Enhancements Induced by Solar Flares and its Implication to Upper Atmosphere. *Journal of Geophysical Research*, 116, 2011. doi: 10.1029/2011JA016704.

[82] Nikolai G. Lehtinen and Umran S. Inan. Possible persistent ionization caused by giant blue jets. *Geophysical Research Letters*, 34(8), 2007. doi: https://doi.org/10.1029/2006GL029051. URL https://agupubs.onlinelibrary.wiley.com/doi/abs/10.1029/2006GL029051.

[83] Edlyn V. Levine, Peter J. Sultan, and Lucien J. Teig. A Parameterized Model of X-Ray Solar Flare Effects on the Lower Ionosphere and HF Propagation. *Radio Science*, 54 (2):168–180, 2 2019. ISSN 0048-6604. doi: 10.1029/2018RS006666. URL https://onlinelibrary.wiley.com/doi/abs/10.1029/2018RS006666.

[84] Nicola Linty, Alex Minetto, Fabio Dovis, and Luca Spogli. Effects of phase scintillation on the gnss positioning error during the september 2017 storm at svalbard. *Space Weather*, 16(9):1317–1329, 2018. doi: 10.1029/2018SW001940. URL https://agupubs.onlinelibrary.wiley.com/doi/abs/10.1029/2018SW001940.

[85] C G Little and H Leinbach. The Riometer-A Device for the Continuous Measurement of Ionospheric Absorption. *Proceedings of the IRE*, 47(2):315–320, 2 1959. ISSN 0096-8390. doi: 10.1109/JRPROC.1959.287299.

[86] H.-L. Liu, B. T. Foster, M. E. Hagan, J. M. McInerney, A. Maute, L. Qian, A. D. Richmond, R. G. Roble, S. C. Solomon, R. R. Garcia, D. Kinnison, D. R. Marsh,

A. K. Smith, J. Richter, F. Sassi, and J. Oberheide. Thermosphere extension of the Whole Atmosphere Community Climate Model. *Journal of Geophysical Research: Space Physics*, 115(A12), 2010. doi: https://doi.org/10.1029/2010JA015586. URL https://agupubs.onlinelibrary.wiley.com/doi/abs/10.1029/2010JA015586.

[87] Han-Li Liu, Charles G. Bardeen, Benjamin T. Foster, Peter Lauritzen, Jing Liu, Gang Lu, Daniel R. Marsh, Astrid Maute, Joseph M. McInerney, Nicholas M. Pedatella, Liying Qian, Arthur D. Richmond, Raymond G. Roble, Stanley C. Solomon, Francis M. Vitt, and Wenbin Wang. Development and Validation of the Whole Atmosphere Community Climate Model With Thermosphere and Ionosphere Extension (WACCM-X 2.0). *Journal of Advances in Modeling Earth Systems*, 10(2):381–402, 2018. doi: https://doi.org/10.1002/2017MS001232. URL https://agupubs.onlinelibrary.wiley.com/doi/abs/10.1002/2017MS001232.

[88] J. Y. Liu, C. S. Chiu, and C. H. Lin. The solar flare radiation responsible for sudden frequency deviation and geomagnetic fluctuation. *Journal of Geophysical Research: Space Physics*, 101(A5):10855–10862, 1996. doi: https://doi.org/10.1029/95JA03676. URL https://agupubs.onlinelibrary.wiley.com/doi/abs/10.1029/95JA03676.

[89] J. Y. Liu, C. H. Lin, Y. I. Chen, Y. C. Lin, T. W. Fang, C. H. Chen, Y. C. Chen, and J. J. Hwang. Solar flare signatures of the ionospheric GPS total electron content. *Journal of Geophysical Research*, 111(A5):A05308, 5 2006. ISSN 0148-0227. doi: 10.1029/2005JA011306. URL http://doi.wiley.com/10.1029/2005JA011306.

[90] Jing Liu, Hanli Liu, Wenbin Wang, Alan G. Burns, Qian Wu, Quan Gan, Stanley C. Solomon, Daniel R. Marsh, Liying Qian, Gang Lu, Nicholas M. Pedatella, Joe M. McInerney, James M. Russell III, and William S. Schreiner. First Results From the Ionospheric Extension of WACCM-X During the Deep Solar Mini-

mum Year of 2008. *Journal of Geophysical Research: Space Physics*, 123(2):1534–1553, 2018. doi: https://doi.org/10.1002/2017JA025010. URL https://agupubs.onlinelibrary.wiley.com/doi/abs/10.1002/2017JA025010.

[91] Jing Liu, Liying Qian, Astrid Maute, Wenbin Wang, Arthur D. Richmond, Junjie Chen, Jiuhou Lei, Qinghe Zhang, and Zanyang Xing. Electrodynamical coupling of the geospace system during solar flares. *Journal of Geophysical Research: Space Physics*, 2020. doi: https://doi.org/10.1029/2020JA028569. URL https://agupubs.onlinelibrary.wiley.com/doi/abs/10.1029/2020JA028569. e2020JA028569 2020JA028569.

[92] G. Lu and A. D. Richmond. Specification and Forecast of Ionospheric Conditions with AMIE. In *The Evaluation of Space Weather Forecasts*, pages 35–38, 1996.

[93] Janet Machol. GOES X-ray Sensor (XRS) Measurements Important notes for users. Technical report, 2016.

[94] B. Maehlum and B. J. O'brien. Study of energetic electrons and their relationship to auroral absorption of radio waves. *Journal of Geophysical Research*, 68(4):997–1010, 1963. doi: 10.1029/JZ068i004p00997. URL https://agupubs.onlinelibrary.wiley.com/doi/abs/10.1029/JZ068i004p00997.

[95] R. C. Majumdar. Generalization of Appleton-Hartree Equation of Theories of Collision Frequency. 1:31–37, 1971. URL http://nopr.niscair.res.in/bitstream/123456789/38050/1/IJRSP1%281%2931-37.pdf.

[96] Daniel R. Marsh, Michael J. Mills, Douglas E. Kinnison, Jean-Francois Lamarque, Natalia Calvo, and Lorenzo M. Polvani. Climate Change from 1850 to 2005 Simulated in CESM1(WACCM). *Journal of Climate*, 26(19):7372 – 7391, 01 Oct.

2013. doi: 10.1175/JCLI-D-12-00558.1. URL https://journals.ametsoc.org/view/journals/clim/26/19/jcli-d-12-00558.1.xml.

[97] Wes McKinney. Data Structures for Statistical Computing in Python. In Stéfan van der Walt and Jarrod Millman, editors, *Proceedings of the 9th Python in Science Conference*, pages 56–61, 2010. doi: 10.25080/Majora-92bf1922-012. URL https://conference.scipy.org/proceedings/scipy2010/mckinney.html.

[98] L. F. McNamara. Statistical Model of D Region. *Radio Science*, 14(6):1165–1173, 1978.

[99] Wayne M. McRae and Neil R. Thomson. Solar flare induced ionospheric d-region enhancements from vlf phase and amplitude observations. *Journal of Atmospheric and Solar-Terrestrial Physics*, 66(1):77 – 87, 2004. ISSN 1364-6826. doi: https://doi.org/10.1016/j.jastp.2003.09.009. URL http://www.sciencedirect.com/science/article/pii/S1364682603002207.

[100] Michael Mendillo and John V. Evans. Incoherent scatter observations of the ionospheric response to a large solar flare. *Radio Science*, 9(2):197–203, 2 1974. ISSN 00486604. doi: 10.1029/RS009i002p00197. URL http://doi.wiley.com/10.1029/RS009i002p00197.

[101] R. T. Merrill, M. W. McElhinny, and P. L. McFadden. *The Magnetic Field of the Earth: Paleomagnetism, the Core, and the Deep Mantle*. 1998. URL https://books.google.com/books?id=96APl4nK9lIC.

[102] K Jarrod Millman and Michael Aivazis. Python for Scientists and Engineers. *Computing in Science & Engineering*, 13(2):9–12, 2011. doi: 10.1109/MCSE.2011.36. URL https://ieeexplore.ieee.org/document/5725235.

[103] A. P. Mitra. *Ionospheric effects of solar flares*, volume 46. 1974. doi: 10.1007/978-94-010-2231-6.

[104] A. P. Mitra and V. C. Jain. Interpretation of the observed zenith-angle dependence of ionospheric absorption. *Journal of Geophysical Research (1896-1977)*, 68(9):2367–2373, 1963. doi: https://doi.org/10.1029/JZ068i009p02367. URL https://agupubs.onlinelibrary.wiley.com/doi/abs/10.1029/JZ068i009p02367.

[105] A. P. Mitra and C. A. Shain. The Measurement of Ionospheric Absorption using Observations of 18.3 Ms/s Cosmic Radio Noise. *Jurnal of Atmospheric and Terrestrial Physics*, 4, 1953. Pergamon Press Ltd., London.

[106] S. K. Mitra. *Upper Atmosphere*. Asiatic Society, 1992.

[107] S. K. Morley, J. Koller, D. T. Welling, B. A. Larsen, M. G. Henderson, and J. T. Niehof. Spacepy - A Python-based library of tools for the space sciences. In *Proceedings of the 9th Python in science conference (SciPy 2010)*, Austin, TX, 2011.

[108] Steven Morley. drsteve/PyForecastTools: PyForecastTools, June 2018. URL https://doi.org/10.5281/zenodo.1256921.

[109] Richard B. Neale, Jadwiga Richter, Sungsu Park, Peter H. Lauritzen, Stephen J. Vavrus, Philip J. Rasch, and Minghua Zhang. The Mean Climate of the Community Atmosphere Model (CAM4) in Forced SST and Fully Coupled Experiments. *Journal of Climate*, 26(14):5150 – 5168, 15 Jul. 2013. doi: 10.1175/JCLI-D-12-00236.1. URL https://journals.ametsoc.org/view/journals/clim/26/14/jcli-d-12-00236.1.xml.

[110] H. W. Newton and H. J. Barton. Bright Solar Eruptions and Radio Fadings during the

Years 1935-36. *Royal Astronomical Society*, 1937. Provided by the NASA Astrophysics Data System.

[111] A. Nina, V. Čadež, D. Šulić, V. Srećković, and V. Žigman. Effective electron recombination coefficient in ionospheric d-region during the relaxation regime after solar flare from february 18, 2011. *Nuclear Instruments and Methods in Physics Research Section B: Beam Interactions with Materials and Atoms*, 279:106 – 109, 2012. ISSN 0168-583X. doi: https://doi.org/10.1016/j.nimb.2011.10.026. URL http://www.sciencedirect.com/science/article/pii/S0168583X11009657. Proceedings of the Fifth International Conference on Elementary Processes in Atomic Systems Belgrade, Serbia, 21-25 June 2011.

[112] Nozomu Nishitani, John Michael Ruohoniemi, Mark Lester, Joseph Benjamin Harold Baker, Alexandre Vasilyevich Koustov, Simon G. Shepherd, Gareth Chisham, Tomoaki Hori, Evan G. Thomas, Roman A. Makarevich, Aurélie Marchaudon, Pavlo Ponomarenko, James A. Wild, Stephen E. Milan, William A. Bristow, John Devlin, Ethan Miller, Raymond A. Greenwald, Tadahiko Ogawa, and Takashi Kikuchi. Review of the accomplishments of mid-latitude Super Dual Auroral Radar Network (SuperDARN) HF radars. 6(1):27, 2019. ISSN 2197-4284. doi: 10.1186/s40645-019-0270-5. URL https://doi.org/10.1186/s40645-019-0270-5.

[113] Sourav Palit, Tamal Basak, Sujay Pal, and Sandip K. Chakrabarti. Theoretical study of lower ionospheric response to solar flares: sluggishness of d-region and peak time delay. 356(1):19–28, 2015. ISSN 1572-946X. doi: 10.1007/s10509-014-2190-6. URL https://doi.org/10.1007/s10509-014-2190-6.

[114] N. M. Pedatella, H.-L. Liu, D. R. Marsh, K. Raeder, J. L. Anderson, J. L. Chau, L. P. Goncharenko, and T. A. Siddiqui. Analysis and Hindcast Experiments of

the 2009 Sudden Stratospheric Warming in WACCMX+DART. *Journal of Geophysical Research: Space Physics*, 123(4):3131–3153, 2018. doi: https://doi.org/10.1002/2017JA025107. URL https://agupubs.onlinelibrary.wiley.com/doi/abs/10.1002/2017JA025107.

[115] N. M. Pedatella, J. L. Chau, J. Vierinen, L. Qian, P. Reyes, E. Kudeki, G. Lehmacher, and M. Oppenheim. Solar Flare Effects on 150-km Echoes Observed Over Jicamarca: WACCM-X Simulations. *Geophysical Research Letters*, 46(20):10951–10958, 10 2019. ISSN 0094-8276. doi: 10.1029/2019GL084790. URL https://onlinelibrary.wiley.com/doi/abs/10.1029/2019GL084790.

[116] L. H. Pederick and M. A. Cervera. Semiempirical Model for Ionospheric Absorption based on the NRLMSISE-00 atmospheric model. *Radio Science*, 49(2):81–93, 2 2014. ISSN 00486604. doi: 10.1002/2013RS005274. URL http://doi.wiley.com/10.1002/2013RS005274.

[117] D. Pequignot, P. Petitjean, and C. Boisson. Total and effective radiative recombination coefficients. *AAP*, 251:680–688, November 1991.

[118] F. Perez and B. E. Granger. Ipython: A system for interactive scientific computing. *Computing in Science Engineering*, 9(3):21–29, May 2007. ISSN 1521-9615. doi: 10.1109/MCSE.2007.53. URL https://ieeexplore.ieee.org/document/4160251.

[119] J. M. Picone, A. E. Hedin, D. P. Drob, and A. C. Aikin. Nrlmsise-00 empirical model of the atmosphere: Statistical comparisons and scientific issues. *Journal of Geophysical Research: Space Physics*, 107(A12):SIA 15–1–SIA 15–16, 2002. doi: https://doi.org/10.1029/2002JA009430. URL https://agupubs.onlinelibrary.wiley.com/doi/abs/10.1029/2002JA009430.

[120] Liying Qian, Alan G. Burns, Stanley C. Solomon, and Phillip C. Chamberlin. Solar flare impacts on ionospheric electrodyamics. *Geophysical Research Letters*, 39 (6), 2012. doi: https://doi.org/10.1029/2012GL051102. URL https://agupubs.onlinelibrary.wiley.com/doi/abs/10.1029/2012GL051102.

[121] Liying Qian, Alan G. Burns, Stan S. Solomon, Anne K. Smith, Joseph M. McInerney, Linda A. Hunt, Daniel R. Marsh, Hanli Liu, Martin G. Mlynczak, and Francis M. Vitt. Temporal Variability of Atomic Hydrogen From the Mesopause to the Upper Thermosphere. *Journal of Geophysical Research: Space Physics*, 123 (1):1006–1017, 2018. doi: https://doi.org/10.1002/2017JA024998. URL https://agupubs.onlinelibrary.wiley.com/doi/abs/10.1002/2017JA024998.

[122] R. G. Rastogi, B. M. Pathan, D. R. K. Rao, T. S. Sastry, and J. H. Sastri. Solar Flare Effects on the Geomagnetic Elements during Normal and Counter Electrojet Periods. *Earth, Planets and Space*, 51(9):947–957, 9 1999. ISSN 1880-5981. doi: 10.1186/BF03351565. URL http://earth-planets-space.springeropen.com/articles/10.1186/BF03351565.

[123] R. J. Redmon, D. B. Seaton, R. Steenburgh, J. He, and J. V. Rodriguez. September 2017's Geoeffective Space Weather and Impacts to Caribbean Radio Communications During Hurricane Response. *Space Weather*, 16(9):1190–1201, 9 2018. ISSN 15427390. doi: 10.1029/2018SW001897. URL http://doi.wiley.com/10.1029/2018SW001897.

[124] George C. Reid. Production and loss of electrons in the quiet daytime d region of the ionosphere. *Journal of Geophysical Research (1896-1977)*, 75(13):2551–2562, 1970. doi: https://doi.org/10.1029/JA075i013p02551. URL https://agupubs.onlinelibrary.wiley.com/doi/abs/10.1029/JA075i013p02551.

[125] P. G. Richards and David Voglozin. Reexamination of ionospheric photochemistry.

Journal of Geophysical Research: Space Physics, 116(A8):n/a–n/a, 8 2011. ISSN 01480227. doi: 10.1029/2011JA016613. URL http://doi.wiley.com/10.1029/2011JA016613.

[126] Philip G. Richards, Thomas N. Woods, and William K. Peterson. HEUVAC: A new high resolution solar EUV proxy model. *Advances in Space Research*, 37(2): 315–322, 1 2006. ISSN 0273-1177. doi: 10.1016/J.ASR.2005.06.031. URL https://www.sciencedirect.com/science/article/pii/S0273117705008288.

[127] A. D. Richmond, M. Blanc, B. A. Emery, R. H. Wand, B. G. Fejer, R. F. Woodman, S. Ganguly, P. Amayenc, R. A. Behnke, C. Calderon, and J. V. Evans. An empirical model of quiet-day ionospheric electric fields at middle and low latitudes. *Journal of Geophysical Research: Space Physics*, 85(A9):4658–4664, 1980. doi: https://doi.org/10.1029/JA085iA09p04658. URL https://agupubs.onlinelibrary.wiley.com/doi/abs/10.1029/JA085iA09p04658.

[128] A.D. Richmond. Assimilative mapping of ionospheric electrodynamics. *Advances in Space Research*, 12(6):59 – 68, 1992. ISSN 0273-1177. doi: https://doi.org/10.1016/0273-1177(92)90040-5. URL http://www.sciencedirect.com/science/article/pii/0273117792900405.

[129] Craig J. Rodger, Oleg A. Molchanov, and Neil R. Thomson. Relaxation of transient ionization in the lower ionosphere. *Journal of Geophysical Research: Space Physics*, 103(A4):6969–6975, 1998. doi: 10.1029/98JA00016. URL https://agupubs.onlinelibrary.wiley.com/doi/abs/10.1029/98JA00016.

[130] N. C. Rogers, A. Kero, F. Honary, P. T. Verronen, E. M. Warrington, and D. W. Danskin. Improving the twilight model for polar cap absorption nowcasts. *Space*

Weather, 14(11):950–972, 2016. doi: 10.1002/2016SW001527. URL https://agupubs.onlinelibrary.wiley.com/doi/abs/10.1002/2016SW001527.

[131] Neil Rogers and Farideh Honary. D-region HF absorption models incorporating real-time riometer measurements. pages 1–2. Institute of Electrical and Electronics Engineers (IEEE), 10 2014. doi: 10.1109/ursigass.2014.6929716.

[132] T. J. Rosenberg, D. L. Detrick, D. Venkatesan, and G. van Bavel. A comparative study of imaging and broad-beam riometer measurements: The effect of spatial structure on the frequency dependence of auroral absorption. *Journal of Geophysical Research: Space Physics*, 96(A10):17793–17803, 1991. doi: 10.1029/91JA01827. URL https://agupubs.onlinelibrary.wiley.com/doi/abs/10.1029/91JA01827.

[133] G. Rostoker, J. C. Samson, F. Creutzberg, T. J. Hughes, D. R. McDiarmid, A. G. McNamara, A. Vallance Jones, D. D. Wallis, and L. L. Cogger. Canopus - A ground-based instrument array for remote sensing the high latitude ionosphere during the ISTP/GGS program. *Space Science Reviews*, 71(1-4):743–760, 2 1995. ISSN 00386308. doi: 10.1007/BF00751349.

[134] Teruo Sato. Sudden fmin enhancements and sudden cosmic noise absorptions associated with solar X-ray flares. *Journal of geomagnetism and geoelectricity*, 27(2):95–112, 1975. ISSN 0022-1392. doi: 10.5636/jgg.27.95. URL http://joi.jlc.jst.go.jp/JST.Journalarchive/jgg1949/27.95?from=CrossRef.

[135] Herbert H. Sauer and Daniel C. Wilkinson. Global mapping of ionospheric HF/VHF radio wave absorption due to solar energetic protons. *Space Weather*, 6(12):n/a–n/a, 12 2008. ISSN 15427390. doi: 10.1029/2008SW000399. URL http://doi.wiley.com/10.1029/2008SW000399.

[136] E. D. Schmitter. Remote sensing planetary waves in the midlatitude mesosphere using low frequency transmitter signals. *Annales Geophysicae*, 29(7):1287–1293, 2011. doi: 10.5194/angeo-29-1287-2011. URL https://angeo.copernicus.org/articles/29/1287/2011/.

[137] Evelyn A. Schumer. *IMPROVED MODELING OF MIDLATITUDE D-REGION IONOSPHERIC ABSORPTION OF HIGH FREQUENCY RADIO SIGNALS DURING SOLAR X-RAY FLARES*. PhD thesis, 2009.

[138] R. W. Schunk and Andrew F. Nagy. Electron temperatures in the F region of the ionosphere: Theory and observations, 8 1978. ISSN 19449208. URL http://doi.wiley.com/10.1029/RG016i003p00355.

[139] Robert Schunk and Andrew Nagy. *Ionospheres*. Cambridge University Press, 2009. doi: 10.1017/cbo9780511635342. URL /core/books/ionospheres/0C725C779F49AE7DF0C45BF5A350A003.

[140] H K Sen and A A Wyller. GENERALIZATION OF THE APPLETON-HARTREE MAGNETO-IONIC FORMULA. 4(7), 1960. URL https://journals.aps.org/prl/pdf/10.1103/PhysRevLett.4.355.

[141] D. K. Sharma, J. Rai, M. Israil, P. Subrahmanyam, P. Chopra, and S. C. Garg. Enhancement in electron and ion temperatures due to solar flares as measured by sross-c2 satellite. *Annales Geophysicae*, 22(6):2047–2052, 2004. doi: 10.5194/angeo-22-2047-2004. URL https://angeo.copernicus.org/articles/22/2047/2004/.

[142] David E. Siskind, K. A. Zawdie, F. Sassi, D. Drob, and M. Friedrich. Global Modeling of the low- and middle-latitude Ionospheric D and lower E Regions and Implications for

HF Radio Wave Absorption. *Space Weather*, 15(1):115–130, 1 2017. ISSN 15427390. doi: 10.1002/2016SW001546. URL http://doi.wiley.com/10.1002/2016SW001546.

[143] Stanley C. Solomon and Liying Qian. Solar extreme-ultraviolet irradiance for general circulation models. *Journal of Geophysical Research: Space Physics*, 110 (A10), 2005. doi: https://doi.org/10.1029/2005JA011160. URL https://agupubs.onlinelibrary.wiley.com/doi/abs/10.1029/2005JA011160.

[144] Stanley C. Solomon, Han-Li Liu, Daniel R. Marsh, Joseph M. McInerney, Liying Qian, and Francis M. Vitt. Whole Atmosphere Simulation of Anthropogenic Climate Change. *Geophysical Research Letters*, 45(3):1567–1576, 2018. doi: https://doi.org/10.1002/2017GL076950. URL https://agupubs.onlinelibrary.wiley.com/doi/abs/10.1002/2017GL076950.

[145] Stanley C. Solomon, Han-Li Liu, Daniel R. Marsh, Joseph M. McInerney, Liying Qian, and Francis M. Vitt. Whole Atmosphere Climate Change: Dependence on Solar Activity. *Journal of Geophysical Research: Space Physics*, 124(5):3799–3809, 2019. doi: https://doi.org/10.1029/2019JA026678. URL https://agupubs.onlinelibrary.wiley.com/doi/abs/10.1029/2019JA026678.

[146] M. A. Stephens. Edf statistics for goodness of fit and some comparisons. *Journal of the American Statistical Association*, 69(347):730–737, 1974. ISSN 01621459. URL http://www.jstor.org/stable/2286009.

[147] G. H. Stonehocker. Advanced telecommunication forecasting technique in AGY. pages 27–31. 5th. Ionospheric forecasting, AGARD, 1970.

[148] S. G. Sumod and Tarun Kumar Pant. An investigation of solar flare effects on equatorial ionosphere and thermosphere using co-ordinated measurements. *Earth, Planets*

and Space, 71(1):125, Nov 2019. ISSN 1880-5981. doi: 10.1186/s40623-019-1105-8. URL https://doi.org/10.1186/s40623-019-1105-8.

[149] P. R. Sutcliffe and A. W. V. Poole. Ionospheric doppler and electron velocities in the presence of ulf waves. *Journal of Geophysical Research: Space Physics*, 94(A10): 13505–13514, 1989. doi: https://doi.org/10.1029/JA094iA10p13505. URL https://agupubs.onlinelibrary.wiley.com/doi/abs/10.1029/JA094iA10p13505.

[150] Chihiro Tao, Michi Nishioka, Susumu Saito, Daikou Shiota, Kyoko Watanabe, Naoto Nishizuka, Takuya Tsugawa, and Mamoru Ishii. Statistical analysis of short-wave fadeout for extreme space weather event estimation. *Earth, Planets and Space*, 72 (1):173, Nov 2020. ISSN 1880-5981. doi: 10.1186/s40623-020-01278-z. URL https://doi.org/10.1186/s40623-020-01278-z.

[151] Erwan Thébault, Christopher C. Finlay, Ciarán D. Beggan, Patrick Alken, Julien Aubert, Olivier Barrois, Francois Bertrand, Tatiana Bondar, Axel Boness, Laura Brocco, Elisabeth Canet, Aude Chambodut, Arnaud Chulliat, Pierdavide Coïsson, François Civet, Aimin Du, Alexandre Fournier, Isabelle Fratter, Nicolas Gillet, Brian Hamilton, Mohamed Hamoudi, Gauthier Hulot, Thomas Jager, Monika Korte, Weijia Kuang, Xavier Lalanne, Benoit Langlais, Jean-Michel Léger, Vincent Lesur, Frank J. Lowes, Susan Macmillan, Mioara Mandea, Chandrasekharan Manoj, Stefan Maus, Nils Olsen, Valeriy Petrov, Victoria Ridley, Martin Rother, Terence J. Sabaka, Diana Saturnino, Reyko Schachtschneider, Olivier Sirol, Andrew Tangborn, Alan Thomson, Lars Tøffner-Clausen, Pierre Vigneron, Ingo Wardinski, and Tatiana Zvereva. International geomagnetic reference field: the 12th generation. *Earth, Planets and Space*, 67(1):79, May 2015. ISSN 1880-5981. doi: 10.1186/s40623-015-0228-9. URL https://doi.org/10.1186/s40623-015-0228-9.

[152] B. T. Tsurutani, D. L. Judge, F. L. Guarnieri, P. Gangopadhyay, A. R. Jones, J. Nuttall, G. A. Zambon, L. Didkovsky, A. J. Mannucci, B. Iijima, R. R. Meier, T. J. Immel, T. N. Woods, S. Prasad, L. Floyd, J. Huba, S. C. Solomon, P. Straus, and R. Viereck. The october 28, 2003 extreme euv solar flare and resultant extreme ionospheric effects: Comparison to other halloween events and the bastille day event. *Geophysical Research Letters*, 32(3), 2005. doi: 10.1029/2004GL021475. URL https://agupubs.onlinelibrary.wiley.com/doi/abs/10.1029/2004GL021475.

[153] B. T. Tsurutani, F. L. Guarnieri, T. Fuller-Rowell, A. J. Mannucci, B. Iijima, W. D. Gonzalez, D. L. Judge, P. Gangopadhyay, A. Saito, T. Tsuda, O. P. Verkhoglyadova, and G. A. Zambon. Extreme Solar EUV Flares and ICMEs and Resultant Extreme Ionospheric Effects: Comparison of the Halloween 2003 and the Bastille day events. *Radio Science*, 41, 2006. doi: 10.1029/2005RS003331.

[154] B. T. Tsurutani, O. P. Verkhoglyadova, A. J. Mannucci, G. S. Lakhina, G. Li, and G. P. Zank. A brief review of "solar flare effects" on the ionosphere. *Radio Science*, 44(1), 2009. doi: 10.1029/2008RS004029. URL https://agupubs.onlinelibrary.wiley.com/doi/abs/10.1029/2008RS004029.

[155] P. T. Verronen, Th. Ulich, E. Turunen, and C. J. Rodger. Sunset transition of negative charge in the d-region ionosphere during high-ionization conditions. *Annales Geophysicae*, 24(1):187–202, 2006. doi: 10.5194/angeo-24-187-2006. URL https://angeo.copernicus.org/articles/24/187/2006/.

[156] Daiki Watanabe and Nozomu Nishitani. Study of Ionospheric Disturbances During Solar Flare Events Using the SuperDARN Hokkaido Radar. *Advances in Polar Science*, 24(1):12–18, 2013. doi: 10.3724/SP.J.1085.2013.00012.

[157] D. R. Weimer. Improved Ionospheric Electrodynamic Models and Application to Cal-

culating Joule Heating Rates. *Journal of Geophysical Research: Space Physics*, 110 (A5), 2005. doi: https://doi.org/10.1029/2004JA010884. URL https://agupubs.onlinelibrary.wiley.com/doi/abs/10.1029/2004JA010884.

[158] R. C. Whitten, I. G. Poppoff, R. S. Edmonds, and W. W. Berning. Effective recombination coefficients in the lower ionosphere. *Journal of Geophysical Research (1896-1977)*, 70(7):1737–1742, 1965. doi: https://doi.org/10.1029/JZ070i007p01737. URL https://agupubs.onlinelibrary.wiley.com/doi/abs/10.1029/JZ070i007p01737.

[159] Bo Xiong, Weixing Wan, Baiqi Ning, Feng Ding, Lianhuan Hu, and You Yu. A Statistic Study of Ionospheric Solar Flare Indicator. *Space Weather*, 12:29–40, 2013. doi: 10.1002/2013SW001000.

[160] Y. Yasyukevich, E. Astafyeva, A. Padokhin, V. Ivanova, S. Syrovatskii, and A. Podlesnyi. The 6 September 2017 X-Class Solar Flares and Their Impacts on the Ionosphere, GNSS, and HF Radio Wave Propagation. *Space Weather*, 16(8): 1013–1027, 8 2018. ISSN 15427390. doi: 10.1029/2018SW001932. URL http://doi.wiley.com/10.1029/2018SW001932.

[161] N. Y. Zaalov, E. V. Moskaleva, and F. V. Shekhovtsov. Method of the HF wave absorption evaluation based on GIRO network data. *Advances in Space Research*, 63 (7):2075–2087, 4 2019. ISSN 18791948. doi: 10.1016/j.asr.2018.12.024.

[162] K. A. Zawdie, D. P. Drob, D. E. Siskind, and C. Coker. Calculating the absorption of HF radio waves in the ionosphere. *Radio Science*, 52(6):767–783, 6 2017. ISSN 00486604. doi: 10.1002/2017RS006256. URL http://doi.wiley.com/10.1002/2017RS006256.

[163] V. Žigman, D. Grubor, and D. Šulić. D-region electron density evaluated from vlf amplitude time delay during x-ray solar flares. *Journal of Atmospheric and Solar-*

Terrestrial Physics, 69(7):775 – 792, 2007. ISSN 1364-6826. doi: https://doi.org/10.1016/j.jastp.2007.01.012. URL http://www.sciencedirect.com/science/article/pii/S1364682607000259.